A dissertation for Doctor of Philosophy in Physics

Azimuthal Anisotropy of K^0_S and $\Lambda + \bar{\Lambda}$ Production at mid-Rapidity from Au+Au Collisions at $\sqrt{s_{NN}} = 130$ GeV and Erraticity Behaviour of Event Factorial Moments in Hadron-Hadron Collisions

by

Fu Jinghua

Co-supervisor: Wu Yuanfang, Xu Nu, Liu Lianshou

Thesis defended on August 26, 2002

PhD degree awarded on January 17, 2003

Central China Normal University

July 2002

Azimuthal Anisotropy of K^0_S and $\Lambda + \bar{\Lambda}$ Production at mid-Rapidity from Au+Au Collisions at $\sqrt{s_{NN}} = 130$ GeV and Erraticity Behaviour of Event Factorial Moments in Hadron-Hadron Collisions

Abstract

The operation and first collisions of Au nuclei in the Relativistic Heavy Ion Collider (RHIC) at Brookhaven National Laboratory (BNL) during year 2000 began a new era in the study of nuclear matter at high energy density and the search of Quark-Gluon Plasma (QGP). The properties of the QGP and the transition to it have to be identified from the final state which is of a hadronic nature. Measurements of azimuthal anisotropies in the transverse momentum distribution of particles can probe the very early stages of ultra-relativistic heavy-ion collisions. This dissertation presents the STAR results on the azimuthal anisotropy parameter v_2 for strange particles K^0_S, Λ and $\bar{\Lambda}$ at mid-rapidity in Au+Au collisions at $\sqrt{s_{NN}} = 130$ GeV at RHIC. The value of v_2 as a function of transverse momentum p_t and collision centrality is presented for both particles up to ~ 3.0 GeV/c. A strong p_t dependence in v_2 is observed up to 2.0 GeV/c. The v_2 measurement is compared with hydrodynamic model calculations. The physics implication of the p_t integrated v_2 magnitude as a function of particle mass is also discussed.

Erraticity analysis provide new opportunity in measuring event by event fluctuations in high energy nuclear collisions. In the second part of this dissertation (chapter 6 and chapter 7), it is demonstrated that in low multiplicity sample, the increase of the fluctuation of event factorial moments with the diminishing of phase space scale, "erraticity", are dominated by the statistical fluctuations. Applying erraticity analysis to high multiplicity sample at RHIC and LHC energy is recommended.

Contents

List of Tables

List of Figures

Chapter 1

Introduction

What is the ultimate building blocks of matter has puzzling us for thousands of years. Over the past hundred years our knowledge on this fundamental question have gone through a considerable evolution. Atoms were found to be divisible into electrons and nuclei. Nuclei in turn consist of nucleons, bound together by strong short-range forces. The basic theory of strong interaction, quantum chromodynamics (QCD), predicts all strongly interacting elementary particles (hadrons) are bound states of quarks (q) or their anti-particles ($\bar{q}$)[49]. Quarks themselves are never seen in isolation, but strongly interact and form particles (hadrons), which are either baryons (qqq) or mesons ($q\bar{q}$). QCD predicts that at high energy density, hadronic matter will turn into a plasma of deconfined quarks and gluons (QGP), which probably exist in the early universe or the core of neutron stars. In 1986/1987, experimental studies of high energy nuclear collisions began from fixed-target machines at the BNL (Brookhaven National Laboratory)-AGS (Alternating Gradient Synchrotron) and the CERN (European Centre for Nuclear Research)-SPS (Super Proton Synchrotron). At BNL, the Relativistic Heavy Ion Collider (RHIC) started operating in 2000. In its first run, RHIC collided Au ions at a center of mass energy of 130 GeV per nucleon pair, about 7.5 times higher than that previously possible in fixed target experiments at CERN. The main features of the three accelerators are listed in Table1.1. At CERN, the Large Hadron Collider (LHC) is under construction and planned for five years later at even higher collision energy.

Accelerator	System	Beam Energy	COM Energy	Beam Rapidity
AGS	Au+Au	4	3.08	2.16
AGS	Au+Au	6	3.63	2.55
AGS	Au+Au	8	4.10	2.84
AGS	Au+Au	10	4.54	3.06
AGS	Au+Au	10.8	4.70	3.14
AGS	Au+Au	11.6	4.86	3.21
SPS	S+S	200	19.41	6.06
SPS	Pb+Pb	40	8.76	4.45
SPS	Pb+Pb	80	12.32	5.14
SPS	Pb+Pb	158	17.27	5.82
RHIC	Au+Au	65	130	$\pm$4.93
RHIC	Au+Au	100	200	$\pm$5.36

Table 1.1: The main features of the different accelerators used in relativistic heavy ion physics, the unit for beam energy and COM energy is GeV/A.

The goal of the ultra-relativistic nuclear collision program is the creation of a system of deconfined quarks and gluons, an entirely new phase of nuclear matter. The properties of the QGP and the transition to it have to be identified from the final state which is of a hadronic nature. If this system is created, its evolution should be governed by the physics of deconfined matter. There is still no reliable signatures for the QGP state and the transition. Measurements of azimuthal anisotropies in the transverse momentum distribution of particles can probe early stages of ultra-relativistic heavy-ion collisions[96, 97, 81]. Up to now most of the anisotropic flow parameters measured are for non-strange particles[23, 41, 89, 80, 28, 32, 39] and only a handful of studies for identified strange particles have been reported[41, 33, 34, 31, 30, 29, 42], all at much lower collision energies. Moreover, previous measurements of strange particle flow correspond to directed flow. We make the first measurement of the azimuthal anisotropy parameter for the strange particles K^0_S, Λ and $\bar{\Lambda}$ from Au+Au collisions at $\sqrt{s_{NN}}$=130 GeV.

This thesis starts with general aspects of heavy ion collisions (chapter 2), followed by a description of the RHIC experiment and STAR detector (chapter 3). The method to reconstruct neutral strange particle in STAR and reconstruct flow signal

experimentally are presented in chapter 4. The result of K^0_S and $\Lambda + \bar{\Lambda}$ anisotropy analysis from first year STAR data are presented in chapter 5.

Central ultra-relativistic nuclear collisions at RHIC produce about $\sim 10^3$ particles and thus present remarkable opportunity to analyze, on an event-by-event basis, fluctuations in physical observables. The capability of measuring several different observables event-by-event is also unique to STAR experiment. Analysis of single events with large statistics can reveal very different physics than studying averages over a large statistical sample of events. Erraticity method was recently proposed[11] for event by event analysis by studying event (phase) space patterns with event-factorial-moments. The influence of statistical fluctuations on this method was studied with Monte Carlo simulation and CERN NA22 π^+p and K^+p experiment data in chapter6 and chapter7.

Chapter 2

Relativistic Heavy Ion Collisions

2.1 States of Strongly Interacting Matter

Ultra-relativistic heavy-ion collisions will produce strongly interacting matter with energy density much higher than normal nuclear matter. It provides a way to investigate the behavior of matter under extreme conditions of temperature, pressure and energy density.

2.1.1 From Hadronic Matter to Quark-Gluon Plasma

Quarks are point-like and confined to "their" hadron by a binding potential

$$V_0(r) \sim \sigma r, \tag{2.1}$$

where the string tension σ measures the energy per unit separation distance. $V_0(r)$ increases linearly with quark separation, which makes quark cannot exist by itself. Similar to Debye screening in QED[76], at sufficiently high density we expect colour screening to set in and the potential(2.1) becomes [19]

$$V(r) \simeq \sigma r \left[\frac{1-\exp(-\mu r)}{\mu r}\right], \tag{2.2}$$

where, μ is the color screening mass, which is also the inverse of the screening radius for colour charges. As shown in Fig.2.1, when $\mu \neq 0$ potential $V(r)$ does not go

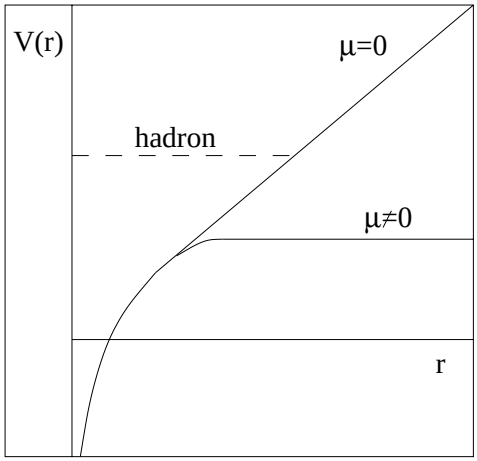

Figure 2.1: Color screening of the confining potential, figure from[92].

into infinite as r increases. Color screening thus transform a color insulator into a color conductor, turning hadronic matter into a quark matter, where the interactions between quarks and gluons become relatively weak and short range. We call this new phase of strongly interacting matter the Quark-Gluon Plasma (QGP) [91].

In relativistic thermodynamics, higher densities can be obtained either by increasing the net baryon number density, or by "heating" the system which will produce further hadrons through collisions. This result in a "T-μ_B" phase diagram of strongly interacting matter as shown in Fig.2.2, where μ_B is the baryon chemical potential. It is usually represented as a continuous curve connecting the high temperature transition region at $\mu_B = 0$ and the high baryon density region at $T = 0$. Also shown on the plot the regions that can be reached from the SIS to RHIC at different beam energy. At low temperature and high density, a diquark condensates may be formed, leading to the appearance of a "color-superconducting" phase, similar to the superconducting phase in QED, resulting from the Cooper pairs of electrons[8]. RHIC experiment might probe the near-zero baryon chemical potential and high temperature region. The region where $\mu_B = 0$ is believe to exist in the early universe.

For the study of critical behavior, long range correlations and multiparticle interactions are important, hence perturbation theory (pQCD) cannot be used. Only numerical lattice QCD (lQCD) methods [64] can provide reliable predictions for the

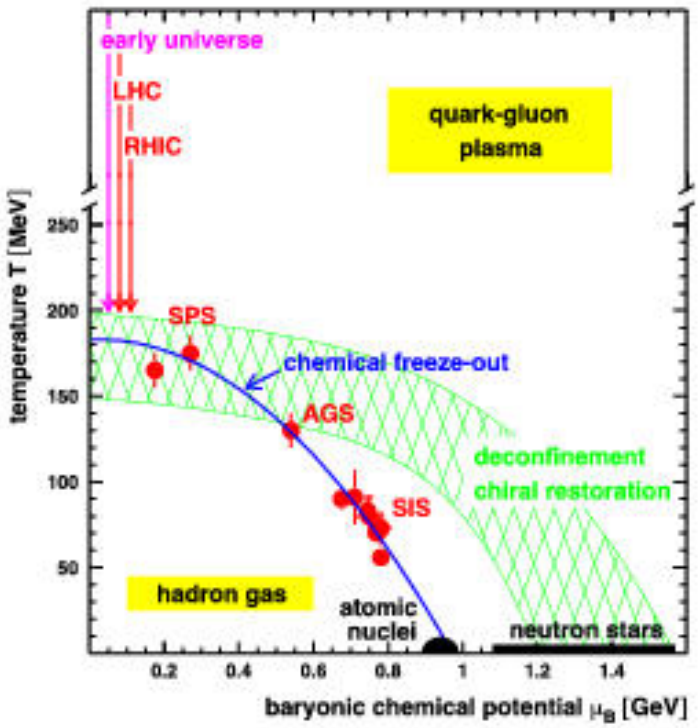

Figure 2.2: The phase diagram of strongly interacting matter, figure from[17].

thermodynamic properties of the QGP phase of the matter. This method is so far valid only for the case of vanishing net baryon number density.

In Fig.2.3 (left), a plot of the energy density, ϵ scaled by T^4 is shown vs. temperature, T for different light quark flavours as well as two light and a heavier quark. This variable ϵ/T^4 is roughly proportional to the number of particle degrees of freedom important at the energy scale corresponding to T. The curves clearly reflect the strong changes in the number of degree of freedom when going through the transition. At high temperatures, the degrees of freedom are roughly that of a massless gas of quarks and gluons. In the limit of very high temperature, we expect them asymptotically approach the Stefan-Boltzmann free gas limit, indicated by the arrows in Fig.2.3 (left) At low temperatures, the number of degrees of freedom is small and consistent with a gas of pions. A sharp transition occurs between the meson system and that of the quarks and gluons where ϵ/T^4 changes by an order of magnitude.

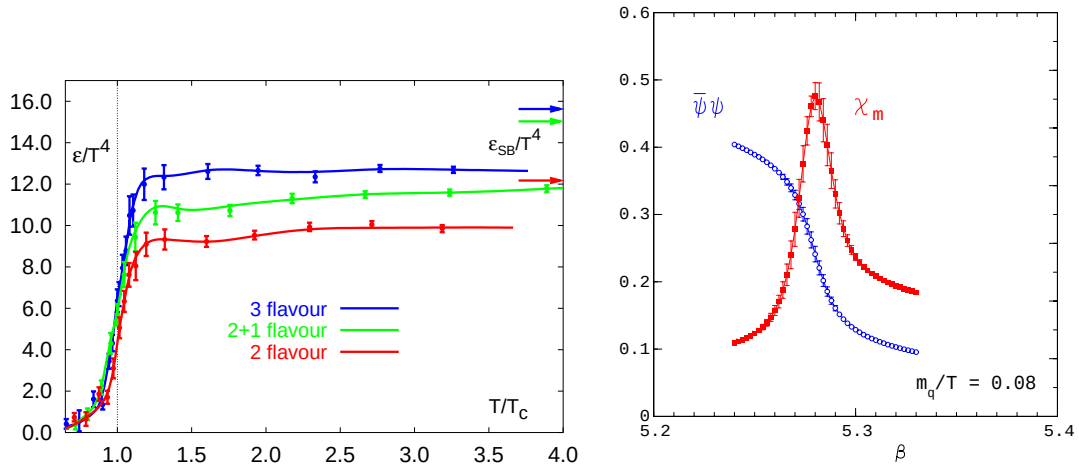

Figure 2.3: Lattice QCD results, (left) the energy density in QCD[64], arrows show the ideal gas values; (right) order parameter for chiral symmetry breaking in the chiral limit ($m_q \to 0$) and its susceptibility $\chi_m = \frac{\partial}{\partial m_q}\langle\bar{\Psi}\Psi\rangle$ as a function of the coupling $\beta = 6/g^2$[64].

The origin of the proton and neutron mass is one of the mysteries of QCD. The masses of the up and down quarks inside a proton are only a few percent of the nucleon mass. It is believed that this mass is obtained by breaking of a chiral symmetry of the strong interactions. The symmetry is broken at low temperature but will restore at high temperature. A measure of this symmetry breaking is $\langle\overline{\Psi}\Psi\rangle$, the typical value of a condensate which is composed of quark-antiquark pairs. At low temperatures, this is non-zero, and rapidly goes to zero at the phase transition temperature, as shown in Fig.2.3 (right). The nucleon mass is proportional to this condensate, and so it goes to zero in the Quark Gluon Plasma phase. This mass shift transition in QCD is often referred to as chiral symmetry restoration. It can but does not have to coincide with deconfinement transition.

2.1.2 Nucleus-Nucleus Collisions

The rapid growth in this field in the past two decades was to a very large extent stimulated by high energy nuclear collisions which produce in the laboratory strongly interacting matter large enough and long-lived enough for a study of statistical QCD. By varying the bombarding energy as well as projectile and target combinations, it

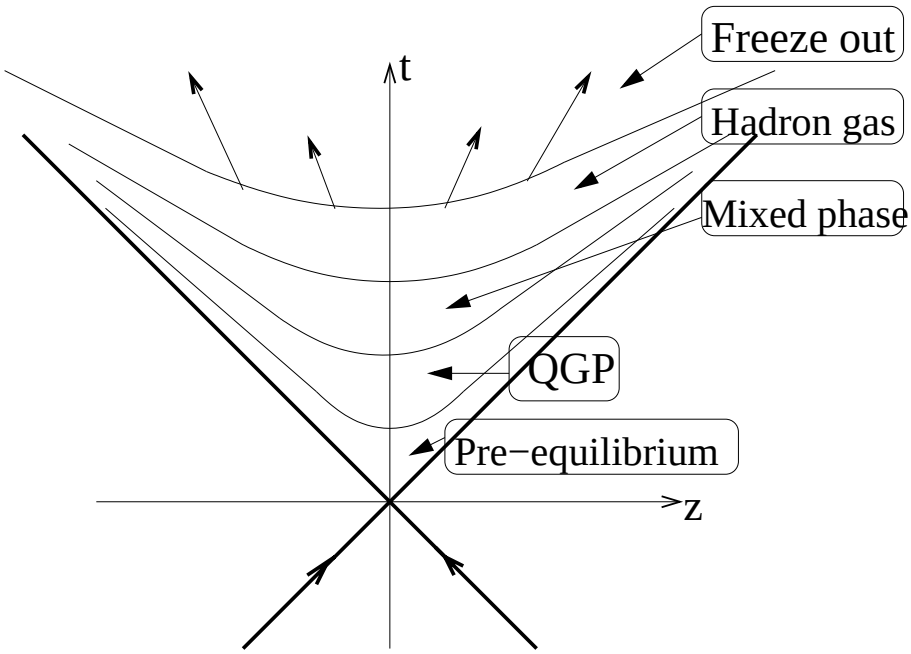

Figure 2.4: The space-time picture of nucleus-nucleus collisions.

is possible to create systems of different energy and baryon density.

The head-on collision of two nuclei can be represented as two thin disks approaching each other at high speed due to the Lorentz contraction. For Au+Au collisions the size of each "disk" in the direction transverse to the beam axis is about 7fm. In a low energy nucleus-nucleus collision, the two nuclei will remain intact and simply "bounce off" each other. With increasing energy, they will penetrate each other more and more, leading to highly excited nuclear matter, which rapidly breaks up into nuclear fragments and some additional mesons. If the collision energy increase further, nuclear transparency begins to set in: the two colliding nuclei pass through each other, leaving behind them a "fireball" of deposited energy, which eventually decays into hadrons.

The different stages of a nuclear-nuclear collision can be illustrated in the space-time diagram as Fig.2.4 with the space coordinate z and the time coordinate t. Thick lines represent the trajectories of the colliding projectile nucleus and the target nucleus, respectively.

The Relativistic Heavy Ion Collider (RHIC) at BNL is currently studying Au + Au collisions with center of mass energy $\sqrt{s_{NN}} = 200$ A GeV. At RHIC energies most of the baryons are expected to be carried away by the receding nucleons (the fragmentation region) while in the region of the collision a large energy (density) is deposited in the form of quark pairs and gluons. Therefore, the collision region is a system with high energy density and small net baryon density, which is similar to the condition in the early universe.

2.1.3 Collision Evolution and Dynamics

Nuclear collisions produce dense matter in a highly dynamical environment and the produced matter expands anisotropically near the speed of light. Before a collision, the partons of the two colliding nuclei are locked into a coherent field configuration. After the nuclear valence quark disks pass through each other the nuclear QCD field continue to interact which spans a space-time hypersurface over a proper time $\sqrt{t^2 - z^2} \sim 30\text{fm/c} = 10^{-22}\text{sec}$. The field then hadronize in a way that is still not well understood. The dense final hadronic matter can further interact as it expands toward the detector. The collision evolution process thus can be summarized as:

- Initial Conditions: Creating an incoherent gas of gluons from the initial nuclear field,
- Parton Transport: Evolution of the created parton gas toward equilibrium,
- QGP evolution: Equilibrated QGP evolutes and finally converts (hadronizes) into hadronic gas,
- The dense hadronic matter expands until the final state interactions cease and the observed final state hadrons "freeze-out".

There exists unfortunately no complete computable dynamic theory that consistently takes into account all elementary processes mentioned above. QCD is believed to be the theory, but it is still not computable except at high p_t where perturbative

or classical methods may apply. Two generic approaches to A+A can be classified by whether the initial conditions are (1) fit by extrapolating final observables backwards via a suitable dynamical scenario, or (2) computed via pQCD or classical Yang Mills(cYM) and subsequent evolution followed by a dynamical scenario. At lower energies (AGS, SPS) only the first approach is available since the momentum scales are simply too low to apply either pQCD or cYM. At collider energies (RHIC and beyond), the production of mini-jets [103, 102, 48] with $p_t > p_0 \sim 2\text{GeV}$ makes it possible for the first time to pursue the second approach via pQCD.

Microscopic models were intended to describe nucleus-nucleus collisions based on a superposition of elementary hadronic interactions and thus provide a description of what we would expect in a hadronic system without a QGP.

Almost every model started from independent, incoherent collisions between the interaction elements (hadrons or partons), and then included the effects of rescattering and coherence through string fusion, color ropes, quark droplets, interacting baryon junctions [53, 2, 1]. "Independence" here means that the successive collisions of a projectile nucleon with the target nucleons do not influence each other. "Incoherence" means that adjacent nucleons in the projectile do not influence each others' interactions with the target nucleons.

Hadronic cascade models are ideal tools for describing the late stages of heavy-ion collisions, the chemical and thermal freeze-out of hadrons when the dense phase is over. At RHIC and LHC energies, the conditions for applicability of perturbative QCD during the very early stages of a collision will be reached. The perturbative cascade has to be followed by a hadronization model and then an evolution of the dilute hadronic phase.

pQCD

The computable lowest order pQCD differential cross section for inclusive $p+p \to h+X$ invariant cross section is given by

$$E_h \frac{d\sigma_{hard}^{pp\to h}}{d^3p} = K \sum_{abcd} \int dx_a dx_b f_{a/p}(x_a, Q_a^2) f_{b/p}(x_b, Q_b^2) \frac{d\sigma}{d\hat{t}}(ab \to cd) \frac{D_{h/c}(z_c, Q_c^2)}{\pi z_c}, \quad (2.3)$$

where $x_a = p_a/P_A, x_b = p_b/P_B$ are the initial momentum fractions carried by the interacting partons, $z_c = p_h/p_c$ is the momentum fraction carried by the final observable hadron, $f_{a/p}(x_a, Q_a^2)$ is the proton structure function for parton of flavor a, and $D_{h/c}(z_c, Q_c^2)$ is the fragmentation function for the parton of flavor c into h. At very high energies classical Yang Mills theory[73, 3, 74] provides a general method which reduces to pQCD at high p_t.

Relativistic Hydrodynamics

The other approach, trying to "fit" the initial conditions by extrapolating the final distributions backwards with a suitable dynamical model has been traditionally based on relativistic hydrodynamics[67, 58, 16]. The central assumption is that thermal and chemical equilibrium are maintained locally in spite of the possible large gradients in the fluid variables. The approximate longitudinal boost invariant boundary conditions at ultra-relativistic energies simplify hydrodynamic equations greatly as pointed out by Bjorken[9]. For $\mu_B = 0$ the hydrodynamic equations are

$$\begin{aligned} \partial_\mu T^{\mu\nu} &= 0 \ , \ T^{\mu\nu}(x) = u^\mu u^\nu (\epsilon + P) - g^{\mu\nu} P \\ \partial_\mu j_i^\mu &= 0 \ , \ j_i^\mu(x) = n_i u^\mu \end{aligned} \quad (2.4)$$

where $\epsilon(x), P(x)$ and $n_i(x)$ are the proper energy density, pressure and number density of charge i in the local rest frame of the fluid, and $u^\mu(x)$ is the four velocity field of the fluid. The great advantage of hydrodynamics is that it provides a covariant dynamics depending only on the equation of state $P(T(x))$ that is directly related to the lattice QCD (lQCD) predictions. When a specific space-time freeze-out hypersurface is assumed together with the assumption, the Cooper-Frye

prescription[45, 27], the computed four fluid velocity field can be used to predict the final anisotropic flow pattern of hadrons. Since this process is assumed to be reversible, the final distributions together with an assumed freeze out hypersurface can be used to compute the initial conditions on any desired initial hypersurface. The disadvantage of this approach[75] is that both the initial and final freeze-out hypersurfaces must be guessed. Also finite mean free path in reality is outside the scope of ideal hydrodynamics, and transport theory solution[75] do not support "sharp" freeze-out hypersurfaces. In spite of some of the theoretical problems, initial conditions for RHIC have been successfully constructed by ideal hydrodynamics which reproduce very well many of the low p_t observables at RHIC[18, 56]. Some recent development tries to determine the initial state by using some other model to calculate it, e.g. event generators[93] or perturbative QCD calculations[63].

2.2 Collective Flow in Heavy-Ion Collisions

The macroscopic properties of nuclear matter under extreme conditions should be visible most clearly in collective features of the available data[88, 80], which arises naturally from the many collisions in a heavy-ion interaction but is absent from elementary processes. Here, the term collectivity denotes a common feature that is observed for several particles emerging from one reaction. Collective flow is the prototype of such a common feature and describes the movement of a large number of ejectiles either in a common direction or at a common magnitude of velocities. Restricting this very general definition of collective behavior to kinematic observables leads to the definition of collective flow:

- "Longitudinal flow" describes the collective motion of the particles in their original direction defined by the beam.

- "Radial flow" characterizes particles that are emitted from a source with a common velocity field independent of the direction, i.e. a velocity field with spherical symmetry.

- "Transverse flow" is the term used whenever the velocity field is found to be independent of the azimuthal angle.
- "Anisotropic flow" describes an emission pattern in which particles are found to be preferentially emitted with respect to a certain azimuthal angle .

All forms of flow are interrelated and represent different parts of one global picture. We study elliptic flow in this analysis which belongs to anisotropic flow.

2.2.1 Anisotropic Flow in Non-central Collisions

The physics interpretation of non-central collisions is more complicated than that of very central collisions, since the azimuthal symmetry is no longer present in the initial state of the interaction. Every event should therefore ideally be analyzed with respect to this initial azimuthal asymmetry, which would be fully determined by the orientation and the size of the impact parameter. We define the plane expanded by the impact parameter vector and the momentum vector of the projectile as the "reaction plane".

Non-central collisions offer additional observables due to their deformed, almond shaped overlap region, which can lead to angular dependencies (relative to the reaction plane) of final state observables which do not appear in central collisions with azimuthal symmetry [81]. Microscopically, large anisotropies in momentum space perpendicular to those in configuration space arise only if there is strong rescattering already in the first moments ($\sim$ fm/c) of the collision, and in a hydrodynamical picture (anisotropic) pressure gradients are building up in the transverse plane, determining the subsequent evolution of the matter. The stronger forces in the direction of steepest pressure gradients lead to more transport of matter in those directions which eventually even out the differences between the radial gradients in the short and long direction of the initial almond, see Fig2.5. Thus anisotropies observed in the final state are built up early and in the hottest stages of the collision, as the cause of these anisotropies disappears during the system's evolution (on a timescale of less than $\sim$ 4 fm/c [96, 7, 83]).

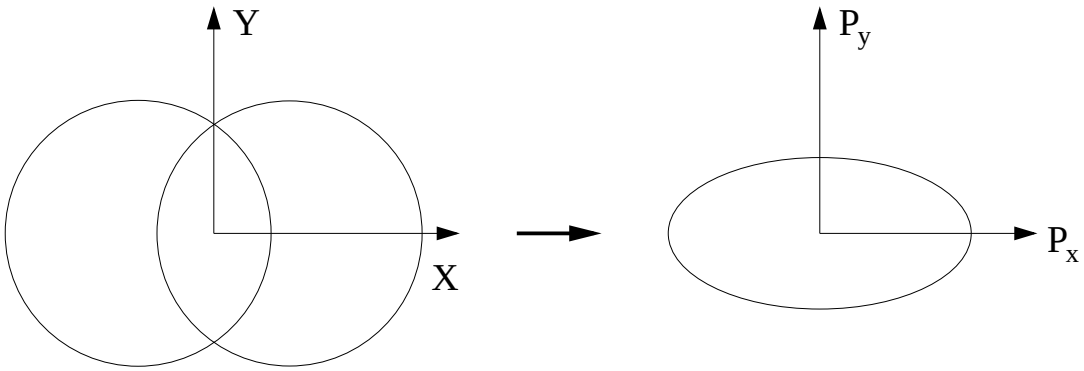

Figure 2.5: From initial spatial anisotropy (left) to final state momentum anisotropy (right) in non-central collisions

Anisotropic flow is defined as azimuthal asymmetry in particle distribution with respect to the reaction plane. It is convenient to characterize the magnitude of this asymmetry using Fourier decomposition of the azimuthal distributions. Then the first harmonic describes the so-called directed flow, and the second harmonic corresponds to elliptic flow. The word "elliptic" comes from the fact that the azimuthal distribution with non-zero second order harmonic represents an ellipse. Elliptic flow characterize the anisotropic emission of particles "in" or "out" of the reaction plane. Non-zero higher harmonics can be also presented in the distribution. The corresponding Fourier coefficients, v_n, are used to quantify the effect[101, 86].

Elliptic flow is a correlation between the azimuth ϕ of an outgoing particle and the azimuth Φ_R of impact parameter [101],

$$v_2 = \langle e^{2i(\phi - \Phi_R)} \rangle, \tag{2.5}$$

where brackets denote a statistical average. It is usually characterized in terms of particle momenta as

$$v_2 = \left\langle \frac{{p_x}^2 - {p_y}^2}{{p_x}^2 + {p_y}^2} \right\rangle. \tag{2.6}$$

The initial "ellipticity" of the overlap zone is usually characterized by the quantity

$$\varepsilon = \left\langle \frac{x^2 - y^2}{x^2 + y^2} \right\rangle, \tag{2.7}$$

assuming the reaction plane being xz-plane.

In contrast to this self-quenching effect e.g. for elliptic flow, other dynamical quantities such as radial flow continue to grow until freeze-out and carry information about the full expansion stage. This makes elliptic flow particularly sensitive to the early stages of the system expansion[97].

Changing the centrality leads to a varying number of participating nucleons and a changing size of the interaction region. The amount of energy deposited in the collision region as well as the energy density in the system will be largest in central collisions and decrease with increasing impact parameter.

Anisotropic flow has been measured in relativistic nuclear collisions[88, 23]. Theoretic calculations and Monte Carlo simulations, for SPS and RHIC energies, has been done over a variety of frameworks: hydrodynamics[81], the low density limit of kinetic theory[52], parton cascade[7], hadronic cascade codes[96], pQCD jet quenching[103] and color glass condensate[73].

Cascade calculations based on the incoherent scattering of classical on shall particles and the low density limit of classical kinetic theory are expected to work best for peripheral collisions where the density of produced particles is sufficiently low and only a few rescattering occur. Central collisions produce higher particle densities where the hydrodynamic limit may be more suitable.

Hydrodynamic Elliptic Flow

The evolution of a hydrodynamical system is determined by its initial conditions and equation of state (EOS). The initial conditions can be fixed by requiring a good fit to the p_t spectra of particle distributions in central collisions. Including phase transition or not and different freeze-out temperature lead to different equation of state. The p_t averaged elliptic flow v_2 as a function of collision centrality is shown in Fig.2.6 (left) for Au+Au collision at $\sqrt{s_{NN}}$=130 GeV at RHIC. The data points are from STAR experiments including all charged particles with $|\eta| < 1.3$ and $0.1 < p_t < 2\text{GeV}/c$. Hydrodynamics successfully reproduces the elliptic flow measured at RHIC for central and semi-central collisions. Fig.2.6 (right) shows the

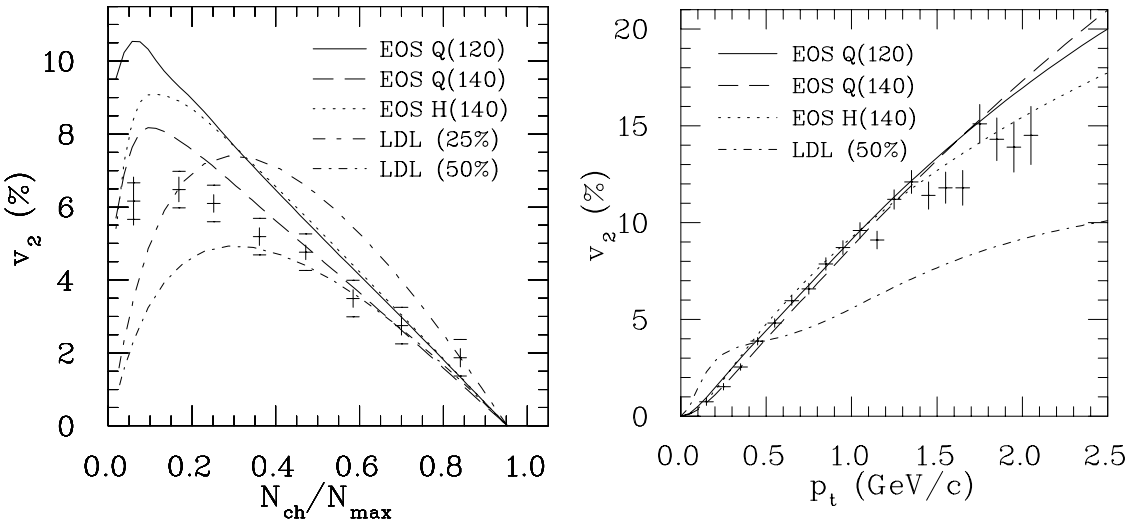

Figure 2.6: Elliptic flow coefficient v_2 for charged particles from Au+Au collisions at $\sqrt{s_{NN}}$=130A GeV from hydrodynamic calculation[56] and RHIC STAR experiment[23], left panel shows centrality dependence, right panel shows p_t dependence. The letters Q and H in the labels stand for an EoS with a first order phase transition and a hadron gas EoS without a phase transition, respectively. Numbers in parentheses stand for the freeze-out temperature in MeV. For Low Density Limit, LDL, numbers in parentheses stand for the fraction of final charged multiplicity arise from resonance decays, figure from[56].

p_t dependence of elliptic flow for minimum bias Au+Au collisions at RHIC. It is calculated by

$$v_2(p_t) = \frac{\int b\,db\,v_2(p_t;b)\,\frac{dN_{\rm ch}}{dy\,p_t\,dp_t}(b)}{\int b\,db\,\frac{dN_{\rm ch}}{dy\,p_t\,dp_t}(b)}, \tag{2.8}$$

with a cut-off at $b_{max} = 13.5$fm. The data agree well with hydrodynamical calculation at low p_t. For p_t above about 1.5GeV/c the measured elliptic flow lag behind the hydrodynamic prediction, indicating departure from thermalization for high p_t particles. The hydrodynamic curves start out quadratically at low p_t, then quickly turn over to an approximately linear rise and keep increasing monotonically with p_t, eventually saturated at $v_2(p_t) = 1$ as $p_t \to \infty$. The influence of the initial spatial anisotropies in terms of a hydrodynamic picture represents the limiting case of maximum response to the initially produced pressure gradients due to strong (infinite) rescattering already at the early stages of the expansion. Such an approach seems appropriate at RHIC energies [56] and is valuable to understand the global (macroscopic) characteristics of the expansion stage of an ultra-relativistic heavy ion

collision. The rapidity dependence can be studied by relaxing the boost invariance assumption and using a genuinely three dimensional model[57].

2.2.2 Transverse Flow in Central Collisions

For central collisions a dense zone of compressed nuclear matter is formed. It is the pressure that drives the system apart. Only the particles on the surface of the hot and dense zone are likely to decouple early. Particles on the inside undergo frequent collisions with each other. Their motion becomes less random because collisions with other particles toward the inside and toward the outside have different probabilities. In this way, a net collective velocity is attained on the freeze-out surface at each moment in time. For symmetric systems, the investigation of transverse mass or of kinetic-energy spectra at midrapidity of particles with different mass yields information on the collective transverse expansion of the emitting source. We can fit the transverse mass spectra with a simple exponential distribution

$$\frac{dN}{m_t dm_t} \propto \exp\left(-\frac{m_t}{T}\right) \tag{2.9}$$

and interpret the inverse slope parameter T as the combination of apparent temperature and the effect of collective flow of the emitting source[55], cf. Eqn.2.11.

2.3 Strangeness Production in Heavy-Ion Collisions

Particle production is, at all incident energies, a key quantity to extract information on the properties of nuclear matter under extreme condition. The study of strange particle production has consistently played an important role in revealing the production mechanisms in relativistic heavy-ion collisions. The K^0_S is a single strange meson with quark content ($d\bar{s}$) (or ($\bar{d}s$) for antiparticles). The Λ is a single strange hyperon with quark content (uds) and $\bar{\Lambda}(\bar{u}\bar{d}\bar{s})$ is its anti-particle.

In a hadronic scenario, strangeness particle can be produced through inelastic

collisions which will drive the system toward chemical equilibrium. A typical process of this type is $\pi^0 + \mathrm{p} \rightarrow \mathrm{K}^+ + \Lambda$. In a deconfined QGP, the $\mathrm{s\bar{s}}$ pair can be copiously produced through gluon fusion ($\mathrm{gg}\rightarrow\mathrm{s\bar{s}}$) because the coupling for gluon splitting into u, d or s quark-antiquark pairs are all equal and the energy threshold for these processes are much lower than those for strange hadron production. The enhancement of strangeness production was proposed as a probe for QGP phase transition[87].

In heavy-ion collisions, a strongly interacting system persists for some considerable time. There are many collisions, and these collisions provide the means for achieving equilibrium. Thermal equilibrium is driven by the total cross section, whereas chemical (flavor) equilibrium is driven by the inelastic cross section. What is measured in heavy-ion collisions is the set of abundances in the final stage, when hadronic final-state interactions cease. The equilibrium abundances for different particle species can be predicted in terms of the baryon-chemical potential μ_B, the strange chemical potential μ_s, and the temperature T. These define the standard partition function Z of statistical mechanics. The hadron abundances are then given by

$$N_j = \lambda_j \frac{\partial}{\partial \lambda_j} \ln Z(T, V, ...). \tag{2.10}$$

Here λ_j is the fugacity [68] for particle species j, given by $\lambda_j = \exp(-\mu_j/T)$. The average chemical potential μ_j is in turn given by $\mu_j = n_j^q \mu_q + n_j^s \mu_s$. n_j^q and n_j^s are the net numbers of non-strange and strange quarks, respectively, for species j.

The inverse slope, T, of the m_t spectra from all kinds of particles were measured at SPS energy, see Fig.2.7 and Eqn.2.9. For most of the particles, inverse slope (T) increase almost linearly with particle mass. This can be explained as the "fireball" expands with a certain velocity and all particles freeze-out at approximately the same temperature, then the slope parameter increases with the mass of the particle, i.e.

$$T = T_{\mathrm{thermal}} + m\langle\beta_t\rangle^2. \tag{2.11}$$

Although the heavier strange particles Λ and Ξ, along with their anti-particles, still can fit into the systematics, the slope of Ω and $\bar{\Omega}$ are significantly lower. A physical

scenario in which multi-strange baryons do not participate in a common expansion and thus decouple early from the collision system due to their small hadronic cross sections, was proposed to explain this observation[54]. This explanation suggests that it may be possible to obtain insight into very early stages of the collisions by studying the elliptic flow of strange particles.

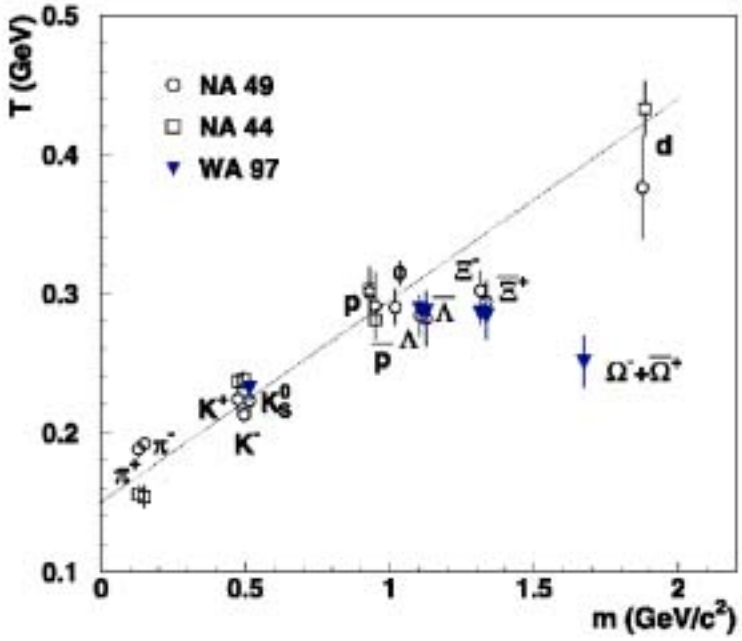

Figure 2.7: Inverse m_t slopes' dependence on particle mass in central Pb-Pb collisions at 158GeV/nucleon, figure from[71].

Chapter 3

Experimental Setup

3.1 RHIC Accelerator Complex

The Relativistic Heavy Ion Collider (RHIC)[10] consists of two concentric rings of superconducting magnets. It is constructed in an existing ring tunnel of ~ 3.8 km circumference located in the northwest section of the Brookhaven National Laboratory (BNL) site.

The major RHIC performance parameters are summarized in Table 3.1. The top kinetic energy will be 100×100 GeV/u for gold ions. At a $B\tilde{n} = 839.5$ T·m of the magnet system set for 100 GeV/u Au beams, the operational momentum increases with the charge-to-mass ratio, resulting in kinetic energies of 125 GeV/u for lighter ions and 250 GeV for protons. The collider will be able to operate over a wide range from injection to top energies. The collider is designed for a Au+Au luminosity of about 2×10^{26} cm^{-2}sec^{-1} at top energy, while maintaining the potential for future upgrades by an order of magnitude. The luminosity is energy dependent and decrease in first approximation proportional to the operating energy. The luminosity for lighter ions will be higher, with $\sim 1 \times 10^{31}$ cm^{-2}sec^{-1} for pp collisions. The collider will allow collisions of beams of equal ion species from Au-Au all the way down to p-p. It will also allow operation of unequal species such as protons on gold ions. The existing tunnel and the magnet lattice configuration provide six experimental areas where the circulating beams cross. The crossing point

configuration foresees head-on collisions, but allows crossing angles up to 1.7 mrad.

Physics Parameters		
No. Intersection Regions	6	
No. Bunches/ring	60	
Bunch Spacing (nsec)	213	
Collision Angle	0	
No. of Au-ions/bunch	1×10^9	
Operational lifetime Au	$\sim$ 10 h	
Diamond length	18 cm rms	
Beam separation in arcs	90 cm	
Acceleration time	75 sec	
Performance Specifications	**Au**	**P**
No. Particles/Bunch	1×10^9	1×10^{11}
Top Energy(Gev/u)	100	250
Luminosity, average($cm^{-2}sec^{-1}$)	$\sim 2 \times 10^{26}$	$\sim 1 \times 10^{31}$

Table 3.1: RHIC Physical Parameters and Performance Specifications

Bending and focusing of the ion beams are achieved by the ring magnets. The required field is generated with single-layer cosine-theta magnets which are contained in vacuum vessels separate for each ring, except those near the collision points. The beam tube in the superconducting magnets is at the temperature of liquid helium and an extremely good vacuum is required to avoid beam loss and radiation background.

The complete RHIC facility is a complex set of accelerators interconnected by beam transfer lines. Formation of the bunches occurs prior to injection. The existing accelerator complex at BNL consisting of Tandem Van de Graaff accelerators, the Booster synchrotron, and the Alternating Gradient Synchrotron (AGS), serve as the injector for RHIC.

The sequence of steps in the chain of accelerators is shown in Fig.3.1 for gold ions. Gold (Au) ions with charge -1 are generated in the Pulsed Sputter Ion Source

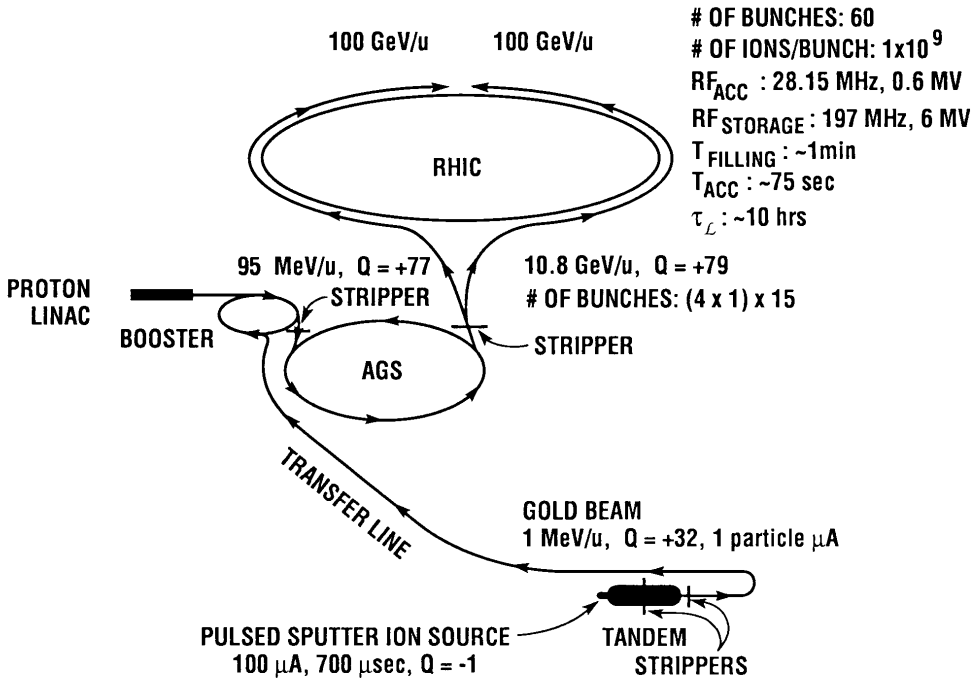

Figure 3.1: RHIC Acceleration Scenario for Gold

and initially accelerated in Tandem Van de Graaff accelerators. Passing through two stripping foil Au ions exit the Van de Graaff at kinetic energy 1 MeV/u and +32 charge. The beam from the Tandem is transferred to the Booster where it is accelerated to 95 MeV/u, stripped once again to +77 charge and then enter the AGS. In the AGS, the beam is accelerated to full energy, 10.8 GeV/u for gold and 28.3 GeV for proton. It is finally stripped from +77 to +79 charge before injection into the RHIC ring. Once injected into RHIC, the bunches are accelerated to collision energy and stored for data taking.

A radio frequency (rf) system are employed at RHIC to capture, accelerate and store the beam. The acceleration rf system operate at $\sim$ 26 MHz for capture of the injected beam, acceleration to top energy and bunch shortening at top energy. After having reached the operating kinetic energy the bunches are transferred from the acceleration to the storage rf system at 196 MHz. This frequency was chosen for sufficient longitudinal focusing to keep bunches short over 10 hours storage time. The beam will be dumped in a single turn (13 μsec) by activating the ejection kicker which deflects the beam horizontally onto a dump block.

Four of the six interaction regions are currently occupied by four experiments, BRAHMS, PHOBOS, PHENIX and STAR. The first commission run occurred in the summer of year 2000. The first beam-beam collision event at RHIC at collision energy of $\sqrt{s_{NN}} = 60$ GeV was recorded by STAR. A few weeks later, STAR recorded collisions at $\sqrt{s_{NN}} = 130$ GeV, which is the nominal beam energy for the year 2000 summer run. An end view of a central trigger event in the TPC is shown in Fig. 3.2. Tracks are reconstructed from online level-3 trigger.

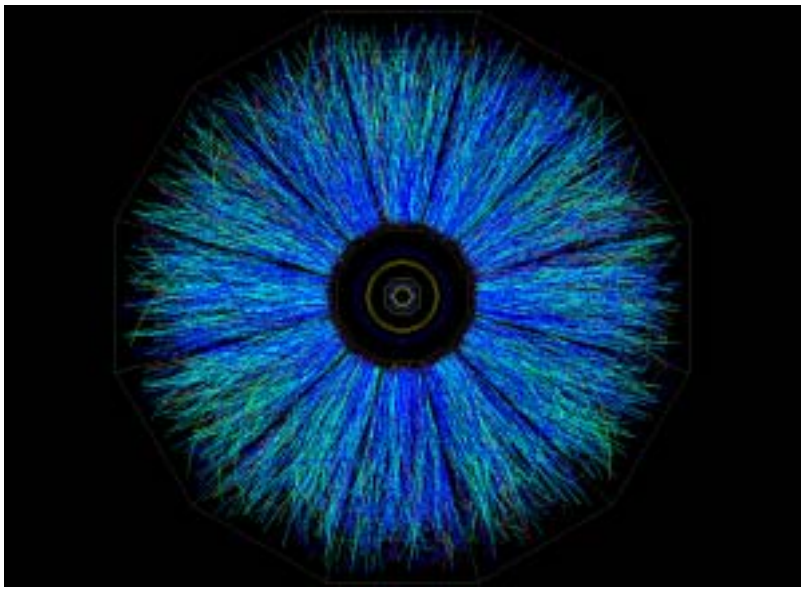

Figure 3.2: Central trigger event in STAR TPC view from beam direction

3.2 The STAR Detector

The STAR (Solenoidal Tracker at RHIC) detector is one of the two large detector systems at RHIC. It is designed to study pp, pA and AA collisions. It is a large acceptance cylindrical geometry detector system with complete azimuthal coverage over the central rapidity region, focusing on measurements of hadron production. STAR will measure many observables simultaneously on an event-by-event basis to study signatures of a possible QGP phase transition and the space-time evolution of the collision process at their respective energy.

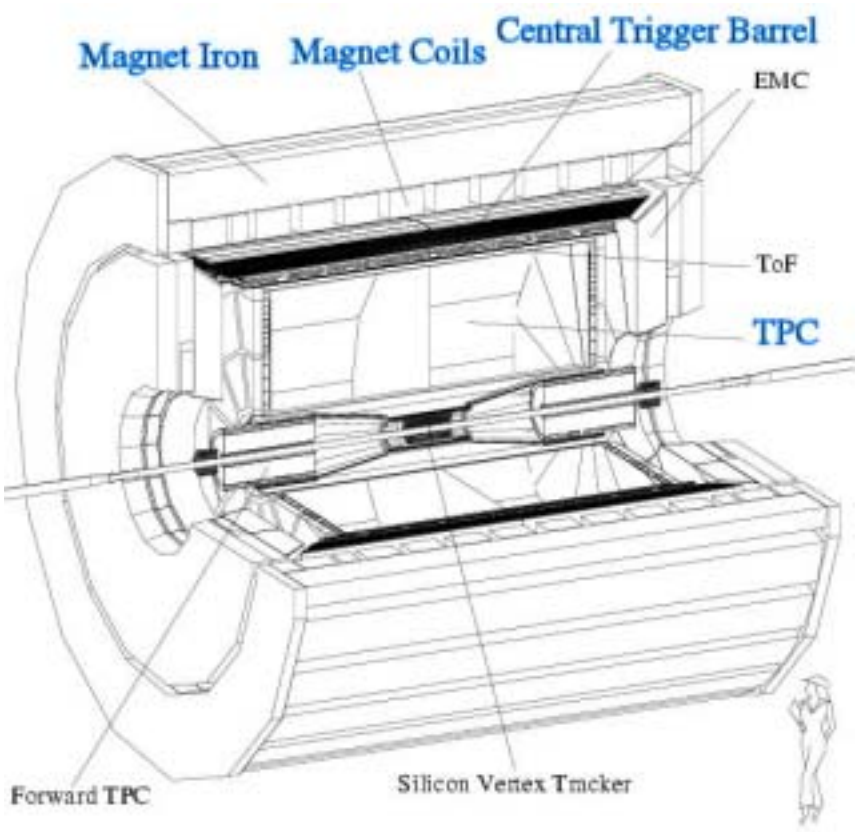

Figure 3.3: The STAR Detector

The configuration of the STAR detector is illustrated in Fig.3.3. It is designed primarily for measurements of hadron production over a large solid angle. The entire detector system is located within a 0.5 Tesla solenoidal analyzing magnet. Inside the magnet are detectors for tracking charged particles and an electromagnetic calorimeter for detecting photons and identifying electrons.

The RHIC colliding beams collide in the center of the detector and then move radially outwards from the beampipe. The primary tracking device at STAR is a large Time Projection Chamber (TPC)[21], which has a diameter of 4 m and a length of 4.2 m. It begins at 50 cm radially from the beam collision point and covers the pseudo-rapidity (η) region [-2, 2]. The TPC allows both momentum and particle identification information to be gathered, the latter accomplished by measuring the energy lose of a particle through the TPC's gas volume. Inside

of the main TPC, just outside the beampipe, is a 3-layer Silicon Vertex Tracker (SVT), which is based on silicon drift technology. It consists of three layers of ladders of silicon drift devices to provide three independent space points with a resolution of less than 50 microns and three samples of ionization for each track that traverses the device. The additional information from SVT will improves the momentum resolution and particle identification over using simply the TPC. The full SVT covers $|\eta| \leq 1$ with one layer covering $|\eta| \leq 2$. Along with the TPC there is one Forward Time Projection Chamber(FTPC) on each side, which provide charge and momentum information in the pseudorapidity range between $2.5 < |\eta| < 4.0$. A radial TPC scheme is used for FTPC, where ionization electrons drift in an electric field perpendicular to the axial solenoidal magnetic field. Outside the tracking, covering $|\eta| \leq 1$ is the barrel electromagnetic calorimeter (EMC). The STAR detector also includes endcap electromagnetic calorimeters that cover the magnet poletips between $1 < |\eta| < 2$. They will provide complete coverage for photons and electrons.

The STAR trigger is designed to operate at a number of levels, allowing more and more sophisticated decisions to be made as the information from various detectors becomes available for processing. For triggering on the nuclear collision geometry, the lowest level trigger system consists of a set of 240 scintillator slats surrounding the main TPC forming the Central Trigger Barrel (CTB) and two Zero Degree Calorimeters (ZDC) located 18 meters up and downstream along the beam direction. The CTB measures charged particle multiplicity in these segments of η and ϕ via the analog pulse height of the photomultiplier output. The ZDCs measure beam-like neutrons from the fragmentation of colliding nuclei. Displayed in Fig.3.4 is the correlation between the summed ZDC pulse height and that of the CTB for event with a successfully reconstructed primary vertex in TPC. The largest number of events occurs for large ZDC values and small CTB values, which corresponds to collisions at large impact parameters. A minimum bias trigger was obtained by selecting events with a pulse height larger than that of one neutron in each of the forward ZDC's which corresponds to 95% of the geometrical cross section. The design of the ZDCs is the same for all RHIC experiments, allowing for a meaningful

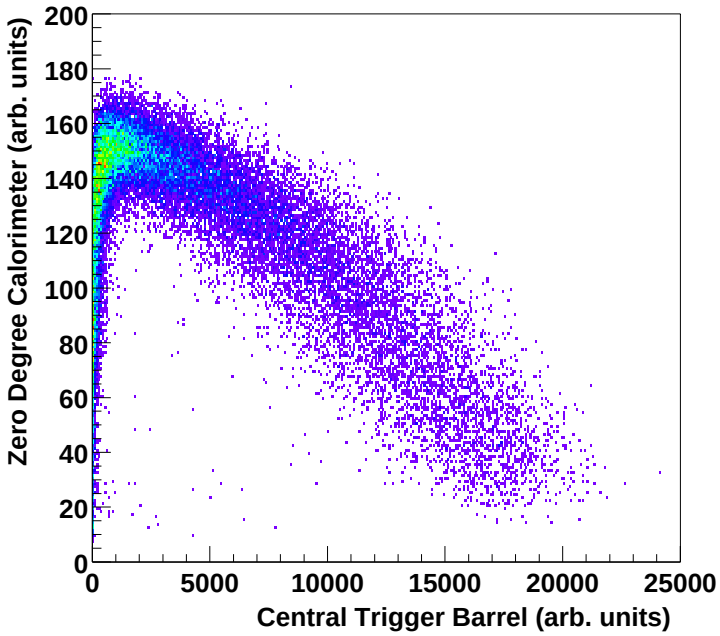

Figure 3.4: Correlation between ZDC and CTB for events with successfully reconstructed primary vertex in TPC

comparison of event centrality among RHIC experiments.

During the first year (year 2000) of data taking, the STAR experimental setup consisted of the TPC, CTB, two ZDCs and a small acceptance Ring Imaging Cherenkov (RICH). The TPC operated in a 0.25 Tesla solenoidal magnet and gives tracking information for charged particles in a pseudorapidity interval of approximately $|\eta| < 1.8$. Particle identification at higher momenta was made possible using RHIC. The RHIC covers only a narrow acceptance window centered at mid-rapidity ($\delta\phi = 20^\circ$ in azimuth and $|\eta| < 0.3$), thus its measurements in year-1 were statistics limited.

The design of STAR detector make it possible to measure many quantities on an event-by-event basis, so that events can be categorized and correlated based on these characteristics. For the first year, STAR has detected all quantities listed in table 3.2, as well as the π^0. With EMC we can measure a) π^0, η distributions, b) High p_t particles and jets.

Hadronic Observables	
a) Charged hadrons:	$p, \bar{p}, \pi's, K's, \Xi^+, \Xi^-, \Omega^+, \Omega^-, d, d$
b) Neutral hadrons:	$\Lambda, \bar{\Lambda}, K^0_S, \phi, \rho, K^*, \bar{K}^*$
c) Spectra:	p_t, particle ratios, slope parameters
d) Collision Geometry:	Flow, HBT, E-by-E correlations, Event Multiplicity

Table 3.2: Quantities detected in STAR for year one

3.3 The STAR Time Projection Chamber

The STAR TPC measures 4 m in diameter by 4.2 m long, making it the largest TPC in the world. As the primary tracking device[22] in STAR, the TPC records the tracks of particles, measures their momenta, and identifies the particles by measuring their ionization energy loss (dE/dx). Particles are identified over a momentum range from 100 MeV/c to greater than 1 GeV/c and momenta are measured over a range of 100 MeV/c to 30 GeV/c.

TPC is divided into two longitudinal drift regions, each 2.1 m long, with a high voltage cathode located at the center, as shown in Fig.3.5. Charged particles can be detected in drift chambers because they ionize the gas along their flight path. Electrons created from track ionization will drift in the longitudinal direction, along the TPC electric field lines, toward either end-cap of the TPC, depending on their point of origin, where their time of arrival and location are recorded.

The uniform electric field is defined by a thin conductive Central Menbrance (CM) at the center of the TPC, concentric field cage cylinders and the read out end caps. The central membrance is operated at 28 kV and the end caps are at ground. The field cage cylinders provide a series of equi-potential rings that divide the space between the central membrance and the anode planes into 182 equally spaced segments. Electric field uniformity is critical since any distortions in the field will result in a distortion of the recorded tracks. The field cage cylinders serve the dual purpose of both gas containment and electric field definition. The

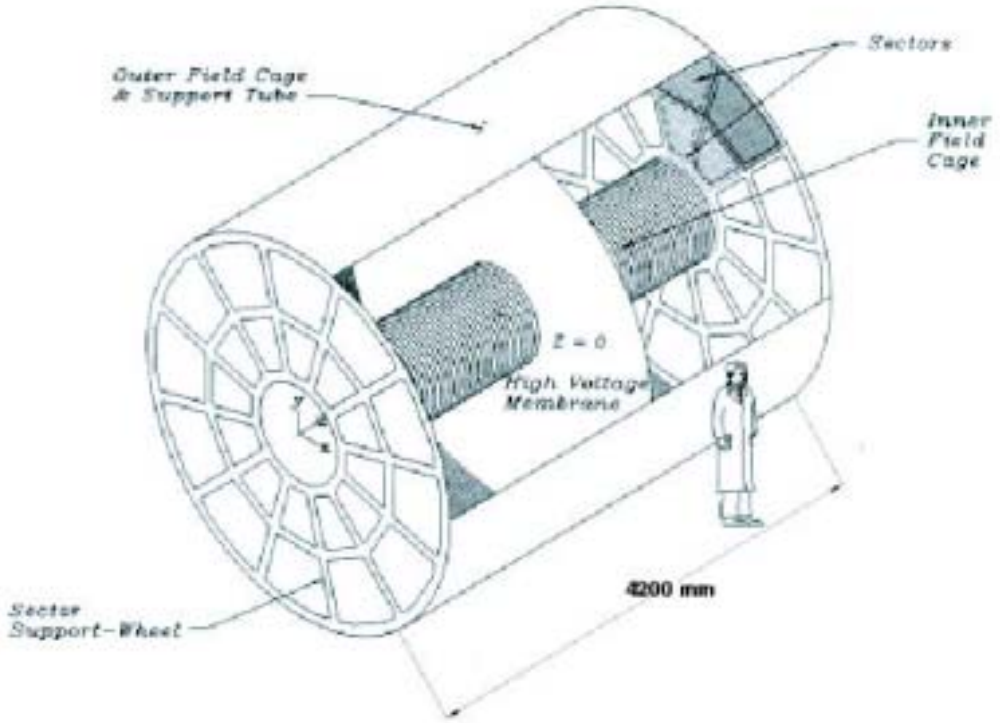

Figure 3.5: STAR TPC

mechanical design has been optimized to reduce mass, minimizing track distortions from multiple coulomb scattering and reducing background from secondary particle production.

Located on the ends of the TPC, the readout planes consist of Multi-Wire Proportional Chamber (MWPC) with pad readout. Each end-cap is instrumented with 72,000 pads which give xy coordinate information. The TPC is divided into 24 super sectors, each subsequently divided into an inner and outer sector. Two pad size are used, one for the inner sectors (50 cm<radius<125 cm) and one for the outer sectors (125 cm<radius<200 cm). Each pad will be read out into 512 time samples which give z-position for each hit. The chambers have four components, a pad plane connected to the front end readout electronics and three wire planes, see Fig.3.6.

Different pads designs are used for inner and outer radius, see Fig.3.7. The outer radius sub-sectors have continuous pad coverage to optimize the dE/dx res-

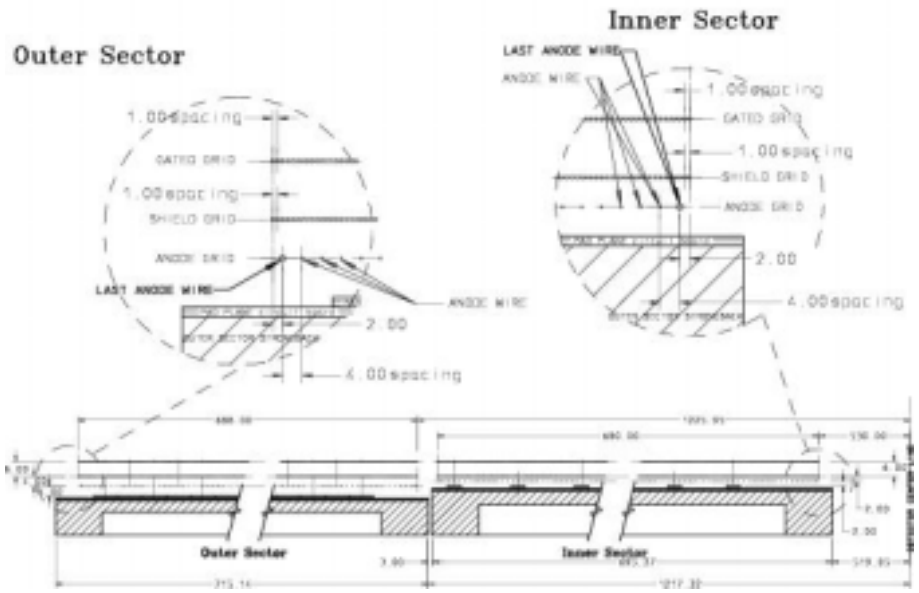

Figure 3.6: A cutaway view of an outer sub-sector pad plane

olution(*i.e.* no space between pad rows). For the inner radius region of the TPC, where track densities are high, a sub-sector design have been used to improve the two track resolution.

The three wire planes are the gating grid, the ground grid, and the anode grid. The ground grid and gating grid help to define the drift field of the TPC. The anode wires are biased to a high voltage to provide the necessary electric field to avalanche the electrons from the track ionization. The outermost wire plane on the sector structure is the gating grid located 6mm from the ground grid. This grid is a shutter to control entry of electrons from the TPC drift volume into the MWPC. It also blocks positive ions produced in the MWPC from entering the drift volume where they would distort the drift field. It is transparent to the drift of electrons while the event is being recorded and closed in the rest of the time. The ground grid lies between the anode wires and the gating grid. It helps to define the anode wire avalanche cells and shield the pad plane and anode grid from feeling the full impact of the gating grid noise.

P10 (90% Argon + 10% Methane) is the working gas in TPC. The gas sys-

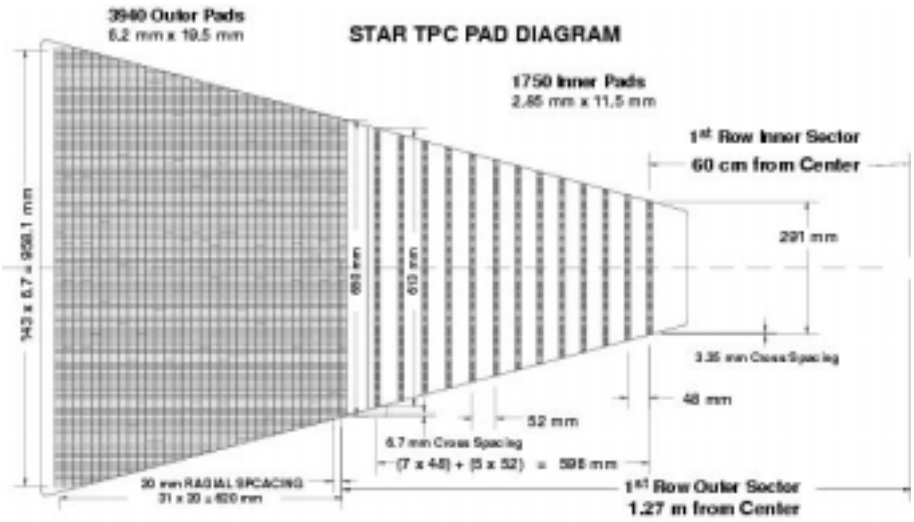

Figure 3.7: The anode pad plane with one full sector shown

tem circulates the gas in the TPC and maintains purity, reducing electro negative impurities such as oxygen and water which capture drifting electrons.

The tracks of a primary particle passing through the TPC is reconstructed by finding ionization clusters along the track. The x and y coordinates of a cluster are determined by the charge measured on adjacent pads in a single pad row. (The local x axis is along the direction of the pad row, while the local y axis extends from the beamline outward through the middle of, and perpendicular to, the pad rows. The z axis lies along the beam line.) The z coordinate of a point inside the TPC is determined by measuring the time of drift of a cluster of secondary electrons from the point of origin to the anodes on the endcap and dividing by the average drift velocity. To minimize the variations in drift velocity, the cathode voltage are set so that the electric field in the TPC corresponds to the peak in the drift velocity curve. Typical drift velocity in STAR TPC is 5.45 cm/μs.

The discrete signals from each sector are delivered to DAQ from 6 readout cards and the data from each read-out card are then send to a DAQ receiver card via an optical fiber. TPC readout starts after the L_0 trigger latency ($\sim$ 1 μs). In the DAQ, these data are processed, including pedestal subtraction, gain correction and zero suppression etc. Data from each detector subsystem are assembled together for

recording and distribution. Combined with the L3 trigger system, the DAQ allows event selection based on physics criteria. Compared to the beam crossing rate, the STAR TPC data-taking is relatively slow due to the event size. The trigger system will allow us to look at every RHIC crossing and decide whether or not to initiate recording that event.

Chapter 4

Analysis Methods

4.1 Event Reconstruction in the STAR TPC

Tracking software will associate space points to form tracks and fit the points on a track with a track-model to extract particle information, such as the momentum. The track-model is a 3D helix with energy lose and multiple scattering effects in the gas which will deviate a particle trajectory slightly from the helix. For year 2000 run we only get track information from TPC. The tracking efficiency depends on the acceptance of the detector, the electronics detection efficiency, as well as the two-hit separation capability of the system. Embedding simulation studies' results indicate that the systematic error on the tracking efficiency is about 6%. Fig.4.1 shows the pion reconstruction efficiency in Au+Au collisions with different multiplicities as a function of the transverse momentum of the primary particle[17]. In high multiplicity events it reaches a plateau of 80% for high p_t particles. Below 300 MeV/c the efficiency drops rapidly because the primary particles spiral up inside the TPC and donot reach the outer field cage. In addition, these low momentum particles interact with the beam pipe and the inner field cage before entering the tracking volume of the TPC. The overall track reconstruction efficiency, finding and accurate track parameter determination, is a very critical parameter in the strangeness reconstruction.

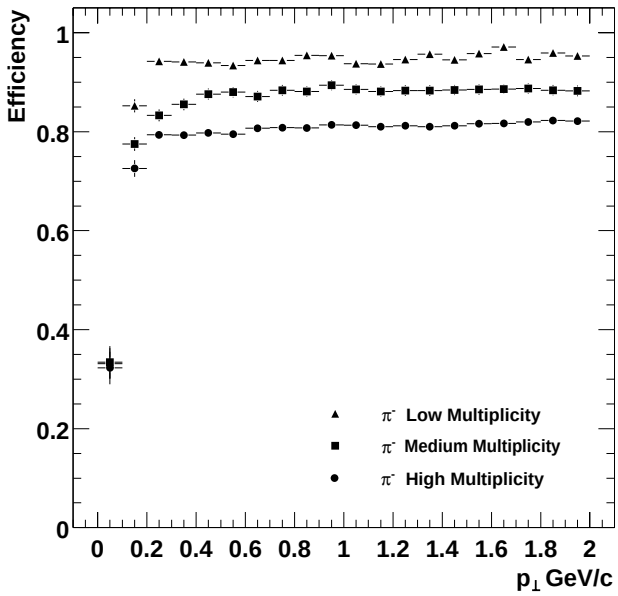

Figure 4.1: The pion tracking efficiency in STAR for central Au+Au events at RHIC for different multiplicity in a 0.25T magnetic field, figure from[60].

4.1.1 Helix Model

In principle five parameters are needed to define a helix. A 3D helix track-model suitable for STAR geometry and magnetic field to the first order can be parameterized as

$$\begin{aligned} x &= x_0 + R\left(\cos(\Phi(s)) - \cos(\Phi_0)\right) \\ y &= y_0 + R\left(\sin(\Phi(s)) - \sin(\Phi_0)\right) \\ z &= z_0 + s\sin\lambda \end{aligned} \tag{4.1}$$

where R is the radius of the curvature, $\Phi_0 = \Psi - h\pi/2$ is the azimuthal angle of the starting point, $h = -\text{sign}(qB)$ is the sense of rotation of the projected helix in the xy-plane, q is the charge of the particle in units of positron charge, B is the z component of the homogeneous magnetic field ($\vec{B} = (0, 0, B)$) and $\Phi(s) = \Phi_0 + h(s/R) * \cos(\lambda)$, s is the path length along the helix, x_0, y_0, z_0 is the starting point at $s = 0$, $\Psi = (dy/dx)_{s=0}$ is the azimuthal angle of the track direction at the starting point, see Fig.4.2. We define bend plane relative to the $\vec{B}$ field which is

along the beam axis while the transverse plane perpendicular to the beam axis.

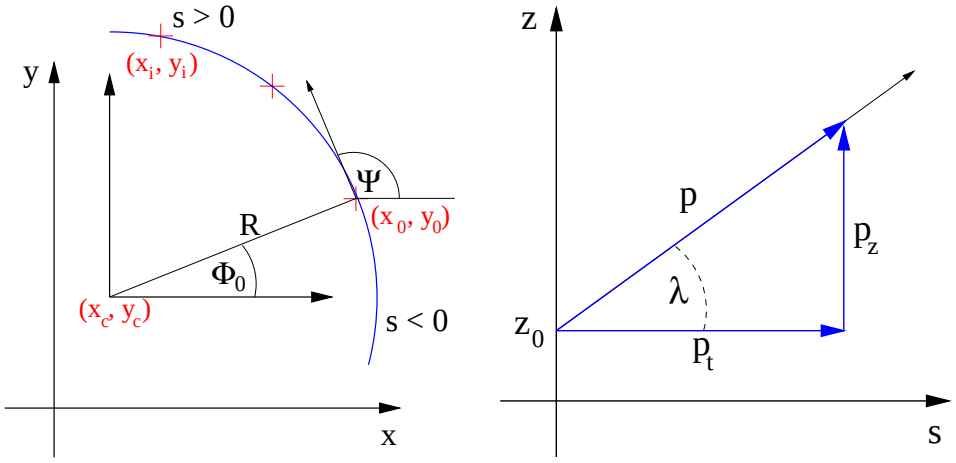

Figure 4.2: Projection of a helix onto the transverse plane (a) and onto the bend plane (b)

The helix parameters are given by two simultaneous 2D fits, in the bend plane and the transverse plane respectively. The circular fit in the xy-plane gives the center of the fitted circle (x_0, y_0) and the curvature $\kappa = 1/R$ while the linear fit in bend plane gives z_0 and λ. The curvature of the track is related to the transverse momentum by

$$p_t = cqB/\kappa, \tag{4.2}$$

with the following units: κ in [m^{-1}], B in [Tesla], c the speed of light in [m/ns] and p_t in [GeV/c]. Longitudinal momentum can be evaluated as:

$$p_z = p_t \tan\lambda. \tag{4.3}$$

Transverse momentum resolution is estimated with embedding simulation. Fig.4.3 shows the p_t resolution for pions and kaons in STAR[60]. At low momentum, momentum resolution is dominated by multiple Coulomb scattering while, at high momentum, it is limited by the strength of the magnetic field and the TPC spacial resolution. The best relative momentum resolution falls between these two and it is 1.9% for pions.

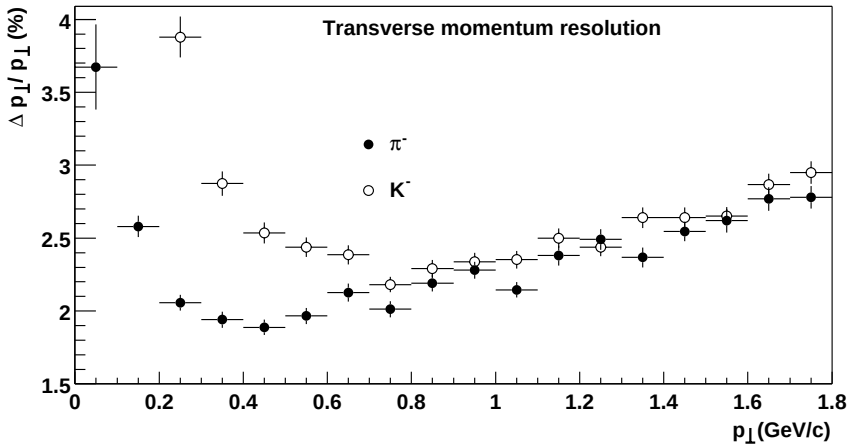

Figure 4.3: Transverse momentum resolution of the STAR TPC for pions and kaons in a 0.25T magnetic field, figure from[60]

4.1.2 Primary Vertex Reconstruction

With all of the tracks reconstructed in the TPC, the primary vertex is found by extrapolating tracks back to the origin. The global average is the vertex position. First, the helices are projected to a reference point which is close to an estimated vertex. The natural choice of the reference point would be the center of the beam profile which in 3D is the central axis of the beam diamond. Then, a χ^2 minimization of the perpendicular distances from the track vectors to a point, distance of closest approach (DCA), is used to decide the primary vertex position. Nearby the central axis, instead of helix, straight line approximation is used for an analytical solution, see Fig.4.4. Tracks at large distances from the central cluster (outliers) have a strong influence on the results. A simple "truncation" method is used in an iterative way to remove the outliers and improve the "robustness" of the fit. We first use all reconstructed tracks to get an estimate of the vertex parameters. Then we use that as a seed to the next iteration and we remove from the track pool all tracks with distances greater than a certain cut value. The new vertex, is then used as a seed to the next iteration. The whole process converges after 3-4 iterations.

The primary vertex resolution decreases as the square root of the number of tracks used in the calculation. A resolution of 350 μm is achieved when the number

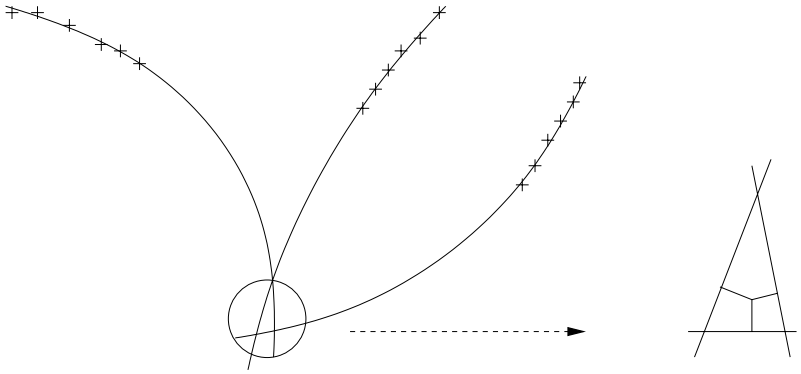

Figure 4.4: Concept of minimization of distances of closest approach.

of tracks is above 1000, see Fig.4.5[60]. It is calculated by comparing the position of the vertices that are reconstructed using each side of the TPC, separately.

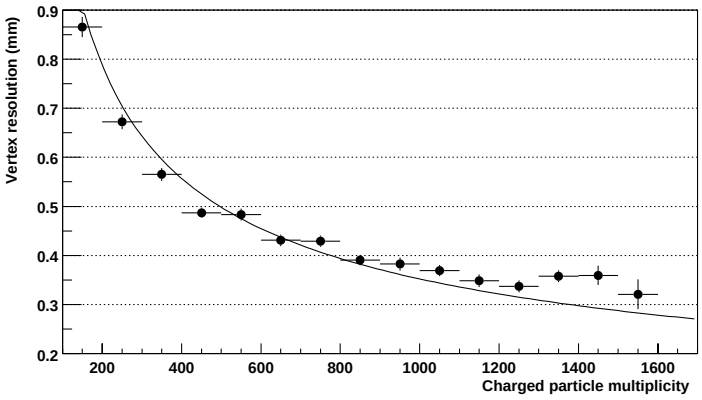

Figure 4.5: Primary vertex resolution in the transverse plane, figure from[60]

Primary vertex determines the interaction point. Global tracks with distance of closest approach to primary vertex less than 3 cm will be refitted including the vertex as an additional space point, which gives different parameters associated with primary tracks. The accurate determination of the main vertex thus is essential for the ability to discriminate between primary and secondary tracks, which in turn decide the reconstruction of secondary vertices. Weak decay strange particles K^0_S and $\Lambda(\bar{\Lambda})$ used in this analysis are identified this way.

4.1.3 Particle Identification with dE/dx

The calculable charge particle energy loss through the TPC gas is a valuable tool for particle identification. It works especially well for low momentum particles but as the particle energy rises, the energy loss becomes less mass-dependent and it is hard to separate particles. By truncating the largest 30% of the dE/dx samples on a track, the mean value of the remaining 70% of the dE/dx sample were calculated. In the STAR TPC, the maximum possible number of dE/dx is the TPC pad rows' number, 45. The measured mean $\langle \mathrm{d}E/\mathrm{d}x \rangle$ can be described by the Bethe-Block function and the resolution σ. We can select a certain kind of particles by applying that particle's mass in Bethe-Bloch formula and cut on number of σ. Fig.4.6 shows the energy loss for particles in the TPC as a function of the particle momentum.

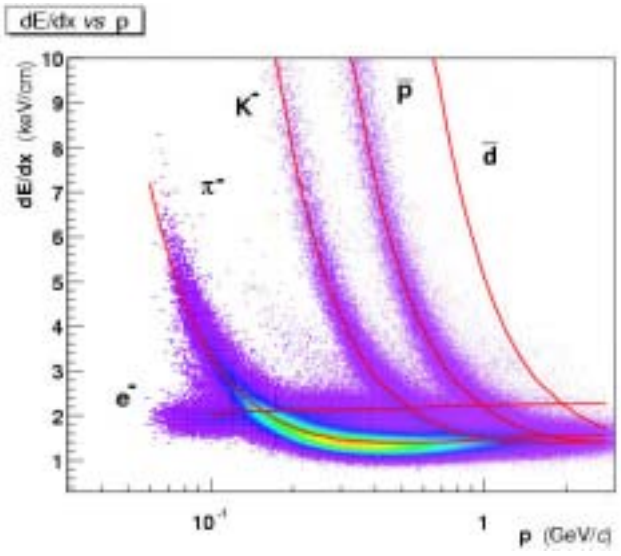

Figure 4.6: Particle energy loss versus momentum

4.2 Secondary Vertex Reconstruction

The neutral strange particles with two-body charged weak decays, K^0_S mesons and Λ and $\bar{\Lambda}$ hyperons, are detected through their typical decay topology. The properties of these decays are summarized in Table4.1. The mean lifetime of these particles

implies that their decay vertex will, in most cases, be well separated from the primary vertex. In Collider experiments the separations between secondary vertex and the primary vertex are on the order of a few centimeters because of the lower momenta in a collider environment while it range from a few tens of centimeters up to a few meters in fixed-target experiments. A well-separated secondary vertex and two tracks of opposite charge ("V" topology with "0" net charge) is the signature for neutral strange decay, cf. Fig.4.7.

Particle	Decay	Fraction(%)	$c\tau$(cm)	Mass(GeV/c^2)
K^0_S	$\pi^+\pi^-$	68.6	2.68	0.496
$\Lambda(\bar{\Lambda})$	$\mathrm{p}\pi^-(\bar{\mathrm{p}}\pi^+)$	63.9	7.89	1.115

Table 4.1: Decay parameters of V0 particles

The majority of V0s decay before they reach the TPC Inner Field Cage and the neutral V0s can not ionize the TPC gas. They are reconstructed in STAR with the standard V0 analysis method, i.e. looking for charge decays of K^0_S and $\Lambda(\bar{\Lambda})$ particles. Fig.4.7 shows a schematic representation of a V0 decay: a neutral particle emitted from the primary vertex V travels a distance r_V (decay length) and decays into two charge daughter particles which are consequently detected in the TPC.

The main steps of V0 reconstruction can be described as below, considering all tracks in each event that do not originated from the primary vertex.

- For any pair of tracks of opposite charges in an event checks for a common vertex. This is done by checking the distance between them at the point of the closest approach. If a 3D distance between the tracks at that point is greater than a certain value, the pair is consided as not originated from a common point and rejected.

- The next check is the distance between the secondary vertex and the primary vertex (the main vertex position assumed to be known with infinite accuracy). The decay vertex has to be beyond a certain distance. This avoids the very

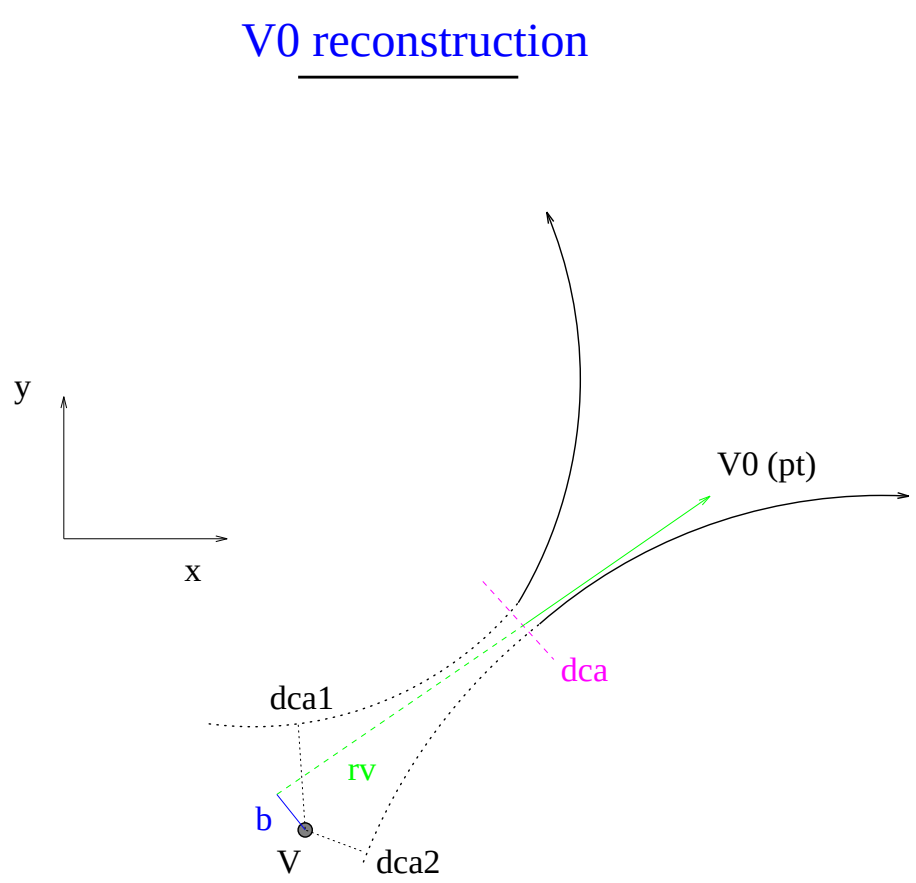

Figure 4.7: V0 decay topology and some important associated parameters, figure from[95].

large number of random crossings close to the primary vertex.

- Then an invariant mass analysis is performed which gives the mass and the three momentum components of the parent particle.

- Finally we require the parent particle to be emanated from the primary vertex. It's impact parameter has to be less than a cut value.

However, due to

- The high multiplicities at RHIC, up to 2000 in a central Au+Au event around mid-rapidity

- Most of the V0 vertices are close to the primary vertex

- Finite position and momentum resolution
- Multiple Coulomb Scattering (MCS)

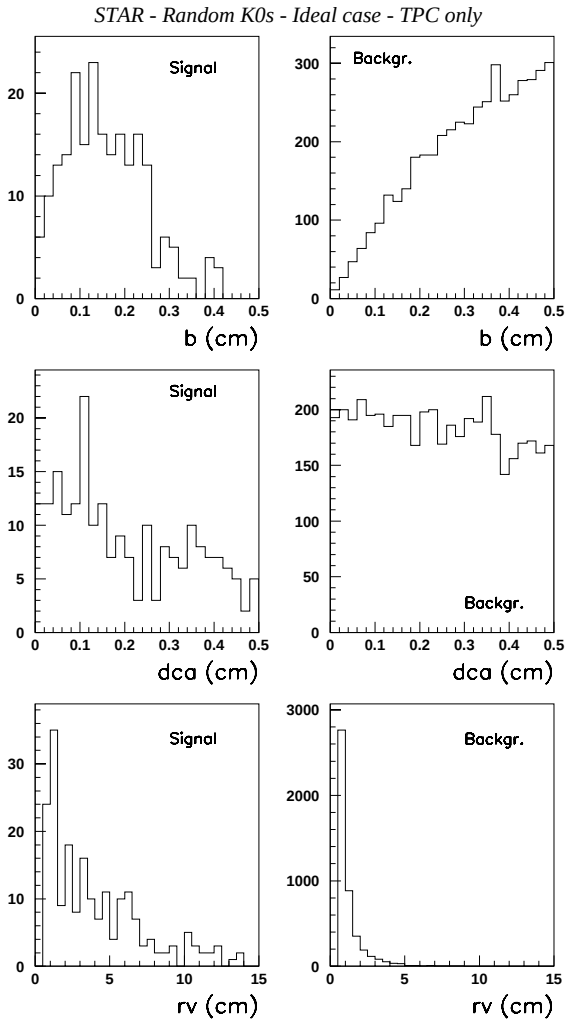

Figure 4.8: Characteristic cut distributions for either real(left) or fake(right) V0 decays, figure from[95].

many fake secondary vertices are formed, which is known as combinatorial background. We can minimize the background by putting cuts on various quantities. The distribution of three most common cut variables from FRITIOF MC simulations are shown in Fig.4.8. These cuts are, the impact parameter (b) of the reconstructed V0 from the event vertex (upper), the distance of closest approach (dca) of the two

daughter tracks (middle), and the decay distance of the V0 from the primary vertex r_V (lower). The left column shows the distributions for real V0 particles (K^0_S here), whereas the right column shows the combinatorial background.

The V0 information will be used further to reconstruct multiple strange particles Ξ (strangeness 2) and Ω (strangeness 3) which decay into Λs and pions or kaons.

4.3 Event Selection

During the summer 2000 run, real data was taken with two different trigger conditions:

- minimum-bias trigger requiring a coincidence between the ZDC's
- central trigger requiring ZDC coincidence and a high multiplicity in the CTB

The central trigger corresponds to approximately the top 15% of the measured cross section for Au+Au collisions. The results presented here are from about 200,000 minimum-bias trigger events and 180,000 central trigger events.

During the summer 2000 run, the collision vertex position varied considerably. Since the collision vertex position has a great effect on the particles acceptance in transverse momentum (p_t) and pseudo-rapidity (η) phase space due to pure geometric effects or the material distributions in the TPC, only events with primary vertex position within 75 cm longitudinally of the TPC center and within 1cm radially of the beam line are used in the analysis. The total charged track multiplicity distribution with pseudo-rapidity window $|\eta| \leq 0.75$ is used for the centrality measurement, see Fig.4.9. The eight centrality bins and the corresponding cross sections are listed in Table4.2. The integral under the curve is 1.0 and the cumulative fraction corresponding to the lower edge of each centrality is indicated in percentage. The three centrality bins used in this analysis are 85-45%, 45-11% and the top 11% which are respectively a combination of bin 1-2 in low multiplicity centrality, bins 3-6 for the mid-central bins and bins 7-8 for the most central bins, cf. Table4.2.

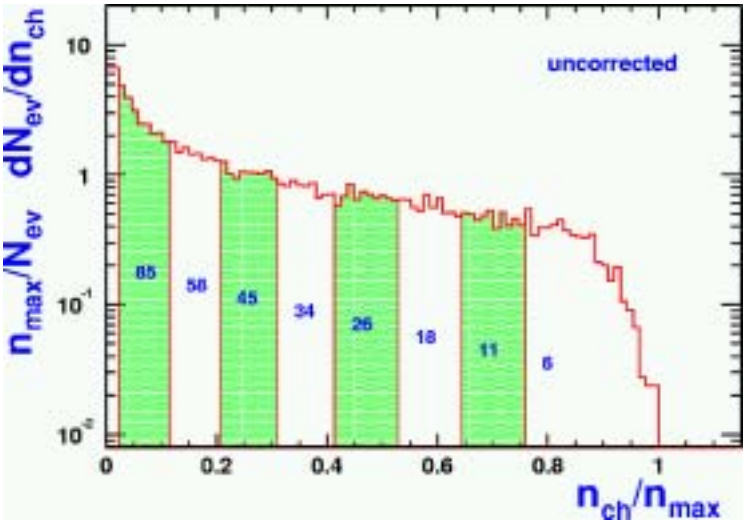

Figure 4.9: The primary track multiplicity distribution as a function of the number of tracks normalized by the maximum observed number of tracks, figure from[23].

Centrality Bin	Multiplicity	Measured Cross Section	Geometric Cross Section
1	20-100	58-85%	53-77%
2	100-180	45-58%	41-53%
3	180-270	34-45%	31-41%
4	270-360	26-34%	24-31%
5	360-460	18-26%	16-24%
6	460-560	11-18%	10-16%
7	560-660	6-11 %	5-10 %
8	> 660	Top 6 %	Top 5 %

Table 4.2: Centrality bins in Fig.4.9 from reference[23] and corresponding measured cross section as well as associated geometric cross section for Au+Au collisions

4.4 Anisotropic Flow Analysis Relative to the Reaction Plane

Some important development has been made in recent years in the approach suitable for flow studies at high (AGS/SPS/RHIC) energies [4] where the longitudinal flow is well decoupled from transverse flow. This means that at high energies we do not have to rotate to the flow axis to study the flow pattern[89], instead use the plane transverse to the beam axis. Thus we discuss anisotropic transverse flow from the particle azimuthal distributions at fixed rapidity or pseudorapidity. The

azimuthal distribution is generally described by means of a Fourier expansion[15], and the different kinds of anisotropies are characterized as corresponding to different harmonics.

The essence of the method can be summarized as:

- First estimate the reaction plane, i.e. event plane.
- Then evaluate the Fourier coefficients in the expansion of the azimuthal distribution of particles with respect to event plane.
- Correction for finite number of detected particles and detector acceptance if it does not have full azimuthal coverage.

4.4.1 Fourier Expansion

The most often used triple differential particle distribution can be written in terms of Fourier series of particle emission azimuthal angle measured with respect to the reaction plan

$$E\frac{d^3N}{d^3p} = \frac{1}{2\pi}\frac{d^2N}{p_t dp_t dy}\left(1 + \sum_{n=1}^{\infty} 2v_n \cos[n(\phi - \Psi_R)]\right), \tag{4.4}$$

where Ψ_R is the true reaction plane angle, i.e. the angle between the x-axis and the reaction plane. We define the longitudinal or beam direction as the z-axis, and the transverse plane as x-y plane. The sine terms in the expansion vanish due to the reflection symmetry with respect to the reaction plane. In a given rapidity (y) and p_t interval the coefficients are determined by

$$v_n = \langle \cos[n(\phi - \Psi_R)] \rangle. \tag{4.5}$$

Similarly this Fourier expansion can be done in coordinate space, where for a given rapidity and p_t interval the coefficients are determined by

$$r_n = \langle \cos[n(\arctan((y/x) - \Psi_R)] \rangle, \tag{4.6}$$

where x, y are the particle space coordinates at freeze-out.

4.4.2 Estimation of the Reaction Plane

The reaction plane can be reconstructed only if the final state of the interaction products retains some memory (azimuthal asymmetry) of the initial collision geometry. The method uses the anisotropic flow itself, i.e. different order azimuthal event shapes, to determine the reaction plane. That means the reaction plane can be determined independently for each harmonic of the anisotropic flow. The reaction plane vector Q_n and the reaction plane angle Ψ_n from the nth harmonic of the distribution are defined by

$$\begin{aligned} Q_n \cos(n\Psi_n) &= X_n = \sum_i w_i \cos(n\phi_i), \\ Q_n \sin(n\Psi_n) &= Y_n = \sum_i w_i \sin(n\phi_i), \end{aligned} \tag{4.7}$$

and

$$\Psi_n = \left(\tan^{-1} \frac{\sum_i w_i \sin(n\phi_i)}{\sum_i w_i \cos(n\phi_i)} \right) \Big/ n, \tag{4.8}$$

where n=1, 2, 3, ... For odd values of n, the weighting factor w_i has a different sign in the forward and backward hemispheres to account for momentum conservation. The reaction plane angle Ψ_n determined from the nth harmonic is in the range $0 \leq \Psi_n < 2\pi/n$. For a given n the corresponding Fourier coefficient v_n can be evaluated using the reaction planes determined from any harmonic m, with $m \leq n$, if n is a multiple of m. That is, the first harmonic plane can be used, in principle, to evaluate all v_n. However, in general, it is true that better accuracy for the determination of v_n is achieved by using the event plane (Ψ_n) determined from the same harmonic because the resolution deteriorates as $k = n/m$ increases. The quantity $\phi - \Psi_m$ has a lowest order periodicity of $2\pi/m$.

4.4.3 Reaction Plane Resolution

The magnitude of the anisotropy and the finite number of particles available to determine the reaction plane leads to a finite resolution. Therefore, the measured v_n^{obs} coefficients with respect to the reaction plane have to be corrected for the

reaction plane resolution

$$v_n = \frac{v_n^{obs}}{\langle \cos[n(\Psi_n - \Psi_R)] \rangle}. \tag{4.9}$$

The mean cosine values are less than unity thus this correction always increases the flow coefficients. However, the true reaction plane angle, Ψ_R, is unknown experimentally. Following Ref.[4], if one constructs the reaction plane from two random subevents, the corresponding correlation function can be written as

$$\langle \cos[n(\Psi_n^a - \Psi_n^b)] \rangle = \langle \cos[n(\Psi_n^a - \Psi_R)] \rangle \times \langle \cos[n(\Psi_n^b - \Psi_R)] \rangle, \tag{4.10}$$

where ${\Psi_n}^a$, ${\Psi_n}^b$ are the angles of the event planes determined in the subevents. The assumption made here is that there are no other correlations except the ones due to flow, or that such other correlations can be neglected. This relation permits the evaluation of the event plane resolution directly from the data. For two subevents with equal multiplicity the resolution of each of them is

$$\langle \cos[n(\Psi_n^a - \Psi_R)] \rangle = \sqrt{\langle \cos[n(\Psi_n^a - \Psi_n^b)] \rangle}. \tag{4.11}$$

The full event plane resolution can be calculated from the sub-event resolution, taking into account that the multiplicity of the full event is twice as large as that of the sub-event

$$\langle \cos[n(\Psi_n - \Psi_R)] \rangle = \sqrt{2} \langle \cos[n(\Psi_n^a - \Psi_R)] \rangle. \tag{4.12}$$

Generally, we have

$$\langle \cos[n(\Psi_n - \Psi_R)] \rangle = C \times \sqrt{\langle \cos[n(\Psi_n^a - \Psi_n^b)] \rangle}, \tag{4.13}$$

where C is a correction[86] for the difference in subevent multiplicity compared to the full event.

Biases due to the finite acceptance of the detector which cause the particles to be azimuthally anisotropic in the laboratory system can be removed by making the distribution of event plane isotropic in the laboratory. This is not needed in STAR because of its full azimuthal coverage.

Chapter 5

Results

5.1 Reaction Plane Evaluation

5.1.1 Reaction Plane Distribution

Primary tracks passing the selection criteria listed in Table5.1 were used for reaction plane reconstruction. Tracks were required to have at least 15 space points to ensure

Track Selection Criteria	
Number of hits on track	> 15
DCA to primary vertex	< 1cm
Proton-like track DCA to primary vertex	< 0.5cm (for $\Lambda + \bar{\Lambda}$ v_2)
Transverse momentum	$0.1 < p_t \leq 2.0$ GeV/c
Pseudorapidity	$\|\eta\| < 1.0$

Table 5.1: Track quality and kinematic cuts for reaction plane reconstruction

the quality of tracks and get rid of short tracks which are mostly coming from "ghost" tracks in tracking. In order to have a constant tracking efficiency within $\pm 10\%$ tracks were selected with 0.1 GeV/c $< p_t \leq$ 2.0 GeV/c. Also, the ratio of the number of space points to the expected maximum number of space points for that particular track was required to be greater than 0.52, which will largely suppress split tracks from double counting. These cuts are used for getting better reconstructed reaction

plane. However, the analysis results are not sensitive to these cuts.

The reaction plane angle are calculated with the subevent method. In our analysis, the two subevents are obtained by dividing all particles of an event randomly into two subevents. Reaction plane vector is calculated from each subevent, (Q_{1x}, Q_{1y}) and (Q_{2x}, Q_{2y}). Average the results from two subevents we get the reaction plane vector for the full event:

$$Q_x = \frac{1}{2}(Q_{1x} + Q_{2x}) \quad , \quad Q_y = \frac{1}{2}(Q_{1y} + Q_{2y})$$

and the reaction plane angle:

$$\Psi_R = \left(\tan^{-1}\frac{Q_y}{Q_x}\right) \Big/ 2.$$

If a particle is used for both reaction plane evaluation and v_2 calculation, strong correlation will be introduced by using the same particle. This is generally called "auto-correlation". To avoid this effect, correlation of each particle with the event plane of the other particles should be considered. Since only primary track with DCA less than 1cm are used for reaction plane reconstruction and neutral strange particle are reconstructed from decay particles, or secondary particles, most of which has relatively large DCA to primary vertex, this will help us solve the "auto-correlation" problem in an "simple" way. For K^0_S reconstruction we ask for decay tracks having DCA to primary vertex larger than 1.5 cm. Thus, there is no overlap between particles used for reaction plane reconstruction and particles used for V0 vertex reconstruction. Since one of the $\Lambda(\bar{\Lambda})$ decay particle, proton(anti-proton), is much heavier than the other one, π^- or π^+, it usually take most of the mother-particle's momentum, which make it in many cases more like a primary track instead of a secondary track. In this analysis we have proton(anti-proton) DCA to primary vertex cut at 0.7 cm which is less than 1cm. To remove "auto-correlation", a 0.5 DCA to primary vertex cut on proton-like track are added when we evaluate reaction plane for $\Lambda(\bar{\Lambda})$ v_2. A track is considered proton-like if its energy loss (dE/dx) is within three standard deviations of that expected for protons. The uncorrected reaction plane angle distributions for K^0_S and $\Lambda(\bar{\Lambda})$ are shown in Fig.5.1.

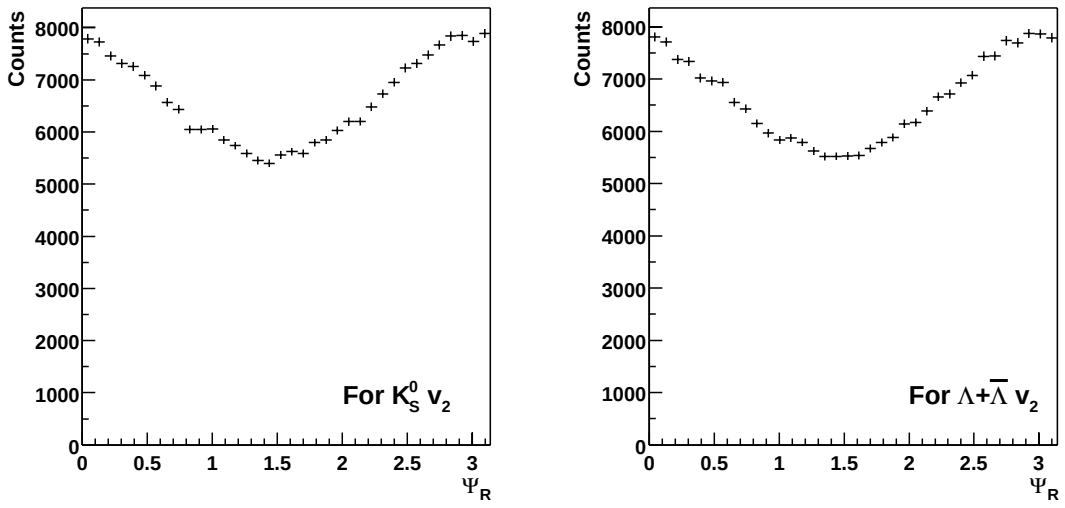

Figure 5.1: Reaction plane angle distribution before correction for K^0_S (left) and $\Lambda(\bar{\Lambda})$ (right) v_2 calculation

5.1.2 Flattening of Reaction Plane Distribution

The good azimuthal symmetry and large phase space coverage of STAR TPC is a great advantage for flow analysis. Since the orientation of the impact parameter vector is random, the distribution of the determined reaction plane should be uniform (flat). The non-flat event plane angle distributions in Fig.5.1 are the direct result of deficiencies in the acceptance of TPC (bad read-out board during the run). Multiplicity dependent corrections are applied by generating a weighting file in every centrality bin, cf. Table4.2, according to particle azimuthal distribution. This weight file is then used in reaction plane angle determination, cf. Eqn.4.7, which goes into the ω_i term. After correction the event plane angle distribution becomes flat, see Fig.5.2. Such corrections ensure the absence of spurious flow signals which could result from distortions in the reaction plane distributions.

5.1.3 Reaction Plane Resolution

The measured full reaction plane angle resolution was estimated from the two subevent reaction plane angles. The reaction plane resolutions in 8 flow centrality

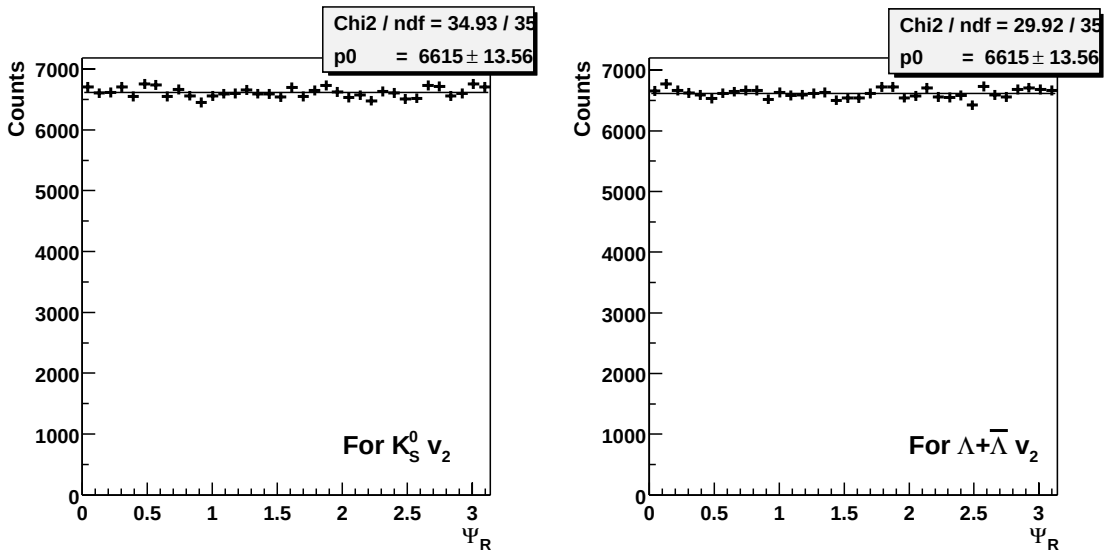

Figure 5.2: Reaction plane angle distribution after acceptance correction for K^0_S(left) v_2 and $\Lambda(\bar{\Lambda})$(right) v_2

bins are shown in Fig.5.3. A maximum resolution of 0.683±0.005 and 0.652±0.006 is reached for the K^0_S and $\Lambda+\bar{\Lambda}$ analysis respectively in mid-central events. This value is much higher than that get at SPS energy (NA49 only reached 0.4[40]) and closer to the ideal value of 1.0. The reaction plane resolution is lower for most peripheral and most central events because of low multiplicity and less event anisotropy respectively. The event plane resolution for $\Lambda+\bar{\Lambda}$ v_2 is a little less than that for K^0_S due to the additional proton-like track DCA cut. The reaction plane resolution from minimum bias events is 0.528 ± 0.002 for K^0_S v_2 calculation and 0.494 ± 0.003 for $\Lambda(\bar{\Lambda})$ v_2.

5.2 K^0_S and $\Lambda(\bar{\Lambda})$ Reconstruction

5.2.1 K^0_S and $\Lambda(\bar{\Lambda})$ Invariant Mass Distribution

The cuts used for K^0_S and $\Lambda(\bar{\Lambda})$ reconstruction are listed in Table5.2. A 3σ dE/dx cut is used for select proton (anti-proton) for $\Lambda(\bar{\Lambda})$ reconstruction. Since all the events were dominated by pions, this cut greatly reduces the combinatorial background,

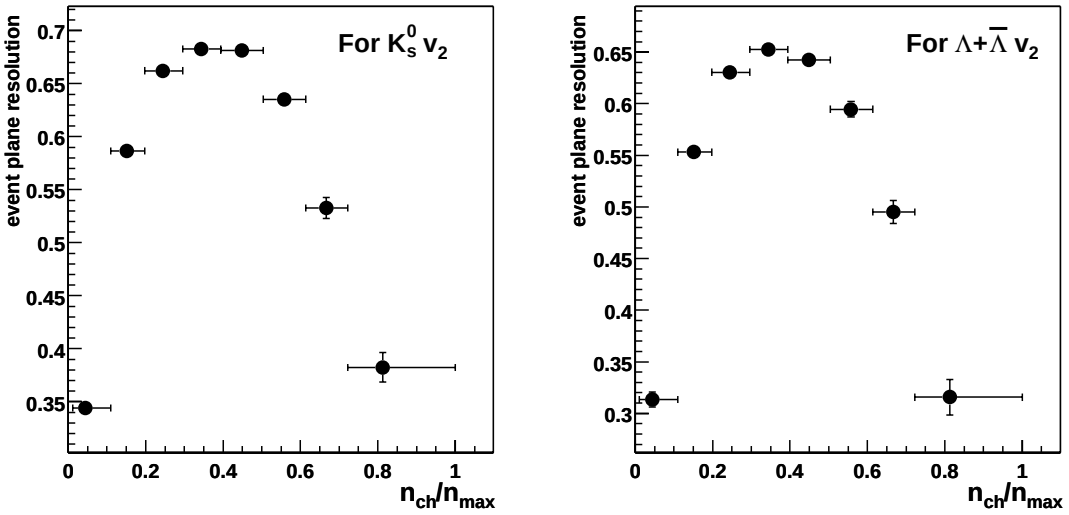

Figure 5.3: Reaction plane resolution for K^0_S (left) v_2 and $\Lambda + \bar{\Lambda}$ (right) v_2

while a cut on pion dE/dx do not show much effect. Decay daughter track DCA to primary vertex cuts were applied to exclude primary tracks. DCA between the two daughter tracks are used to eliminate track pairs that are not come from the same common decay vertex. Reconstructed mother particle DCA to primary vertex cut is used because the neutral strange particle are from the primary vertex. All these cuts together reduce the combinatorial background greatly.

For track pairs passed all the cuts listed in Table5.2, the invariant mass for the

Track Selection Criteria	K^0_S	$\Lambda\Lambda$
Number of hits on track	> 15	> 15
Track (p, $\bar{p}$) DCA to primary vertex	N/A	> 0.9 cm
Track (π^-,π^+) DCA to primary vertex	> 1.5 cm	> 2.5 cm
Positive and negative track DCA	< 0.75 cm	< 0.75 cm
Track (K^0_S or $\Lambda(\bar{\Lambda})$) DCA to primary vertex	< 0.7 cm	< 0.7 cm
Decay Length	> 5 cm	> 5 cm
Pion PID	N/A	N/A
Proton PID	N/A	$< \|3\sigma\|$

Table 5.2: Track quality and kinematic cuts for K^0_S and $\Lambda(\bar{\Lambda})$ reconstruction

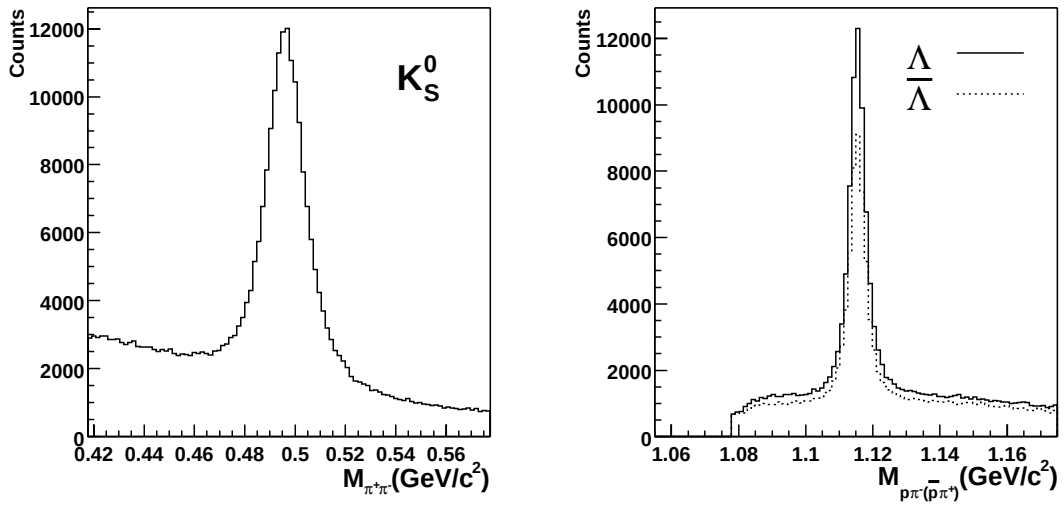

Figure 5.4: Invariant mass distributions for $\pi^+\pi^-$ showing a K^0_S mass peak (left panel) and $p\pi^-(\bar{p}\pi^+)$ showing a $\Lambda(\bar{\Lambda})$ mass peak (right panel)

decay vertex is calculated by

$$m = \sqrt{(\sqrt{{m_p}^2 + {P_p}^2} + \sqrt{{m_n}^2 + {P_n}^2})^2 - P^2}, \tag{5.1}$$

where subscript p and n represent positive and negative decay particle respectively. For K^0_S reconstruction pion mass are used for both m_p and m_n. For $\Lambda(\bar{\Lambda})$ one of them is substituted with proton (anti-proton) mass. P_p and P_n are positive and negative track momentum at the DCA points and $P = P_p + P_n$ is the total momentum. With all the topological cuts used, clear signal is observed in invariant mass distributions. Fig.5.4 shows the invariant mass distribution for reconstructed K^0_S (left) and $\Lambda(\bar{\Lambda})$ (right) with the cuts listed in Table5.2 from minimum bias collisions.

A Gaussian fit to the invariant mass peak gives:

$$\text{Mass}_{K^0_S} = 496 \pm 4 \text{ Mev}/c^2$$

$$\text{Width}_{K^0_S} = 15 \pm 1 \text{ Mev}/c^2$$

and

$$\text{Mass}_{\Lambda} = 1116 \pm 7 \text{ Mev}/c^2$$

$$\text{Width}_{\Lambda} = 5 \pm 1 \text{ Mev}/c^2$$

They are consistent with values listed in the PDG[25] and the widths are determined by the particle momentum resolution of the detector. The cuts used in this analysis are chosen to maximum the signal to background ratio in the mean time without losing much statistics. The typical signal to background ratio in our analysis is about 4:1 for K^0_S and 5:1 for $\Lambda(\bar{\Lambda})$.

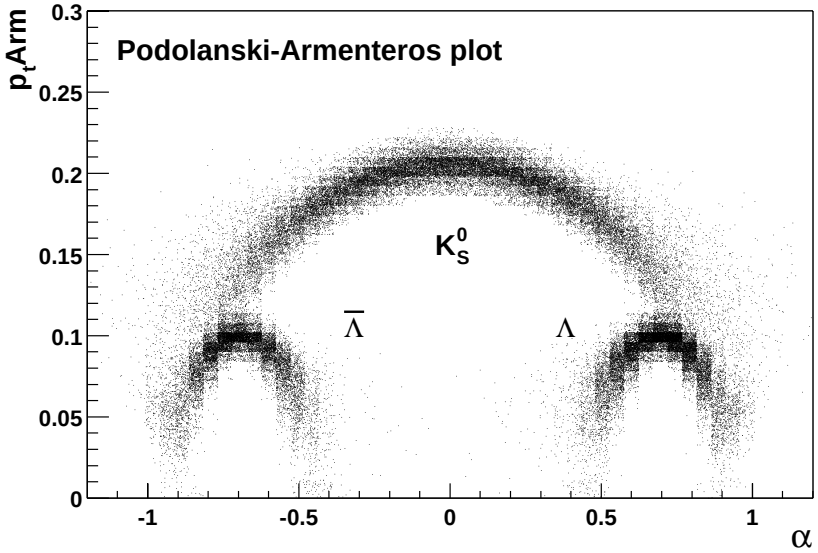

Figure 5.5: Podolanski-Armenteros plot for V0s

Fig.5.5 is the Podolanski-Armenteros plot[85], which is traditionally used to show the three possible weak V0 decays. Only V0 vertex candidates that fall into the mass window equal to two times Gaussian fit width around the mass peak are used for this plot. This plot decompose the momentum of each decay track into two components: perpendicular to the total momentum (p_tArm) and parallel to the total momentum (p_l). For each decay, we plot the value of p_tArm (which is by definition the same for both tracks) versus the variable $\alpha = (p_l^+ - p_l^-)/(p_l^+ + p_l^-)$, constructed from parallel momenta of the positive and negative tracks. Clear K^0_S and $\Lambda, \bar{\Lambda}$ bands can be seen on the plot. The maximum value of p_tArm occurs when the decay products are perpendicular to the direction of the parent in the rest frame which means that for K^0_S, with identical mass daughters, α is equal to zero.

5.2.2 Background Subtraction

The combinatorial background has to be subtracted before calculating v_2. We can fit the invariant mass distribution with either a combination of a Lorentzian (Breit-Wigner) function for the signal and a 2nd order polynomial function for the background, or a combination of a Gaussian function for the signal and a 2nd order polynomial function for the background. Comparing the two fits, Lorentzian fit, see Fig.5.6, tends to overshot the mass peak while the Gaussian fit, see Fig.5.7, always under-estimate the raw yield[71].

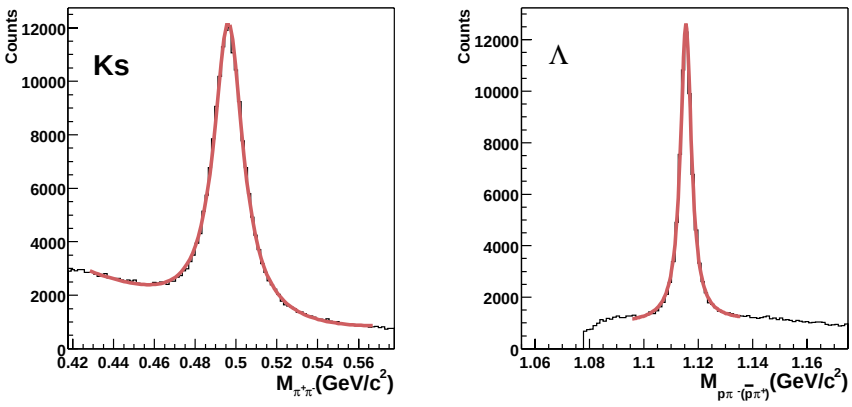

Figure 5.6: K^0_S (left) and Λ (right) invariant mass fit with Lorentzian function.

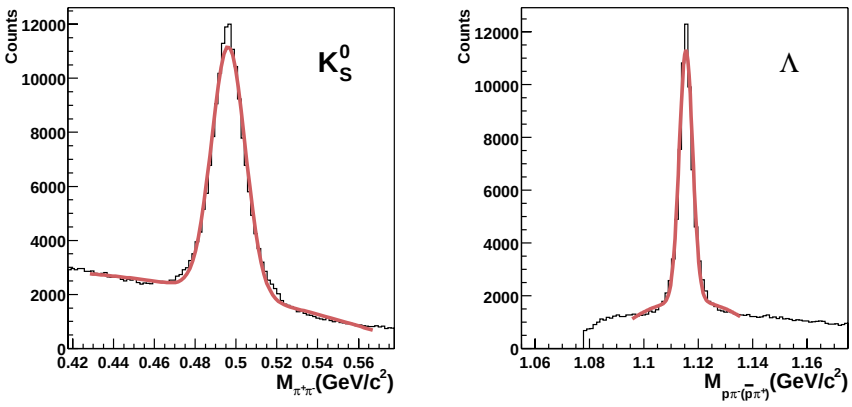

Figure 5.7: K^0_S (left) and Λ (right) invariant mass fit with Gaussian function.

For v_2 analysis we need to subtract background in individual ϕ and p_t bins. In higher p_t region, much less statistics can be got in a particular bin, which makes it even harder to have a good fit of the signal peak. It turns out that the track rotation together with bin counting method is more suitable for this analysis to get K^0_S and $\Lambda(\bar{\Lambda})$ raw yields. The basic idea of this method is similar to the mixing event method[65] and first used by Hui Long[71] in $\Lambda(\bar{\Lambda})$ analysis in STAR. Instead of taking a track from another event, one of the two decay tracks is rotated by 180 degree in the azimuthal plane with respect to the primary vertex. In this way, all the decay vertices were destroyed because one of the daughter tracks is rotated away without changing the symmetry of the whole event statistically. After track rotation, secondary vertex is reconstructed again in exactly the same way, but this time only combinatorial background is reconstructed, see Fig.5.8. With this method most of

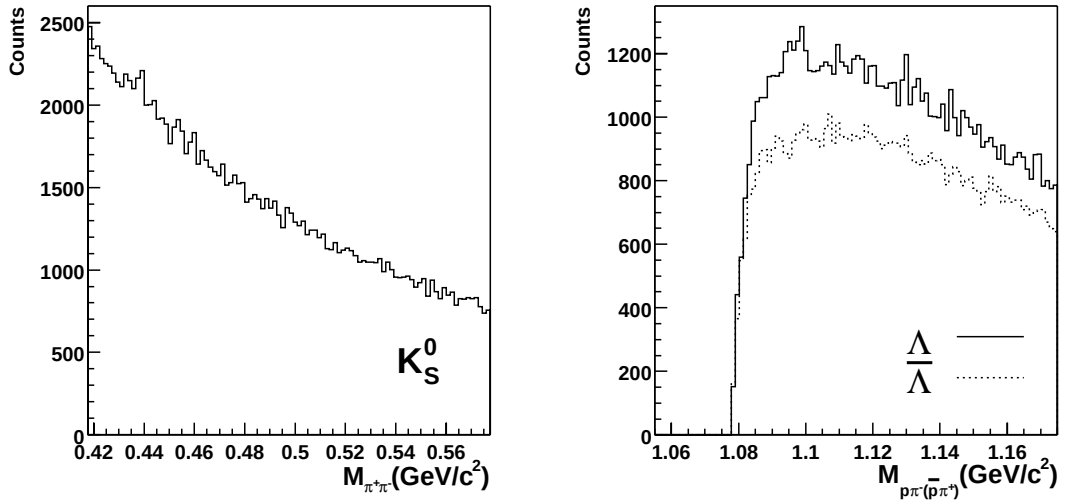

Figure 5.8: Invariant mass distributions for $\pi^+\pi^-$ (left panel) and $p\pi^-(\bar{p}\pi^+)$ (right panel) after rotating one of the daughter tracks

the combinatorial background can be subtracted. The invariant mass distribution after background subtraction from minimum bias events for K^0_S and Λ are shown in Fig.5.9.

The raw yield is estimated by bin counting method. This method obtain the yield by simply summing the number of counts in the peak. Since some background

underneath the peak remains, by simply summing the entries in the histogram between the limits, the background is also being counted in the yield. The two limits used in the bin counting method are 2 times Gaussian fit width around the mass peak value for both K^0_S and $\Lambda(\bar{\Lambda})$. For K^0_S, a first order polynomial function is used to fit the background and the fitted background within the same limits are subtracted to get the raw yield, see Fig.5.9 (left). For Λ and $\bar{\Lambda}$ almost no background is left after the track-rotation background subtraction. We suppose the background is linear in shape and background shape do not change under the mass peak. Thus, we can simply subtract the background values from either side of the peak, in such a way that the total range of the background subtraction is equal to the range under the peak, see Fig.5.9 (right). The bin counting method is reliable in the limit of low statistics, where a fit may fail. The differences that occur when using different cuts in V0 vertex reconstruction and different yield subtraction methods is used later to estimate the systematic error. The typical raw yield per event for this analysis is about 0.7 for K^0_S and 0.3 for Λ for minimum bias events.

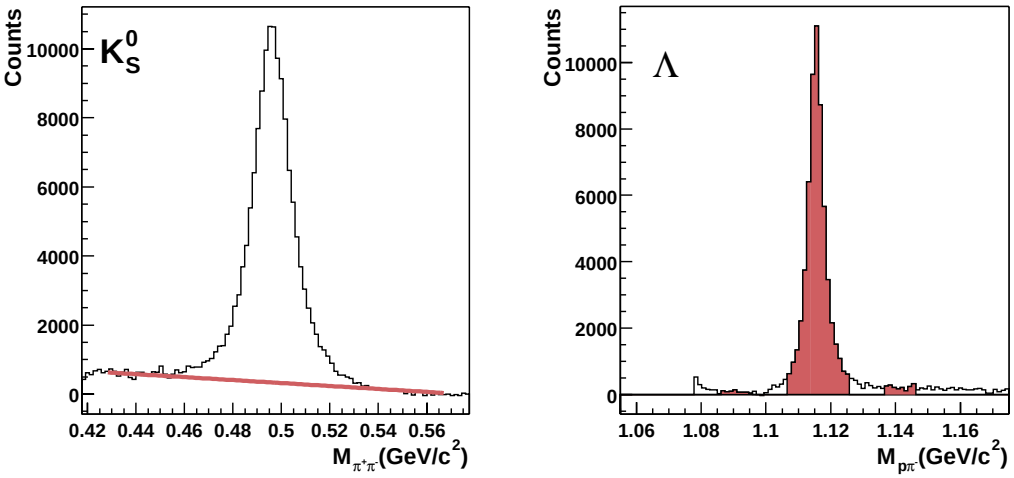

Figure 5.9: K^0_S and Λ invariant mass distribution after track-rotation background subtraction. Raw yields are got by add the histogram bin content and subtract the fitted background for K^0_S or subtract background from either side of the peak for $\Lambda(\bar{\Lambda})$.

After background subtraction and extracting the raw yield, K^0_S and $\Lambda(\bar{\Lambda})$ phase space coverage of raw data can be calculated. The y-p_t coverage for the K^0_S and Λ

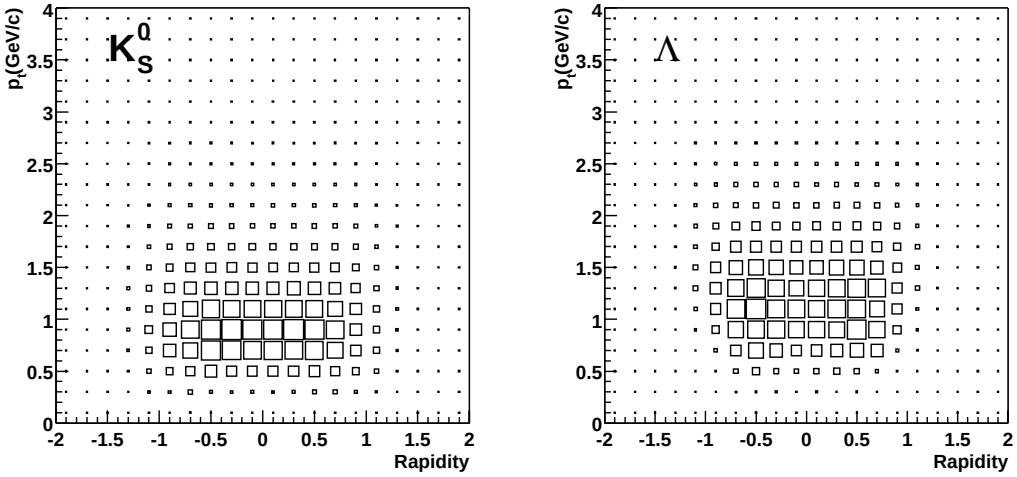

Figure 5.10: Phase space coverage for K^0_S (left) and Λ (right) in p_t and rapidity, the box size is proportional to the contents.

from minimum bias collisions are shown in Fig.5.10 . The $\bar{\Lambda}$ has the same phase space coverage as Λ. The cut-off at low p_t is due to the detector acceptance effect for low p_t pions and protons. The reconstructed neutral strange particles are concentrated between $|y| < 1$ and $p_t < 2$ GeV/c. For our analysis a rapidity cut $-1 < y < 1$ is added to keep a roughly constant acceptance in rapidity. The particle identified and used for the v_2 analysis are from the kinematic region 0.2 GeV/$c \leq p_t \leq$ 3.2 GeV/c for K^0_S or 0.3 GeV/$c \leq p_t \leq$ 3.2 GeV/c for $\Lambda + \bar{\Lambda}$.

5.3 Elliptic Flow of K^0_S and $\Lambda + \bar{\Lambda}$

With the determined azimuthal angle of the reaction plane (Ψ_R) event by event and the reconstructed neutral strange particles, azimuthal angle distributions of K^0_S and $\Lambda(\bar{\Lambda})$ with respect to reaction plane, $\phi - \Psi_R$, can be reconstructed, which is done in several steps. Here, ϕ is azimuthal angle of the reconstructed neutral strange particle. Since no significant differences in elliptic flow are observed between Λ and $\bar{\Lambda}$, to compensate for limited statistics, Λ and $\bar{\Lambda}$ are summed together in the analysis.

- First, the invariant-mass distribution calculated from the raw data for every

studied trigger and reaction centrality window were divided into transverse momenta p_t and azimuthal angle $\phi - \Psi_R$ bins, with p_t bin width of 400 MeV/c and $\phi - \Psi_R$ bin width 10 degree.

- Then, the combinatorial background was generated and divided into the same p_t and $\phi - \Psi_R$ bins and subtracted.

- Finally, after background subtraction, we count the raw yields in the mass peak and get the azimuthal angle distributions.

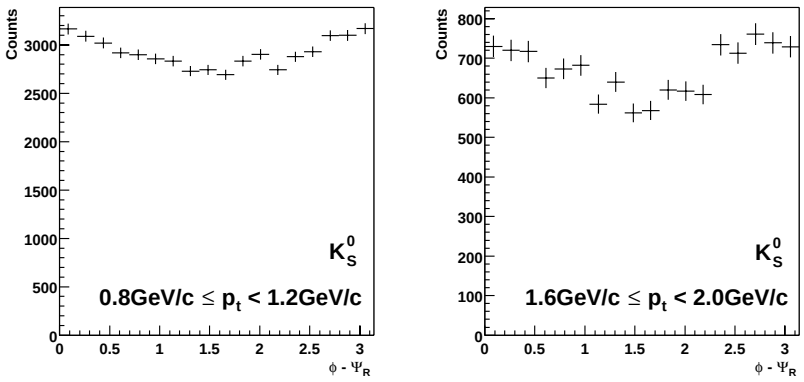

Figure 5.11: Azimuthal angle distribution for K^0_S from minimum bias events in two p_t bins 0.8 GeV/$c \leq p_t <$ 1.2 GeV/c (left) and 1.6 GeV/$c \leq p_t <$ 2.0 GeV/c (right)

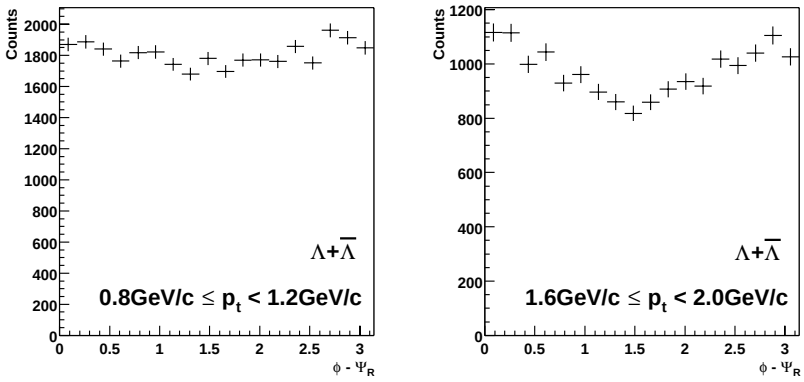

Figure 5.12: Azimuthal angle distribution for $\Lambda + \bar{\Lambda}$ from minimum bias events in two p_t bins 0.8 GeV/$c \leq p_t <$ 1.2 GeV/c (left) and 1.6 GeV/$c \leq p_t <$ 2.0 GeV/c (right)

The result for K^0_S in 0.8 GeV/$c \leq p_t <$ 1.2 GeV/c and 1.6 GeV/$c \leq p_t <$ 2.0 GeV/c are shown in Fig.5.11. $\Lambda + \bar{\Lambda}$ azimuthal angle distributions in the same p_t region are shown in Fig.5.12. The uncertainty in the ϕ distribution comes from both the signal and the background subtraction. Use S for signal, T for total reconstructed candidate and B for background, we have

$$S = T - B$$

$$(\Delta S)^2 = (\Delta T)^2 + (\Delta B)^2$$

$$\Delta T = \sqrt{T} \ , \ \ \Delta B = \sqrt{B}$$

From the $\phi - \Psi_R$ distribution, we calculate $v_2 = \langle cos[n(\phi - \Psi_R)]\rangle$ and the center position of every $\phi - \Psi_R$ bin is used in the calculation.

5.3.1 K^0_S and $\Lambda + \bar{\Lambda}$ v_2 from Minimum bias Collisions

The differential elliptic flow v_2 depends on mass, rapidity and p_t. In Fig.5.13, $v_2(p_t)$ is shown for K^0_S and $\Lambda + \bar{\Lambda}$ for minimum bias collisions, integrated over rapidity and centrality by taking the multiplicity-weighted average. The uncertainties shown are statistical only. The dashed-lines represent the hydrodynamic model calculations [100] for (from top to the bottom) pions, kaons, protons and lambdas. Also shown in the figure is the elliptic flow v_2 for charged particles[66]. Within statistical uncertainty, the K^0_S results are in agreement with the v_2 of charged kaons in the p_t range they share (300 MeV/$c \leq p_t \leq$ 700 MeV/c)[41]. We observe that v_2 for both strange particles increases as a function of p_t up to about 1.5 GeV/c, similar to the hydrodynamic model prediction. In the higher p_t region ($p_t \geq$ 2 GeV/c), however, the values of v_2 seem to be saturated and less than the hydrodynamic model predictions. This is also seen in the behavior of charged particles.

5.3.2 K^0_S and $\Lambda + \bar{\Lambda}$ v_2 Centrality Dependence

The differential elliptic flow $v_2(p_t)$ is plotted for K^0_S for two different centrality selections in the left panel of Fig.5.14, and for $\Lambda + \bar{\Lambda}$ in the right panel. The

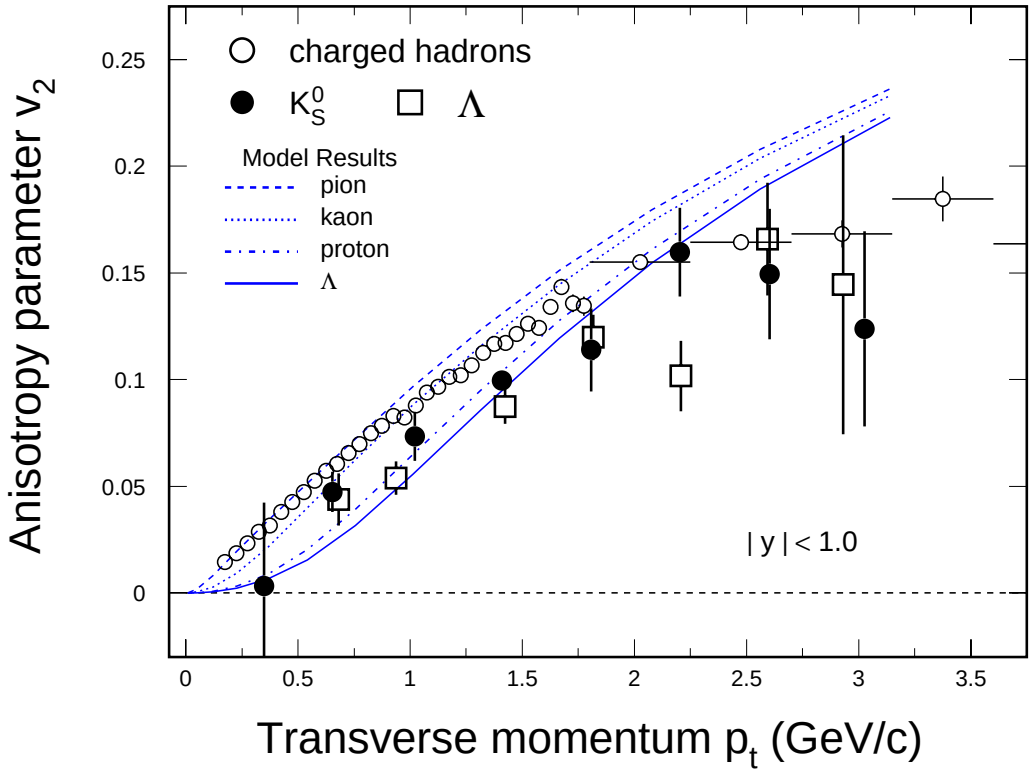

Figure 5.13: Elliptic flow v_2 as a function of p_t for the strange particles K^0_S (solid circles) and $\Lambda + \bar{\Lambda}$ (open squares) from minimum bias Au+Au collisions. For comparison, v_2 of charged particles (open circles) are also shown. The lines are from hydrodynamic model calculations[100].

circles represent the most central 11% of the measured cross section. The filled squares correspond to 11-45% of the measured cross section. The uncertainties on the points are statistical only. The two particles show a similar p_t dependence in the two centrality intervals. At a given p_t, the more peripheral collisions have the larger value of $v_2(p_t)$. The p_t dependence is stronger in more peripheral collisions than in the central collisions. A similar dependence was observed for charged hadrons in Au+Au collisions at the same RHIC energy[41]. In the hydrodynamic limit, the centrality dependence of elliptic flow is mainly determined by the initial elliptic anisotropy, ε, of the overlapping zone in the transverse plane[82], cf. Eqn.2.7. The ratio of the two should be approximately constant[81], i.e. $(v_2/\varepsilon)_{\rm hydro} \approx$ Const, depending on the equation of state used. This gives large v_2 for more peripheral collisions because of large initial spacial eccentricity.

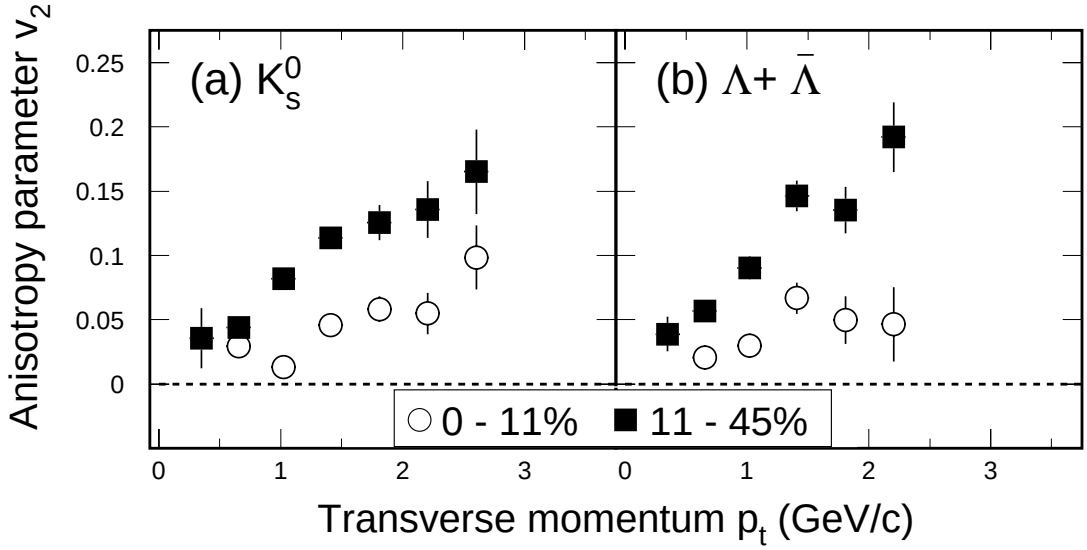

Figure 5.14: Elliptic flow v_2 as a function of p_t for K^0_S (left) and $\Lambda+\bar{\Lambda}$ (right). Filled circles and open squares are for central (0-11%) and mid-central (11-45%) collisions, respectively. Both minimum bias trigger and central trigger events are used.

5.3.3 p_t Integrated K^0_S and $\Lambda+\bar{\Lambda}$ v_2

The p_t integrated anisotropy parameters for negatively charged particles, K^0_S, and $\Lambda+\bar{\Lambda}$ are shown in Fig.5.15. Similar to Fig.5.13, the results are from minimum bias collisions. The integrated values of v_2 are calculated by parameterizing the yield with the inverse slope parameter of exponential fits to the K^0_S or $\Lambda+\bar{\Lambda}$ transverse mass distribution[66]. Although the $v_2(p_t)$ of $\Lambda+\bar{\Lambda}$ is below the $v_2(p_t)$ of K^0_S at each p_t as shown in Fig.5.13, the p_t integrated v_2 values increase with the particle mass. This increase reflects the relatively higher mean p_t of the $\Lambda+\bar{\Lambda}$ compare to the K^0_S where the integrated v_2 is dominated by the region near the particles mean p_t and is insensitive to the upper or lower bounds of the integration. In hydrodynamic models, although the spatial geometry of an anisotropic pressure gradient and the resultant collective velocity are the same for all particles, massive particles tend to gain larger transverse momenta and so develop a larger elliptic flow. The hydrodynamic model calculations[100], shown as a gray-band and central dashed line, are, within errors, in agreement with this result. The width of the gray-band in Fig.5.15 indicates the uncertainties of the model calculation, mostly due to the choice of the freeze-out

conditions. In the region near the particles mean p_t that dominates the value of the integrated v_2, assumptions used in the hydrodynamic model calculations are more likely to be valid. As a result, the apparent deviation of the measured v_2 from the hydrodynamic prediction for $p_t \geq 2$ GeV/c seen in Fig.5.13 is not strongly reflected in Fig.5.15. The increase of v_2 with particle mass is indicative that significant collective motion, perhaps established early in the collision, is an effective means to transfer geometrical anisotropy to momentum anisotropy. The nature of the particles during this process, however, whether parton or hadron, and the degree of thermalization for strange particles during the collective expansion remains an open issue.

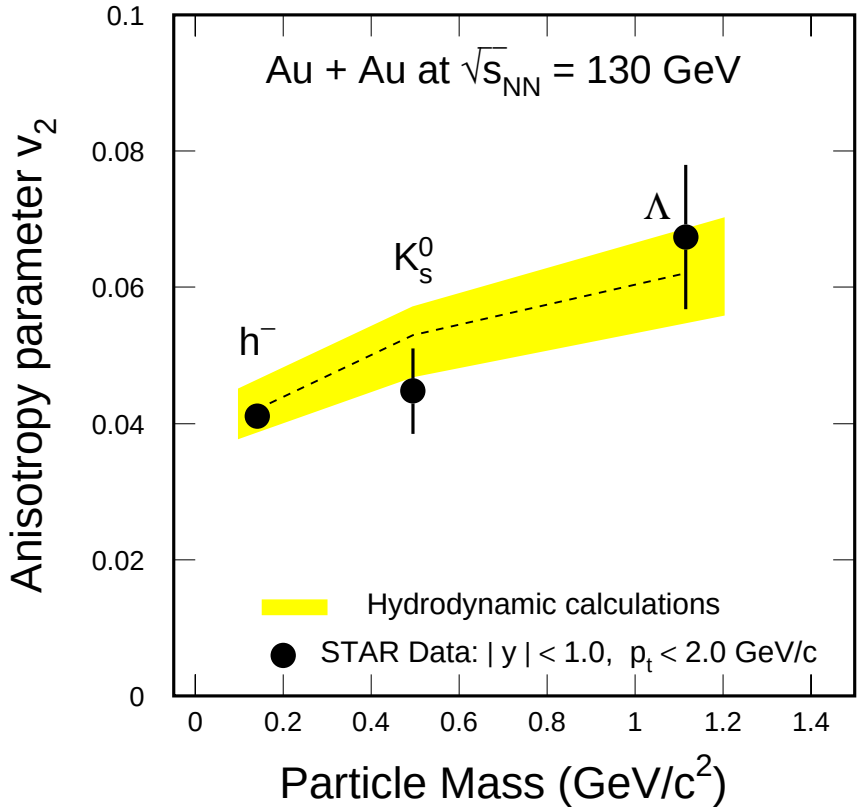

Figure 5.15: Integrated elliptic flow v_2 as a function of particle mass. The gray-band and central dashed line indicates the hydrodynamic model results[100].

5.4 Systematic Uncertainties

For this analysis, three main sources contribute to systematic errors in the measured anisotropy parameters:

- Particle identification
- Background subtraction
- Contributions to the anisotropy parameter from correlations unrelated to the reaction plane such as resonance decays, jets or Coulomb and Bose-Einstein correlations[77, 78]

The contributions from the first two sources are estimated by examining the variation in v_2 after changing several track and event cuts and using different background subtraction method. We estimate that these effects contribute an error of less than ± 0.005 to v_2 in low p_t region where more background is observed and high p_t region where statistics are low. Around mean p_t, where we have most of our statistics, there is almost no effect. The contribution to the azimuthal anisotropy from correlations unrelated to the reaction plane, however, could be significant, especially in peripheral collisions.

5.4.1 Four Particle Correlations

The standard flow analysis method as discussed above is based on a two-particle correlation methods. It assumes that azimuthal correlations between two particles are generated by the correlation of the azimuth of each particle with the reaction plane and this is used to extract the orientation of the reaction plane. However, it has been shown[66, 77] recently that, at ultra-relativistic energies, other sources of azimuthal correlations are of comparable magnitude and must be taken into account in the flow analysis. The most commonly discussed non-flow source of azimuthal correlations are global momentum conservation which might affect directed flow measurement

but not elliptic flow, Coulomb and Bose-Einstein correlations, resonance decay and jets.

A cumulant method based on higher order azimuthal correlations can be used to eliminate the non-flow effects[79]. The correlation between two particles is

$$\langle u_{n,1} {u^*}_{n,2} \rangle = \langle e^{in\phi_1} e^{-in\phi_2} \rangle = {v_n}^2 + \delta_n, \tag{5.2}$$

where n is the harmonic and the average is taken over all pairs of particles in an event sample. δ_n represents the contribution from non-flow correlations. Similarly, the correlation between four particles,

$$\langle u_{n,1} u_{n,2} {u^*}_{n,3} {u^*}_{n,4} \rangle = {v_n}^4 + 2 \cdot 2 \cdot {v^2}_n \delta_n + 2{\delta^2}_n. \tag{5.3}$$

The pure four-particle non-flow correlation, which is of order $1/N^3$ much smaller than direct two-particle correlations, is omitted from this expression. Flow contributions can be got by subtract from expression(5.3) twice the square of expression(5.2),

$$\langle\langle u_{n,1} u_{n,2} {u^*}_{n,3} {u^*}_{n,4} \rangle\rangle = \langle u_{n,1} u_{n,2} {u^*}_{n,3} {u^*}_{n,4} \rangle - 2\langle u_{n,1} {u^*}_{n,2} \rangle^2 = -{v_n}^4. \tag{5.4}$$

It is named "cumulant" to the order 4 and denoted by $\langle\langle \cdots \rangle\rangle$. Limited by statistics we use the conventional flow analysis method and estimate our systematic errors from non-flow contribution following the first two studies of elliptic flow in STAR[41, 23].

5.4.2 Estimate of non-Flow Effects

A previous study used the correlation of reaction plane angles from subevents to estimate the magnitude of non-flow contributions[41]. The correlation between two subevent reaction plane angle is

$$\begin{aligned} \langle \cos(2(\Psi_2^{(a)} - \Psi_2^{(b)})) \rangle &\approx \left\langle \frac{\sum_{i=1}^{M_{sub}} u_i}{\sqrt{M_{sub}}} \cdot \frac{\sum_{j=1}^{M_{sub}} u_j^*}{\sqrt{M_{sub}}} \right\rangle \\ &= \frac{M_{sub} M_{sub}}{M_{sub}} \langle u_i u_j^* \rangle \\ &\propto M_{sub}(v_2^2 + g), \end{aligned} \tag{5.5}$$

where M_{sub} is the multiplicity for a sub-event, g denotes the non-flow contribution to two-particle correlations. Non-flow effects are assumed to contribute to the first and second harmonic correlations by similar amounts, so the magnitude of the first harmonic correlation sets a limit on the non-flow contributions to v_2, see Fig.5.16. The peaked shape of the centrality dependence of $\langle\cos[2(\Psi^a - \Psi^b)]\rangle$ is characteristic of

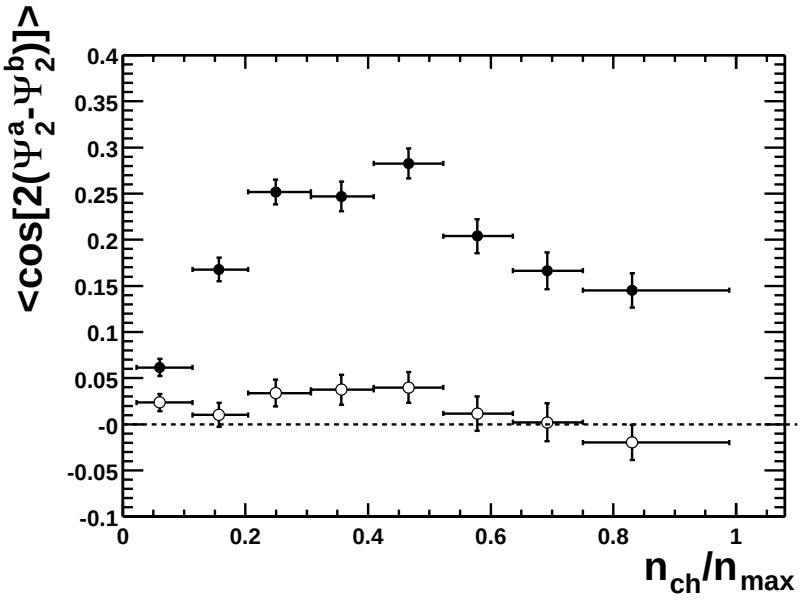

Figure 5.16: Correlation between the event plane angles determined for two independent subevents. The upper set is for the second harmonic ($n = 2$) and the lower set for the first harmonic ($n = 1$), figure from[23].

anisotropic flow whereas all known non-flow effects would be monotonic or almost constant for this quantity. The first harmonic correlation, shown in Fig.5.16, is significantly weaker than the second harmonic correlation. This sets an upper limit for the contribution of all non-flow effects to the second harmonic correlation and is the basis of our estimation of the systematic errors of elliptic flow. This study showed that the non-flow systematic errors for charged particles are typically -0.005, but are significantly larger in the more peripheral events where the error increases to -0.035 for the 58-85% most peripheral events. These effects always act to increase the measured value of v_2 above its true value so their contributions to the systematic error are asymmetric. These estimates are confirmed by measurements of v_2 using the 4th-order cumulant method[98]. The elliptic flow measured using this method

was consistent with the lower limit of the systematic errors from the traditional v_2 analysis method. The centrality averaged values of v_2 from the four-particle correlations are 15% lower than those obtained from the reaction plane analysis. The ratio of v_2 from the two method is approximately independent of pseudorapidity and transverse momentum within 0.1 GeV/c < p_t < 4.0 GeV/c. We assume the systematic errors on v_2 for the neutral strange particles K^0_S and $\Lambda + \bar{\Lambda}$ are similar to that found in the analysis of charged particles.

5.5 Discussion and Conclusion

5.5.1 Azimuthal Particle Distribution

The Fourier expansion of azimuthal particle distributions approach studies the event shapes which are sensitive to collective flow without assuming any model. The information provided in this way can be used for a comparison with different models. Fourier coefficients of different harmonics reflect different type of anisotropy. A three dimensional event shape can be obtained by correlating and combining the Fourier coefficients in the different rapidity windows.

Since the azimuthal distribution $r(\phi)$ is a periodic function it can be written in the form of Fourier expansion:

$$r(\phi) = \frac{x_0}{2\pi} + \frac{1}{\pi}\sum_{n=1}^{\infty}\left[x_n \cos(n\phi) + y_n \sin(n\phi)\right]. \tag{5.6}$$

The coefficients in the Fourier expansion of $r(\phi)$ are integrals of $r(\phi)$ with weights proportional to $\cos(n\phi)$ or $\sin(n\phi)$. For the case of a finite number of particles, the integrals become simple sums over particles found in the appropriate rapidity window:

$$\begin{aligned} x_n &= \int_0^{2\pi} r(\phi)\cos(n\phi)d\phi = \sum_{\nu} r_\nu \cos(n\phi_\nu), \\ y_n &= \int_0^{2\pi} r(\phi)\sin(n\phi)d\phi = \sum_{\nu} r_\nu \sin(n\phi_\nu), \end{aligned} \tag{5.7}$$

where ν runs over all particles. Without any flow and neglecting fluctuations the function $r(\phi)$ is constant, $r(\phi) = x_0/(2\pi) = 1/(2\pi)\sum_\nu r_\nu$. All Fourier coefficients

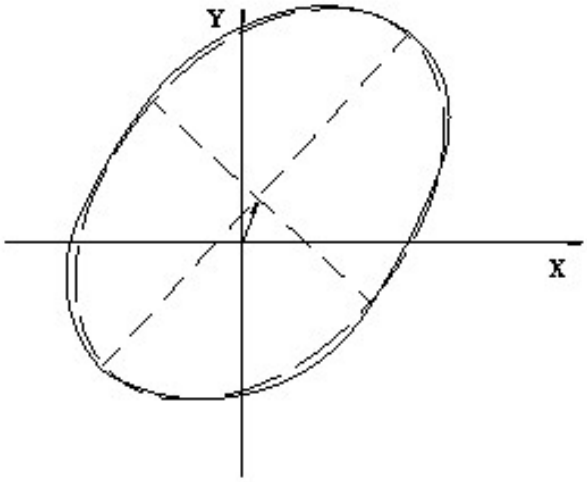

Figure 5.17: The azimuthal distribution $r(\phi)$ (solid line) approximate by ellipse (dashed line), figure from[101].

except x_0 would be zero. If flow is present, $r(\phi)$ is no longer a constant, and the shape of the distribution is no longer a circle centered at zero, see Fig.5.17. Each non-zero pair of the Fourier coefficients x_n and y_n indicates the presence of the "nth type" flow, which we characterize by the value of $v_n = \sqrt{x_n^2 + y_n^2}$, and by the angle $\Psi_n (0 \leq \Psi_n < 2\pi/n)$,

$$x_n = v_n \cos(n\Psi_n),$$
$$y_n = v_n \sin(n\Psi_n). \tag{5.8}$$

The first harmonic coefficients correspond to an overall shift of the distribution in the transverse plane, see Fig.5.17. That's directed flow v_1. If $r(\phi)$ is the transverse momentum distribution, v_1 is the magnitude of the total vector sum of transverse momenta. In the case of negligible fluctuations the direction of flow due to symmetry is to coincide with the reaction plane angle $\Psi_1 = \Psi_R$, or point in the opposite direction $\Psi_1 = \Psi_R + \pi$.

If approximates the azimuthal distribution by an ellipse, as shown in Fig.5.17, the v_2 is proportional to the magnitude of the eccentricity. The orientation of the major axis, defined by the angle Ψ_2 (or $\Psi_2 + \pi$, which give the same orientation for an ellipse) can be only Ψ_R or $\Psi_R + \pi/2$. In the case $\Psi_2 = \Psi_R$, the major axis

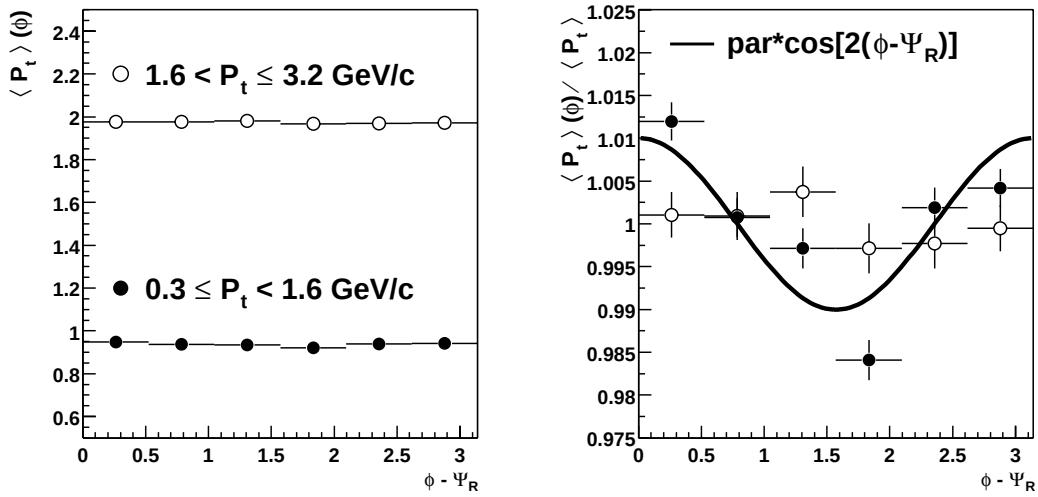

Figure 5.18: mean p_t as a function of azimuthal angle $\phi - \Psi_R$ unnormalized (left) or normalize by $\langle p_t \rangle$ from the corresponding p_t region (right) for K^0_S from minimum bias collisions. Thick line in the right panel is fitting result with function $C * \cos[2(\phi - \Psi_R)]$.

lies within the reaction plane, while $\Psi_2 = \Psi_R + \pi/2$ corresponds to an orientation of the ellipse perpendicular to the reaction plane. The coefficient v_3 is non-zero if the azimuthal distribution has a triangle-type "deformation". Any transverse flow would influence the p_t distribution of the observed particles. Fig.5.18 shows the mean p_t, $\langle p_t \rangle(\phi)$, as a function of azimuthal angle in low p_t and high p_t region for K^0_S from minimum bias collisions. The left panel is unnormalized distribution while the right panel is normalized by the average p_t, $\langle p_t \rangle$, in the corresponding p_t region. Thick line in the right panel is fitting with function $C * \cos[2(\phi - \Psi_R)]$, where C is a fitting parameter. Large 2nd-order azimuthal variation is observed in low p_t region (black dots) which is the characteristic of elliptic flow and it decreases in high p_t region (open circles). That means the contribution to v_2 from $\langle p_t \rangle$ oscillation is different in different p_t region. This is consistent with the results in a previous flow study paper from STAR[41]. There, a simple hydrodynamic motivated model is used to fit the transverse momentum dependence of anisotropic flow. Their results indicate that to have a good fit of the data we need more source elements moving in the direction of the reaction plane, i.e. the elliptic flow observed is not caused by an

azimuthal transverse velocity variation along, but by the combination of a velocity difference and a spatially anisotropic freeze-out hyper-surface.

5.5.2 Transverse Momentum Dependence

Mass Dependence at Low p_t

Fig.5.19 (left) shows the differential momentum anisotropy $v_2(p_t)$ for different hadron species for EOS Q and $T_f \approx 120$ MeV up to $p_t \sim 1.5$ GeV/c[100]. At a given value of p_t, the elliptic flow is seen to decrease with increasing particle mass. This is also observed in our measurement, cf. Fig.5.13, and a previous flow measurement from STAR[41], cf. Fig.5.19 (right), indicating the system created shows a behavior consistent with collective hydrodynamical flow.

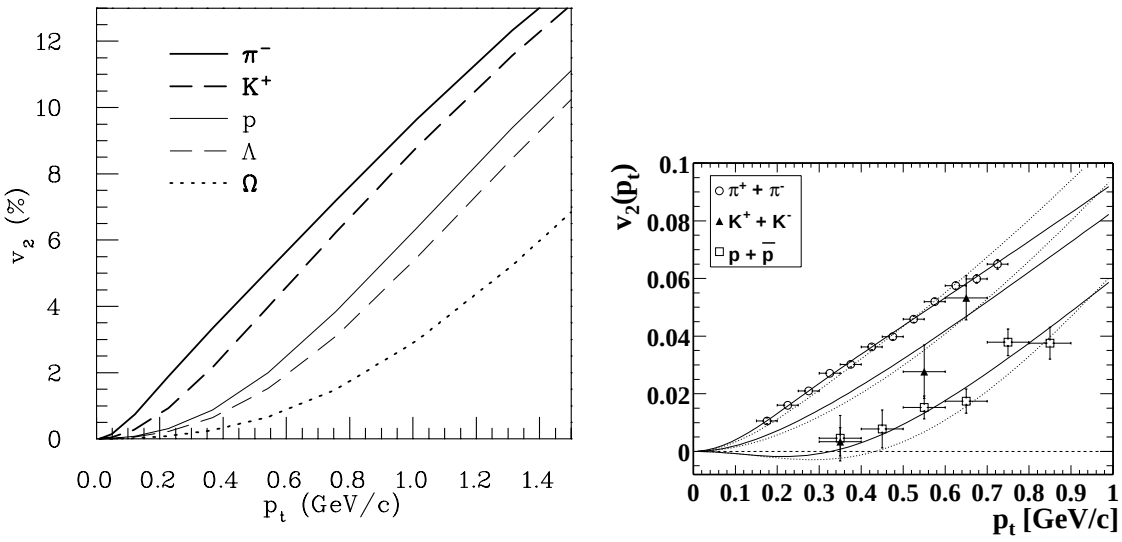

Figure 5.19: p_t-differential elliptic flow at mid-rapidity from minimum bias Au+Au collisions at $\sqrt{s_{NN}} = 130$A GeV for various hadrons from hydrodynamic calculation for EOS Q(120) (left), figure from[100], for pions, kaons and protons+antiprotons from STAR experiment (right), figure from[41]. The solid and dash lines in the right panel are hydrodynamic motivated model fitting.

This mass dependence can be understood as the result of an interplay between the mean expansion velocity, the elliptic component of the expansion velocity and the thermal velocity of the particles. A simple intuitive argument from hydrodynamics

take into account radial flow shifting the p_t-distributions to larger values of p_t. For non-relativistic, $p_t < m$, this effect increases with the particle mass m and the radial flow velocity $\langle v_\perp \rangle$. Relative to the case without radial flow, the spectrum is thus depleted at small p_t. The depletion as well as the p_t range over which it occurs increase with m and $\langle v_\perp \rangle$. In the case of fully developed elliptic flow, the radial velocity is larger in x than in y direction, $|v_x| > |v_y|$, which will result in a stronger depletion effect in x direction. Thus it eventually reduces v_2 at small p_t. This reduction and the p_t-range over which it occurs both increase with the particle mass m and the average radial flow $\langle v_\perp \rangle$. This rest-mass-dependence effect disappear at high p_t region where the mass difference between different hadron species becomes less relevant.

High p_t Azimuthal Asymmetry

At high p_t, a hydrodynamical description of the hadron production mechanism may break down as processes involving hard scattering of the initial-state partons are expected to play the dominant role. Calculations based on perturbative QCD predict that high energy partons traversing nuclear matter lose energy through induced gluon radiation[50], where the magnitude of the energy loss depends on the density of the medium[51]. The fragmentation products of partons that have propagated through the azimuthally asymmetric system generated by non-central collisions may exhibit azimuthal anisotropy due to energy loss and the azimuthal dependence of the path length. High p_t parton production in the direction of long axis of the overlapping region exhibits more collisions (inelastic and elastic) than that emitted along the short axis. It results in smaller probability to fragment into high p_t hadron. It provide important information about the initial conditions and dynamics in a heavy ion collision[104] and can be measured via the differential elliptic flow parameter $v_2(p_t)$.

At $p_t < 2\text{GeV}/c$, soft non-perturbative hydrodynamic like flow effects have to

be taken into account, this leads to

$$v_2(p_t) \approx \frac{v_{2s}(p_t)dN_s + v_{2h}(p_t)dN_h}{dN_s + dN_h} \ , \tag{5.9}$$

where subscript s and h represent the soft and hard component respectively. The resulting $v_2(p_t) \sim p_t$ is shown in Fig.5.20. In contrast to non-dissipative hydrodynamical calculations , cf. Fig.2.6 (right), v_2 coefficient decreases with increasing p_t at high transverse momenta.

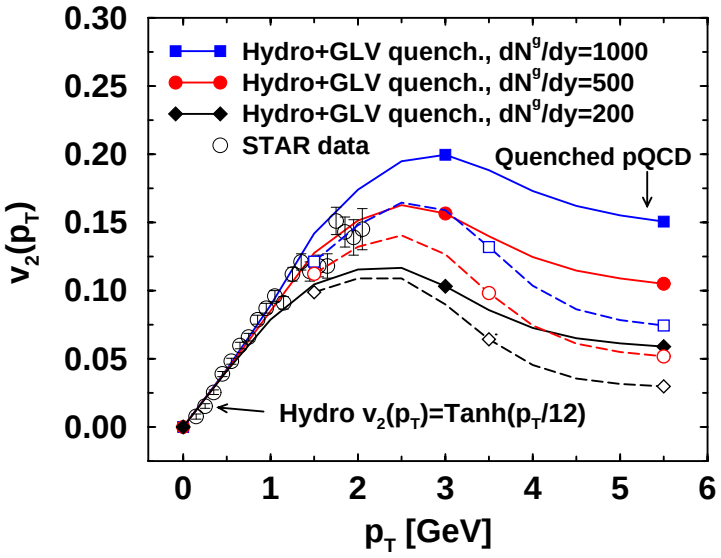

Figure 5.20: The interpolation of $v_2(p_t)$ between the soft hydrodynamic and hard pQCD, solid and dash line corresponding to Wood-Saxon geometry and sharp cylinder geometry respectively.

The observed K^0_S and $\Lambda + \bar{\Lambda}$ azimuthal anisotropy $v_2(p_t)$ saturation at $p_t > 2$ GeV/c, cf. Fig.5.13, deviate from non-dissipative hydrodynamics which predicts a monotonically increasing v_2 with increasing p_t. Recent measurements of inclusive charged hadron distributions in Au+Au collisions at $\sqrt{s_{NN}} = 130$ GeV also show a suppression of hadron yields at high p_t in central collisions relative to peripheral collisions and scaled nucleon-nucleon interactions[84, 99]. The data might indicate the effect of dissipative dynamics with finite parton energy loss. It could help in understanding the origin of particles in the region, do they acquire their transverse momentum due to multiple scattering or they come from a fragmentation of even higher p_t partons.

5.5.3 Conclusion

We made the first measurement of the anisotropy parameter v_2, for strange particles K^0_S and $\Lambda + \bar{\Lambda}$, from Au+Au collisions at $\sqrt{s_{NN}} = 130$ GeV. The v_2 values as a function of p_t from mid-central collisions are higher at each p_t than v_2 from central collisions. Hydrodynamic model calculations seem to provide an adequate description for elliptic flow of the strange particles up to a p_t of 2 GeV/c suggesting the system might equilibrate early. For p_t above 2 GeV/c, however, the observed v_2 seems to saturate whereas hydrodynamic models predict a continued increase with p_t. The p_t integrated v_2 as a function of particle mass is consistent with a hydrodynamic picture where collective motion, established by a pressure gradient, transfers geometrical anisotropy to momentum anisotropy. Although the hadronic scattering cross sections of strange and non-strange particles may be different, we have yet to see deviations in the measured v_2 from hydrodynamic calculations at low p_t for strange or non-strange particles. In a possible partonic phase prior to the hadronization epoch, the hadronic scattering cross sections for the final hadrons are not relevant. As such, if the elliptic flow of identified particles proves to be independent of their relative hadronic cross sections, it may be evidence that v_2 is established during a partonic phase. More theoretical work is necessary to understand these measurements and what they tell us about the nature of matter in the early stage of nuclear collisions.

Chapter 6

The Influence of Statistical Fluctuations on Erraticity Behavior of Multiparticle System

In a microscopic quantum system, such as inelastic collision of elementary particles at very high energy, it is often impossible to track the time evolution of their state. Instead the momenta of all charged particles in the final state can be determined precisely in experiments. For each collision event the momenta of these particles constitute a spatial pattern in momentum space. Erraticity method[11] was proposed by Cao and Hwa to characterize the event to event fluctuation of those patterns in experiments.

6.1 Sample Factorial Moments and Event Factorial Moments

Since the finding of unexpectedly large local fluctuations in high multiplicity event recorded by the JACEE collaboration[26], the investigation of non-linear phenomena in high energy collisions has attracted much attention[20]. The anomalous scaling of factorial moments, defined as

$$F_q = \frac{1}{M}\sum_{m=1}^{M}\frac{\langle n_m(n_m-1)\cdots(n_m-q+1)\rangle}{\langle n_m\rangle^q}, \tag{6.1}$$

at diminishing phase space scale or increasing division number M of phase space[5, 6]:

$$F_q \propto M^{-\phi_q}, \tag{6.2}$$

called intermittency (or fractal) has been proposed for characterizing this phenomenon in multiparticle system. The average $\langle \cdots \rangle$ in Eqn.6.1 is over the whole event sample and n_m is the number of particle falling in the mth bin. This anomalous scaling has been observed successfully in various experiments [35, 36, 90].

A recent new development further along this direction was made by Cao and Hwa in the event by event analysis[11, 12, 13]. They proposed to measure the (phase) space patterns in multiparticle system by the event factorial moments

$$F_q^{(e)} = \frac{\frac{1}{M}\sum_{m=1}^{M} n_m(n_m-1)\cdots(n_m-q+1)}{\left(\frac{1}{M}\sum_{m=1}^{M} n_m\right)^q} \tag{6.3}$$

Oppose to sample factorial moments defined in Eqn.6.1, event factorial moments Eqn.6.3 do not average over all events.

6.2 Erraticity

As pointed out by Cao and Hwa the event to event fluctuations of event factorial moments or the space patterns it measures can be quantified by its normalized moments as:

$$C_{p,q} = \langle \Phi_q^p \rangle, \quad \Phi_q = F_q^{(e)} \Big/ \langle F_q^{(e)} \rangle \,, \tag{6.4}$$

and by $dC_{p,q}/dp$ at $p = 1$:

$$\Sigma_q = \langle \Phi_q \ln \Phi_q \rangle \tag{6.5}$$

If there is a power law behavior of the fluctuation as division number goes to infinity, or as resolution $\delta = \Delta/M$ goes to very small, i.e.,

$$C_{p,q}(M) \propto M^{\psi_q(p)} \qquad (M \to \infty), \tag{6.6}$$

the phenomenon is referred to as erraticity[59]. The derivative of exponent $\psi_q(p)$ at $p = 1$

$$\mu_q = \frac{d}{dp}\psi_q(p) \mid_{p=1} = \frac{\partial \Sigma_q}{\partial \ln M} \tag{6.7}$$

describes the width of the fluctuation and so is called as "entropy index". In the following, we will refer to $C_{p,q}$ or Σ_q in Eqn.6.4 and Eqn.6.5 as "erraticity moments".

6.3 Statistical Fluctuations

It is well known that the obstacle of event by event analysis is the influence of statistical fluctuations caused by insufficient number of particles. The big advantage of sample factorial moments in Eqn.6.1 is that it can eliminate this kind of statistical fluctuations. It has been proved[5, 6] that if the statistical fluctuations of particles falling in a bin is poissonian like, then the sample factorial moments equal to the corresponding dynamic probability moments, see Appendix C on page 99:

$$F_q = C_q = M^{q-1} \sum_{i=1}^{M} \langle p_i^q \rangle \tag{6.8}$$

Again, the average is over the whole sample and p_i is the probability of particle falling in the ith bin in a certain event. However, we can not follow the same procedure to get the similar equation for event factorial moments of Eqn.6.3, although there is a horizontal average over bins in the equation. Since the number of particles in an event is not large enough and so is the number of bin, event factorial moments can not completely eliminate statistical fluctuations and present the dynamic probability moments associated with it, see Appendix C. How large of the statistical fluctuations in erraticity analysis is and how it depends on the number of multiplicity have not been seriously estimated yet. We will answer these questions quantitatively here.

6.3.1 Flat Probability Distribution

To be direct and obvious, we first use an unique flat probability distribution in whole studying interval and whole sample. It means that the probabilities in all bins are equal and are the same for different events. For simplicity, we use only fixed number of multiplicity. In this case the denominator in the definition of factorial moment, Eqn.6.1 and Eqn.6.3, becomes simply $N(N-1)\cdots(N-q+1)$ [5, 6]. We first take

$N = 9$, which is about the average multiplicity at ISR energies. The distribution of particle in the whole studying phase region in an event can be readily located by Bernouli distribution:

$$B(n_1, \ldots, n_M | p_1, \ldots, p_M) = \frac{N!}{n_1! \cdots n_M!} p_1^{n_1} \cdots p_M^{n_M}, \quad \sum_{m=1}^{M} n_m = N \tag{6.9}$$

By this way, we simulate a sample with 1000 events. The results of the second order sample factorial moments F_2, erraticity moments $C_{p,2}$ and Σ_2 versus the division number M of the phase space region are shown in Fig.6.1(a). The second order sample factorial moment is a constant with the increasing of division number. This is what we expect. Since no dynamic is input, it becomes a constant after eliminating the statistical fluctuations. While the increase of erraticity moments $C_{p,2}$ and Σ_2 with division number is measurably large. These contributions come from pure statistical fluctuations of event factorial moments due to the insufficient number of particle in an event since there is no dynamic fluctuation from event to event in the case. This result can fully recover what has observed in NA27 data[94], cf. the open circles in the second figure of Fig.6.1(a). This means that in low multiplicity sample, the statistical fluctuations of event factorial moments dominate the erraticity behavior of multiparticle system. Event factorial moments is not a good representation of event dynamics for low multiplicity events.

However, erraticity analysis proposed a very important way to study the event by event fluctuations, though we are still not clear whether there are such fluctuations and if there are what mechanism causes them. We have demonstrated in our former paper[47] that if and only if different events have different dynamic fluctuation strengths, the erraticity moments will keep increasing with the increasing of division number and so has nonzero entropy index.

As is well known, the statistical fluctuations will become negligible if the multiplicity of an event is large enough. At how high a multiplicity the event factorial moments can measure the dynamical fluctuations of a finite particle system is a very meaningful question.

Let us switch the fixed multiplicity N to 20 and 300 in the above mentioned

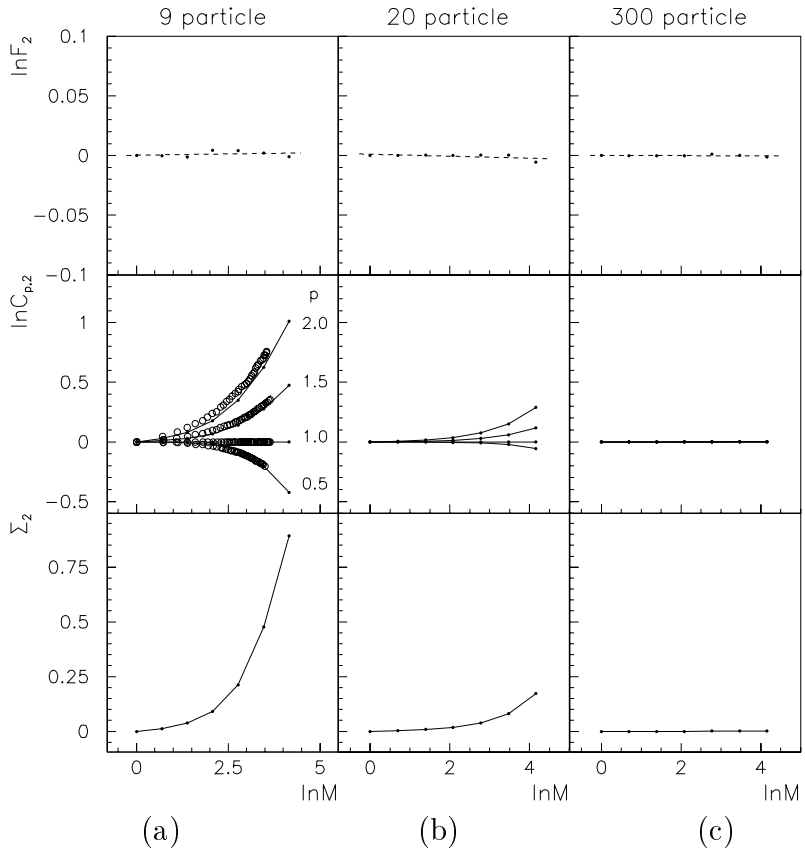

Figure 6.1: The dependence of the logarithm of the second order sample factorial moments F_2, erraticity moments $C_{p,2}$ and Σ_2 on that of the phase space division number M for a flat probability distribution with particle number equal to 9(a), 20(b) and 300(c), respectively. The dashed lines are linear fit. The solid lines are for guiding the eye. The open circles are result from NA27 data, taken from Ref.[94].

simulation. The corresponding second order sample factorial moments F_2, erraticity moments $C_{p,2}$ and Σ_2 versus the division number M of the phase space region are shown in Fig.6.1(b) and (c) respectively. The second order sample factorial moment keep to be a constant as we know. The erraticity moments become flatter and flatter with the increase of multiplicity. It means that pure statistic fluctuations of event factorial moments are greatly depressed by the increase of multiplicity.

From Fig.6.1, we can see that, when multiplicity is larger than 300, event factorial moments can be approximately used to describe the event spatial pattern associated with it and its moments – erraticity moments – can represent the erraticity behavior of the system.

6.3.2 Simulation with Random Cascading α Model

In order to confirm this upper limit of multiplicity, we do following parallel analysis for a system with dynamic fluctuation from event to event.

Random cascading α model is the simplest model which can be used to generate a sample with non-zero entropy index. We will use it for our quantitative discussion below. In the random cascading α model, the M division of a phase space region Δ is made in steps. At the first step, it is divided into two equal parts; at the second step, each part in the first step is further divided into two equal parts, and so on. The steps are repeated until $M = \Delta Y/\delta y = 2^\nu$. How particles are distributed from step to step between the two parts of a given phase space cell is defined by the independent random variable $\omega_{\nu j_\nu}$, where j_ν is the position of the sub-cell($1 \leq j_\nu \leq 2^\nu$) and ν is the number of steps. It is given by[105]:

$$\omega_{\nu,2j-1} = \frac{1}{2}(1+\alpha r) \quad ; \quad \omega_{\nu,2j} = \frac{1}{2}(1-\alpha r) \quad , \quad j = 1,\ldots,2^{\nu-1} \tag{6.10}$$

where, r is a random number distributed uniformly in the interval [-1,1]. α is a positive number less than unity, which determines the region of the random variable ω and describes the strength of dynamical fluctuations in the model[69]. If it changes from event to event, there will be different dynamical fluctuation strength in different events. Here, let it has a Gaussian distribution. The mean and variance of the Gaussian are both chosen as 0.22. After ν steps, the probability in the mth window ($m = 1,\ldots,M$) is $p_m = \omega_{1j_1}\omega_{2j_2}\cdots\omega_{\nu j_\nu}$.

Using the model, we generate 1000 events. The logarithm of second order sample probability moment $\ln C_2$, and erraticity moments $\ln C_{p,2}$ and Σ_2 as a function of $\ln M$ are shown in Fig.6.2(a). Now the sample probability moment $\ln C_2$ has a power law behavior as dynamic fluctuations have been input. The erraticity moments also show a power law behavior at large division number region. It represents the dynamic fluctuation from event to event. The corresponding entropy index obtained from a linear fit to the last 3 points of Σ_2 is $\mu_2 = 0.0161$.

Finite number of particle can also be added to the above pure dynamic fluctu-

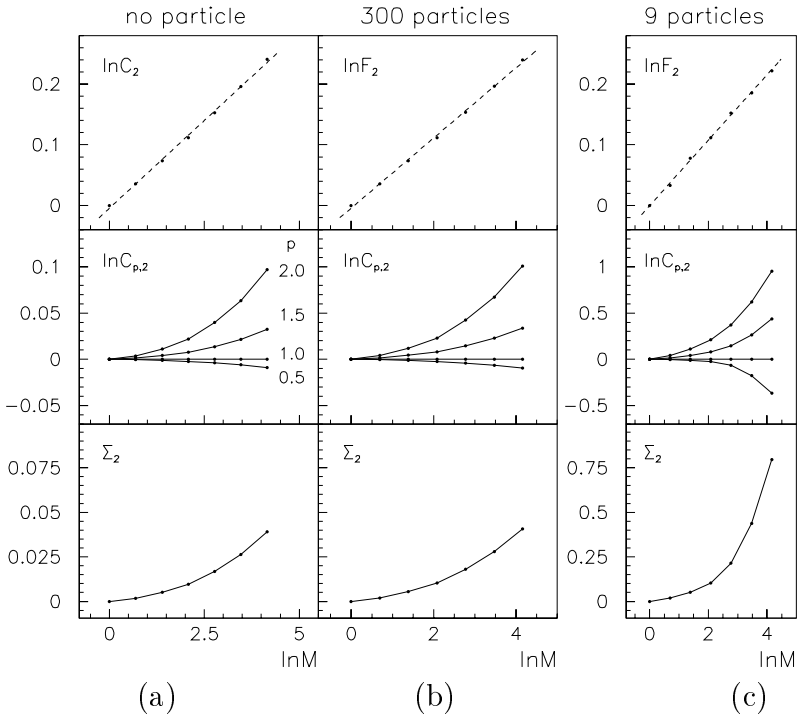

Figure 6.2: (a)The dependence of the logarithm of the second order probability moments C_2, erraticity moments $C_{p,2}$ and Σ_2 on that of the phase space division number M for the α model with Gaussian distributed α. (b)The same as (a) but for the sample factorial moments F_2 and the corresponding erraticity moments $C_{p,2}$ and Σ_2 with 300 particles. (c)The same as (b) but with 9 particles. The dashed lines are linear fit. The solid lines are for guiding the eye.

ation model by Bernouli distribution of Eqn.6.9. Again, we put $N = 9$ first. The corresponding factorial moment and erraticity moments are given in Fig.6.2(c). The value of erraticity moments now are much larger than those obtained from the original pure dynamic fluctuations in Fig.6.2(a). The entropy index, $\mu_2 = 0.422$, also turns out to be more than one magnitude bigger. This results confirm us again that the erraticity behavior is dominated by statistical fluctuations in low multiplicity sample if we use event factorial moments to characterize it. Though there is dynamic fluctuation from event to event, it will be merged to large statistical fluctuations in the case.

Secondly, we let $N = 300$. The corresponding factorial and erraticity moments are shown in Fig.6.2(b). The erraticity moments now approach to its original dynamic fluctuation values in Fig.6.2(a) and entropy index is $\mu_2 = 0.0168$ close to

its real value 0.0161. So we get the same conclusion as pure statistic fluctuation case. When multiplicity is larger than 300, erraticity behavior of the system can be estimated by the fluctuation of event factorial moments.

6.3.3 Multiplicity Dependence

To show quantitatively the influences of statistic fluctuations on erraticity behavior at different multiplicity cases, we simulate various number $N = 5, \ldots, 1000$ of particles in an event for both flat probability distribution and above described α model cases. The corresponding entropy indices are given in Fig.6.3 as full circles (flat distribution) and full triangles (α model) respectively. We can see that both of them decrease with multiplicity. For flat probability distribution, entropy index of statistical fluctuation is depressed more than three orders of magnitude when multiplicity N increases from a few to 300. After multiplicity $N > 300$, the entropy index is unmeasurably small. Meanwhile, the entropy index of α model sample approaches to its real dynamic value $\mu_2 = 0.0161$, cf. the solid line in Fig.6.3, after $N > 300$. This means that the erraticity analysis given by event factorial moments is applicable for heavy ion collisions, when the average multiplicity is higher than 300, where the influence of the statistical fluctuations is weak. Note that the multiplicity of heavy ion experiments at RHIC and forthcoming LHC is higher than this number.

6.4 Event Probability Moments

If the multiplicity is higher than a thousand, which has been recorded by NA49 experiment and RHIC experiments, the factorial moments analysis of a single event is unnecessary anymore as $n_m(n_m - 1)\cdots$ does not make much difference from $n_m \cdot n_m \cdot \cdots$ in most of the phase space bins which provides main contribution to the anomalous scaling of moments. In these cases the probability distribution in an event can be approximately presented by[61]:

$$p_m \approx \frac{n_m}{N}, \quad 1 = \sum_{m=1}^{M} p_m \tag{6.11}$$

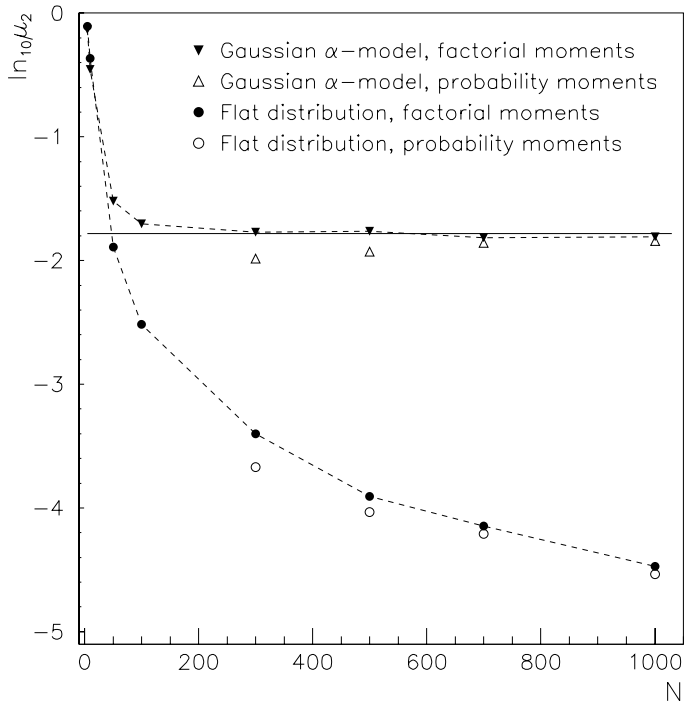

Figure 6.3: The dependence on number of particle of the entropy indices μ_2 for Gaussian α model calculated from event-factorial-moments (full triangles) and from probability-moments (open triangles). The same for flat distribution (full and open circles). The solid line is the dynamical result without statistical fluctuation. The dashed lines are for guiding the eye

The erraticity moments of event probability moments can be consequently defined by:

$$C_{p,q} = \langle \Phi_q^p \rangle, \quad \Phi_q = \sum_{m=1}^{M} p_m^q \Big/ \langle \sum_{m=1}^{M} p_m^q \rangle \tag{6.12}$$

By this definition, we repeat the analysis for both the flat probability distribution and the dynamic fluctuation distribution cases. It is a little smaller than the corresponding event factorial moments analysis at flat probability distribution case, cf. the open and full circles in Fig.6.3, and so it depresses the influence of statistical fluctuations more. The dynamic fluctuations of event to event in the α model case can still be abstracted out as done by the event factorial moments description, cf. the open and full triangles in Fig.6.3.

Chapter 7

Erraticity Analysis of Multiparticle Production in π^+p and K^+p Collisions at 250 GeV/c

Erraticity analysis has been performed in both hadron-hadron and nucleus-nucleus collisions[94, 70]. All the results show positive value of entropy index, μ_q, indicating the existence of erraticity behavior, i.e. fluctuations from event to event, in multiparticle systems. However, the cause of these fluctuations is still unclear. Here, the erraticity analysis results of π^+p and K^+p collisions at 250 GeV/c and comparison with Monte Carlo simulation will be discussed.

7.1 Data Sample

In the CERN experiment NA22, the European Hybrid Spectrometer (EHS) was equipped with the Rapid Cycling Bubble Chamber (RCBC) as an active target and exposed to a 250 GeV/c tagged, positive, meson enriched beam. In data taking, a minimum bias interaction trigger was used. The details of spectrometer and trigger can be found in[24, 72].

Charged particle tracks are reconstructed from hits in the wire- and drift-chambers of the two-lever-arm magnetic spectrometer and from measurements in the bubble

chamber. The momentum resolution varies from 1-2% for tracks reconstructed in RCBC, to 1-2.5% for tracks reconstructed in the first lever arm and is 1.5% for tracks reconstructed in the full spectrometer.

Events are accepted for the analysis when the measured and reconstructed charge multiplicity are the same, charge balance is satisfied, no electron is detected among the secondary tracks and the number of badly reconstructed (and therefore rejected) tracks is 0. The loss of events during measurement and reconstruction is corrected for by applying a multiplicity dependent event weight normalized to the topological cross sections given in [43, 44]. Elastic events are excluded. Furthermore, an event is called single-diffractive and excluded from the sample if the total charge multiplicity is smaller than 8 and at least one of the positive tracks has a Feynman variable $|x_F| > 0.88$. After these cuts, the inelastic, non-single-diffractive sample consists of 59 200 π^+p and K^+p events.

For laboratory momenta $p_{lab} < 0.7\text{GeV}/c$, the range in the bubble chamber and/or the change of track curvature is used for proton identification. In addition, a visual ionization scan is used for $p_{lab} < 1.2\text{GeV}/c$ on the full K^+p and on 62% of the π^+p sample. Positive particles with $p_{lab} > 150\text{GeV}/c$ are given the identity of the beam particle. Other particles with momenta $p_{lab} > 1.2\text{GeV}/c$ are not identified in the present analysis and are treated as pions.

In spite of the electron rejection mentioned above, residual Dalitz decay and γ conversion near the vertex still contribute to the two particle correlations. Their influence on our results has been investigated in detail in[46].

The data are based on the CERN experiment NA22 with 43680 events which has non-zero single event (charged) multiplicity so that its event factorial moment can be calculated. The initial intervals of the three phase space variables, rapidity y, azimuthal angle ϕ and transverse momentum p_t for the analysis, are defined as: $-2 \leq y \leq 2$, $0 \leq \phi \leq 2\pi$, $0.001 \leq p_t \leq 10\text{GeV/c}$ respectively. In order to reduce the effect of non-flat particle density distribution $\rho(x)$ in phase space, cumulative

variable

$$X(x) = \int_a^x \rho(x)dx \Big/ \int_a^b \rho(x)dx \tag{7.1}$$

is taken for all variables. In Eqn.7.1 a and b are the extreme points of the distribution $\rho(x)$.

7.2 Results and Discussion

7.2.1 Erraticity Behavior in Different Phase Space

The results of Σ_2 in one dimensional rapidity, transverse momentum components p_y, p_z and azimuthal angle ϕ are shown in Fig.7.1(a)-(d). The power law behavior of Σ_2 as division number goes to large indicates that there is erraticity in π^+p and K^+p collisions at 250 GeV/c. They are similar to erraticity behavior given by NA27 data[94]. Entropy index μ_2 can be obtained by linear fits of Σ_2 vs. $\ln M$. For a better linear fit, the first seven points are omitted. It can be seen from the figures that the values of Σ_2 and μ_2 in different variables are almost the same. That is to say, erraticity is independent of phase space variable in which we do the analysis.

Further, $C_{p,2}$, Σ_2 vs. $\ln M$ in three dimensional (y, p_t, ϕ) region are shown in Fig.7.2. In comparison to one dimensional results, three dimensional results have much better linear behavior after omitted first two points. This is different from the intermittency behavior, where even in three dimensional phase space, sample factorial moments still show a upward bending behavior and has been well explained by self-affine fractal mechanism[107, 37, 38].

7.2.2 Erraticity Behavior and the Single Event Variables $\bar{p_t}$ and N

A natural way to find out which factor does affect the erraticity behavior is to study the relations between erraticity behavior and other physical quantities. In order to see if erraticity has different behavior for different (hard or soft) processes, we first

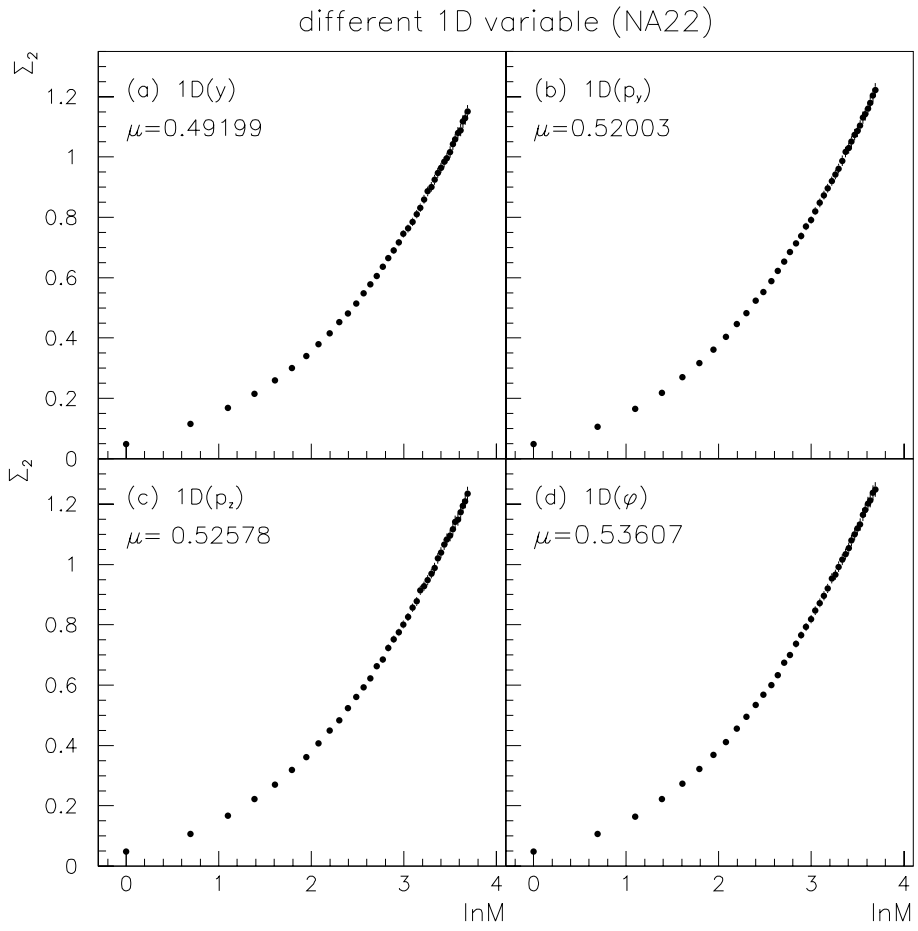

Figure 7.1: Σ_2 vs. $\ln M$ in one dimension, (a) y (p_x) region, (b) p_y region, (c) p_z region, (d) ϕ region.

show how it changes with different average transverse momentum per event. The later is defined as

$$\bar{p_t} = \sum_{i=1}^{n} p_{ti}/n, \tag{7.2}$$

where n is the total number of (charged) particles in the event. It has been shown[106] that $\bar{p_t}$ is a good variable to characterize the soft or hard degree of an event. The (unnormalized) distribution of (charged) multiplicity n and average transverse momentum per event $\bar{p_t}$ in the studied sample are shown in Fig.7.3. The average multiplicity and average transverse momentum of the whole sample are:

$$\langle n \rangle = \sum_{i=1}^{N} n_i/N = 7.979, \tag{7.3}$$

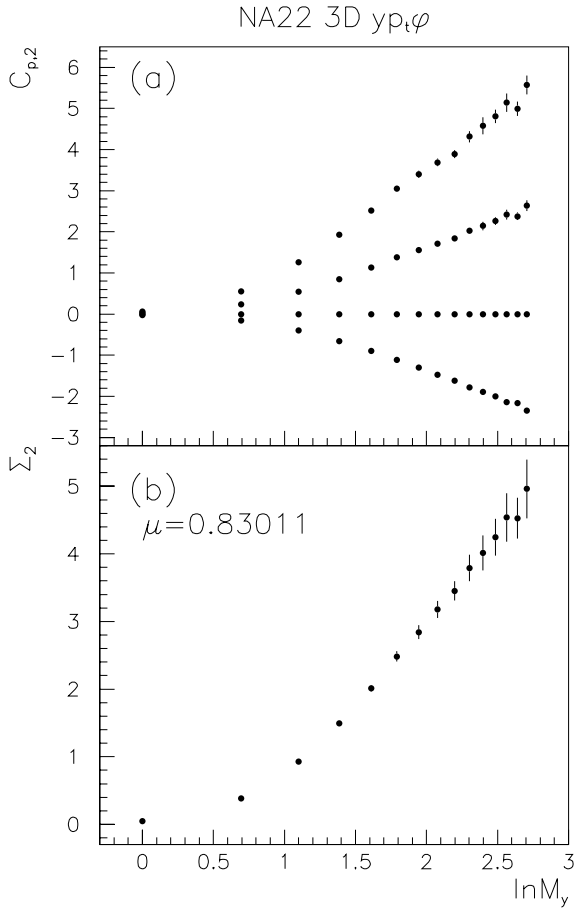

Figure 7.2: Three dimension (y, p_t, ϕ) region, (a) $C_{p,2}$ vs. $\ln M$ and (b) Σ_2 vs. $\ln M$.

$$\langle \bar{p}_t \rangle = \sum_{i=1}^{N} \bar{p}_{t_i}/N = 0.383, \tag{7.4}$$

where N is the number of event used. We divide the whole sample into three subsamples, i.e. $\bar{p}_t < 0.28$, $0.28 < \bar{p}_t < \langle \bar{p}_t \rangle$ and $\bar{p}_t > \langle \bar{p}_t \rangle$, cf. the dashed lines in Fig.7.3 lower left panel. The values of Σ_2 are calculated in these three different $\bar{p}_t$ regions respectively. The results in both one dimensional rapidity and three dimensional (y, p_t, ϕ) are shown in two upper panel in Fig.7.4

It can be seen from Fig.7.4 that, in both one dimensional and three dimensional cases, Σ_2 is almost the same for different $\bar{p}_t$ subsamples. It means that erraticity behavior at this collision energy does not relate to the soft or hard degree of an event, or to the gluon or quark jet as argued in NA27 erraticity analysis paper[94].

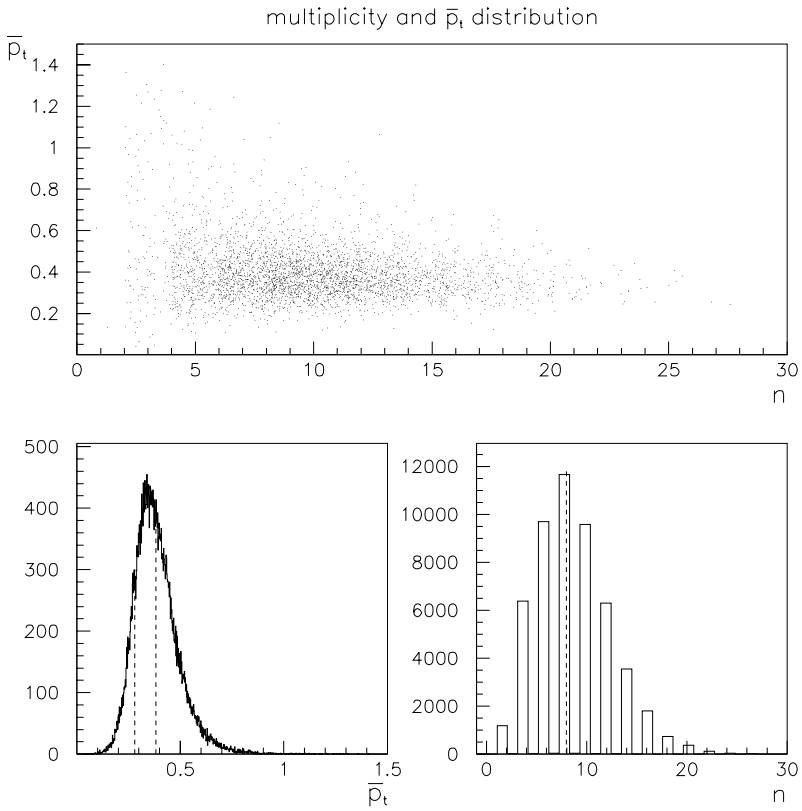

Figure 7.3: Distribution of multiplicity n and single event average transverse momentum $\bar{p}_t$, n, $\bar{p}_t$ scatter plot (upper panel), distribution of $\bar{p}_t$ (lower left panel), distribution of n (lower right panel).

Then, we turn to study the relation between erraticity and multiplicity. We divide the whole sample into two subsamples with $n < \langle n \rangle$ and $n > \langle n \rangle$, cf. the dashed line in Fig.7.3 lower right panel. The results of Σ_2 calculated in these two different multiplicity regions for both one and three dimensional cases, together with the total sample result, are shown in two lower figures of Fig.7.4.

It can be seen from the figures that for different multiplicity subsamples, it shows significantly different entropy indices. This means that the erraticity behavior depends strongly on multiplicity. The value of entropy index in higher multiplicity sample is much smaller than in lower ones. It means much less fluctuation from event to event in high multiplicity sub-sample. As we demonstrated in the previous chapter, when total multiplicity is very low, event factorial moments defined in Eqn.6.3 can not fully eliminate statistical fluctuation due to insufficient number of

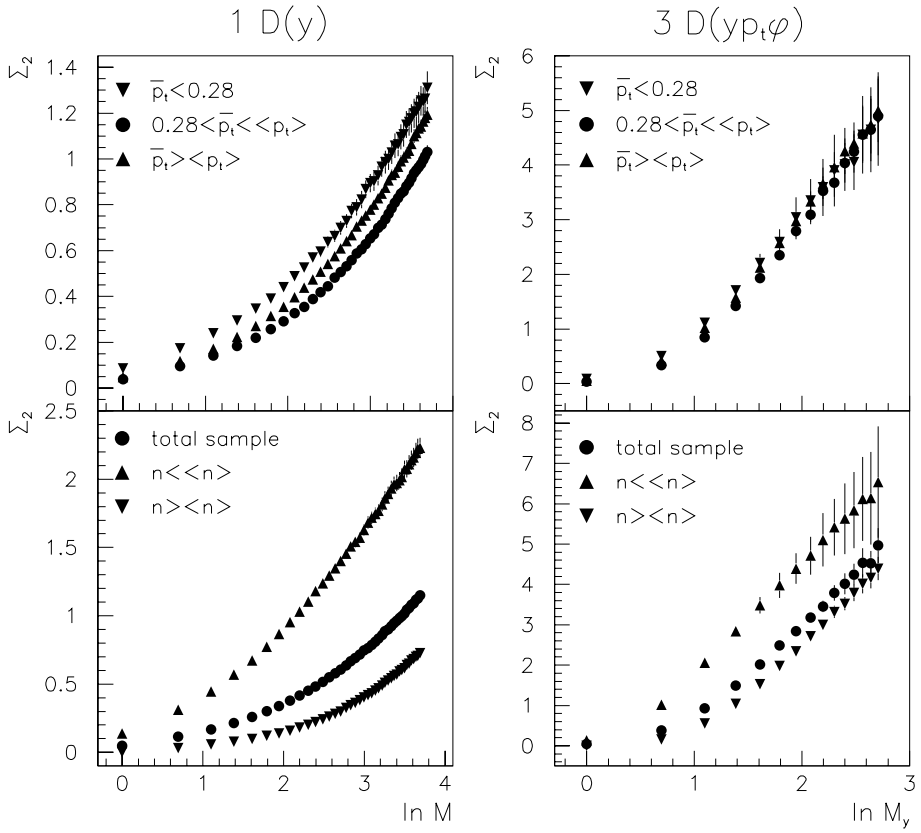

Figure 7.4: Σ_2 vs. ln M of different $\bar{p_t}$ sub-sample (two upper panels) and multiplicity sub-sample (two lower panels), in one dimension rapidity (two left panels) and three dimension y, p_t, ϕ (two right panels) phase space. The total sample result is shown in the lower panels together with the different multiplicity sub-sample result for comparison.

particles[62]. The lower multiplicity is, the bigger statistical fluctuations contain in event factorial moments. So the relation between erraticity and multiplicity may imply the contribution from this trivial statistical fluctuations. To confirm this argument, we made the following model comparisons.

7.3 Comparison with Monte Carlo Models

As we know, various models that simulate low p_t processes in multiparticle production can readily generate the average quantities, but failed in getting correctly the fluctuations from the average[20]. In particular, few models can fit the intermittency

data[43, 44]. A color mutation model ECOMB, proposed recently by Z. Cao and R. Hwa, is one of the few that can reproduce intermittency data[14]. The results of erraticity moments $\ln C_{2,2}$ and Σ_2 versus the logarithm of the division number M in one dimensional rapidity region getting from ECOMB at $\sqrt{s} = 22$ GeV are shown in Fig.7.5 (open triangles connected by dotted line) together with the experimental results from NA22 (full circles). We can see that the results from ECOMB agrees with the experimental results well.

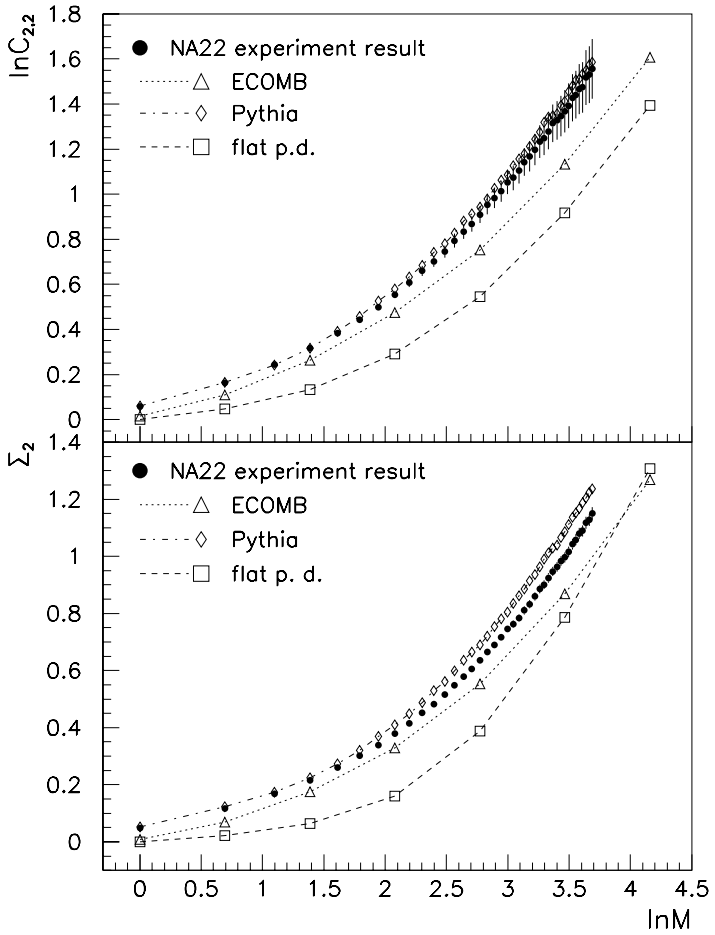

Figure 7.5: Erraticity moments $\ln C_{2,2}$ (upper panel) and Σ_2 (lower panel) vs. the division number $\ln M$ of the phase space region for NA22 data (full circles), ECOMB MC result (open triangles connected by dotted line), PYTHIA MC result (open rhombus connected by dot-dashed line) and a flat probability distribution with particle number equal to 7 (open squares connected by dashed line).

Then we use the LUND Monte Carlo event-generator PYTHIA 5.5 to simulate

π^+p collisions at 250 GeV/c to see if it has erraticity behavior or not. It has been shown that PYTHIA MC cannot reproduce the intermittency data and its average factorial moment value is almost the same for different division number. The resulting $\ln C_{2,2}$ and Σ_2 versus the logarithm of division number M from PYTHIA are also shown in Fig.7.5 as open rhombus connected by dot-dashed line. It turns out that the PYTHIA results agree with data even better than ECOMB. So, again, erraticity behavior in such kind of low collision energy may not be something dynamical but mainly due to trivial statistical fluctuations.

In order to be more convincing, 50,000 pure statistical fluctuation events (cf. Sec. 6.1 on page 77) with fixed number of multiplicity $N = 7$ is generated. The result of $\ln C_{2,2}$ and Σ_2 from this sample are shown in Fig.7.5 (open square connected by dashed line), which can also reproduce the tendency of erraticity behavior of NA22 data. It is a little smaller than experimental data as we fixed multiplicity. So the erraticity behavior of NA22 data is mainly a reflection of the statistical fluctuations due to insufficient number of particles at this low collision energy. This is consistent with the results in [62].

7.4 Conclusion

From the simple discussion above, we can make the following conclusions: If we use event factorial moments to measure spatial pattern, in very low multiplicity sample, such as the sample at ISR energies, statistical fluctuations caused by insufficient number of particle in an event will control the erraticity behavior of the system. One dimensional and three dimensional (y, p_t, ϕ) analyses of π^+p and K$^+$p collisions at 250 GeV/c indicate that erraticity behavior is independent of the phase space variable used and the average transverse momentum of the sample. However, it strongly depends on multiplicity which comes from large statistical fluctuations of event factorial moments in low multiplicity sample. Therefore, the physical conclusions from the experimental data on these kind of sample can not be treated seriously. However, if the multiplicity of studying sample is larger than 300, the in-

fluence of statistical fluctuations on erraticity behavior is negligible. Therefore, the erraticity behavior, if any, could be well observed in current and future heavy-ion collisions. Furthermore, if the multiplicity of an event is larger than a thousand, the probability moments defined by Eqn.6.11 and Eqn.6.12 can present erraticity behavior of the system as well as the event factorial moments.

Chapter 8

Outlook

RHIC has completed two run cycles. The first run ended in September, 2000 at $\sqrt{s_{NN}} = 130$ GeV and the second run ended in January, 2002 at $\sqrt{s_{NN}} = 200$ GeV. The next run will start later this year. Ultra-relativistic heavy ion collisions continue to offer a huge spectrum of exciting new opportunities, particularly on large distance scales not reachable in few hadron collisions. Matter has been produced at densities 10 times greater than normal nuclear matter density and strongly interact with itself. Quark and gluon degrees of freedom play a more visible role at RHIC than at SPS and QCD is being more directly involved in the interpretation of the data. The strength of the anisotropy flow, which describe the asymmetry momentum space particle emission after a heavy ion collision, is directly connected to the mean free path of the particles (partons, hadrons) forming the hot mid-rapidity region. The measurement of v_2 might therefore yield valuable information about the transport properties of QCD-matter, like the interaction frequencies of the excited partonic and hadronic matter at RHIC energies. Strange particles, K^0_S Λ Ξ especially ϕ meson and Ω baryon, with their small hadronic cross section, are supposed to measure QGP properties without any additional disturbance due to the hadronic phase.

The measured mass dependence of $v_2(p_t)$ below 2 GeV/c is in close agreement with full hydrodynamic model calculations, suggesting that in Au+Au collisions at $\sqrt{s_{NN}} = 130$GeV, the system created which for central and mid-peripheral collisions evolve rapidly towards local thermal equilibrium followed by hydrodynamic expan-

sion. More statistics is needed to address whether strange particles really follow the hadrodynamic calculation like the other charged particles and how it behave at high momentum region. By measuring v_2 at high p_t for different hadron species, we can determine whether jet quenching occurs or to what degree the matter has thermalized and the fundamental thermalization time scale in the early stages of a relativistic heavy ion collision. If thermalization has happened, we can measure the equation of state which reflects (determines) properties of the matter created in heavy ion collisions.

Event by event analysis will help identify phase transition in high energy nuclear collisions, whether it is first order or a soft cross over. Density fluctuations may be expected to show up in phase space. The high multiplicity at RHIC and LHC energy makes erraticity analysis, at least for central and mid-central events, a very good way to characterize anomalous event by event phase space fluctuations.

STAR has measured a wide range of hadronic probes in both central and minimum bias Au+Au collisions at $\sqrt{s_{NN}} = 130$ GeV. It's particular focus on a broad spectrum of physics measurements will expand our understanding of heavy ion collisions on multiple fronts in the very near future. Four complementary detectors maximizes the RHIC discovery potential. We are still at the beginning of discovery of the high energy phases of matter!

Appendix A

Kinematic Variables

For two body colliding system, the beam direction is usually defined as z-axis. Many measurement are treated separately in the z-direction (longitudinal direction) and transverse directions.

The transverse direction momentum, p_t, is most often used,

$$p_t = \sqrt{p_x^2 + p_y^2} \tag{A.1}$$

p_t is boost invariant along z since its components p_x and p_y are unchanged by z-direction boost. For identified particles the transverse mass is defined as,

$$m_t = \sqrt{p_t^2 + m^2}, \tag{A.2}$$

where m is the particle mass and the transverse kinetic energy of the particle is $m_t - m$.

The most commonly used longitudinal variable is rapidity,

$$y = \frac{1}{2}\ln\Big(\frac{E + p_z}{E - p_z}\Big), \tag{A.3}$$

where E and p_z are the energy and longitudinal momentum component of the particle. Rapidity is additive under Lorentz transformation along z, which guarantees the shape of the corresponding distribution independent of the Lorentz frame. For 65 GeV incident energy of the Au beams at RHIC, the initial rapidity of each beam

is ± 4.94. When the beams are symmetric, the rapidity of the centre-of-mass system, mid-rapidity, is $y = 0$. If particle mass is much smaller than its momentum, it is convenient to use pseudorapidity, η, which is defined as

$$y = \frac{1}{2}\ln\left(\frac{E + p_z}{E - p_z}\right) \approx \frac{1}{2}\ln\left(\frac{|\vec{p}| + p_z}{|\vec{p} - p_z}\right) = \ln\left(\sqrt{\frac{1 + \cos\theta}{1 - \cos\theta}}\right) = -\ln(\tan\theta/2) \equiv \eta \quad \text{(A.4)}$$

For massless particles $\eta = y$ which only depends on it's emission angle relative to the beam axis.

Appendix B

Distance of Closest Approach Between Two Helices

The closest distance D between two helices $H1$ and $H2$ can be solved with the following literature approach,

$$\frac{d^2 D(\phi_1, \phi_2)}{d\phi_1 d\phi_2} = 0, \tag{B.1}$$

where D is the distance between the two helices at ϕ_1 and ϕ_2. The helix track model in section 4.1.1 on page 34 can also be parameterized with ϕ as a parameter of the equations:

$$\begin{aligned} x &= x_c + R\cos(\Phi_0 + h\phi) \\ y &= y_c + R\sin(\Phi_0 + h\phi) \\ z &= z_c + R\tan(\lambda)\phi \end{aligned} \tag{B.2}$$

We first project the two helix onto XY plane and find their DCA points on it which is simply the crossing points of the two circles. Let the solutions be ϕ_{p1}, ϕ_{p2} for track1 and ϕ_{n1}, ϕ_{n2} for track2. Then we look for the DCA points in 3-dimentions for each set of solutions. Take the first crossing point (ϕ_{p1}, ϕ_{n1}) for example. In general, the DCA points in 3D space is close to its 2D solution. Expand helix equation around the first 2D crossing point,

$$x_p = x_{c_p} + R_p\cos(\Phi_{0_p} + h_p\phi_{p1}) - R_p h_p \sin(\Phi_{0_p} + h_p\phi_{p1})\delta\phi_p$$

$$
\begin{aligned}
y_p &= y_{c_p} + R_p \sin(\Phi_{0_p} + h_p\phi_{p1}) + R_p h_p \cos(\Phi_{0_p} + h_p\phi_{p1})\delta\phi_p \\
z_p &= z_{c_p} + R_p \tan(\lambda_p)\phi_{p1} + R_p \tan(\lambda_p)\delta\phi_p \\
x_n &= x_{c_n} + R_n \cos(\Phi_{0_n} + h_n\phi_{n1}) - R_n h_n \sin(\Phi_{0_n} + h_n\phi_{n1})\delta\phi_n \\
y_n &= y_{c_n} + R_n \sin(\Phi_{0_n} + h_n\phi_{n1}) + R_n h_n \cos(\Phi_{0_n} + h_n\phi_{n1})\delta\phi_n \\
z_n &= z_{c_n} + R_n \tan(\lambda_n)\phi_{n1} + R_n \tan(\lambda_n)\delta\phi_n
\end{aligned}
$$

The distance between the two helices is,

$$D^2(x_p, y_p, z_p, x_n, y_n, z_n) = (x_p - x_n)^2 + (y_p - y_n)^2 + (z_p - z_n)^2.$$

The DCA point position is the solution of the set of linear equations,

$$\frac{\partial D^2}{\partial(\delta\phi_p)} = 0 \quad , \quad \frac{\partial D^2}{\partial(\delta\phi_n)} = 0.$$

After a solution is found, the candidate vertex can be chosen as the mid-point of the two DCA points on the two tracks.

Appendix C

On the Elimination of Statistical Fluctuation in Sample Factorial Moments and Event Factorial Moments

If the statistical fluctuations are Poissonian, the multiplicity distribution Q_n in the ith bin is

$$Q_n = \int_0^\infty \frac{p^n}{n!} e^{-p} D(p) dp, \tag{C.1}$$

where $D(p)$ is the dynamical distribution in the same bin. From the definition of factorial moment Eqn.6.1, neglecting the denominator, which is only for normalization, we get:

$$F_q = \frac{1}{N} \sum_N n(n-1)\cdots(n-q+1), \tag{C.2}$$

N is the number of event in a sample which is generally big and the sum is over all the event in the sample. The crucial point is that, when N is big enough, the bin-multiplicity n can take value from zero to very large (constrained only by energy conservation). Therefore,

$$\begin{aligned} F_q &= \sum_{n=0}^{\infty} n(n-1)\cdots(n-q+1) Q_n \\ &= \sum_{n=0}^{\infty} \int_0^\infty n(n-1)\cdots(n-q+1) \frac{p^n}{n!} e^{-p} D(p) dp \end{aligned}$$

$$
\begin{aligned}
&= \int_0^\infty \sum_{n=0}^{\infty} \frac{p^n}{(n-q)!} e^{-p} D(p) dp \\
&= \int_0^\infty \left(\sum_{n=0}^{\infty} \frac{p^{(n-q)}}{(n-q)!} e^{-p} \right) p^q D(p) dp \\
&= \int_0^\infty p^q D(p) dp = C_q
\end{aligned} \tag{C.3}
$$

The normalization of Poisson distribution

$$
\sum_{n=0}^{\infty} \frac{p^n}{n!} e^{-p} = 1, \tag{C.4}
$$

is used in the above derivation. The statistical fluctuations have been eliminated successfully by averaging over the event sample.

Now we come to event-factorial-moments. There are two important points that are different from sample-factorial-moments:

1. The number M of bins, unlike the number of events N, cannot be very large.
2. The total multiplicity in a single event is always fixed and this will result in a maximum bin-multiplicity n_{max}.

Therefore, for event-factorial-moment,

$$
\begin{aligned}
F_q^{(e)} &= \sum_{n=0}^{n_{\max}} n(n-1)\cdots(n-q+1) Q_n^{(e)} \\
&= \sum_{n=0}^{n_{\max}} \int_0^\infty n(n-1)\cdots(n-q+1) \frac{p^n}{n!} e^{-p} D(p) dp \\
&= \int_0^\infty \left(\sum_{n=0}^{n_{\max}} \frac{p^{(n-q)}}{(n-q)!} e^{-p} \right) p^q D(p) dp
\end{aligned} \tag{C.5}
$$

Because of the cutoff at n_{max}, normalization condition (C.4) cannot be used now, and therefore

$$
F_q^{(e)} \neq \int_0^\infty p^q D(p) dp. \tag{C.6}
$$

Bibliography

[1] E.G. Ferreiro A. Capella and C.A. Salgado. *Phys. Lett.*, B459:27, 1999.

[2] J. Aichelin and K. Werner. *Phys. Lett.*, B300:158, 1993.

[3] A.Krasnitz and R.Venugopalan. *Phys. Rev. Lett.*, 84:4309, 2000.

[4] A.M.Poskanzer and S.A.Voloshin. Methods for analyzing anisotropic flow in relativistic nuclear collisions. *Phys. Rev.*, C58:1671, 1998.

[5] A. Białas and R. Peschanski. *Nucl. Phys.*, B273:703, 1986.

[6] A. Białas and R. Peschanski. *Nucl. Phys.*, B308:857, 1988.

[7] M. Gyulassy B. Zhang and C.M. Ko. *Phys. Lett.*, B455:45, 1999.

[8] D. Bailin and A. Love. *Phys. Rep.*, 107:325, 1984.

[9] J.D. Bjorken. *Phys. Rev.*, D27:140, 1983.

[10] Brookhaven National Laboratory. *RHIC Design Manual*, technical report edition, 1994. URL: http://www.agsrhichome.bnl.gov/NT-share/rhicdm/.

[11] Z. Cao and R. Hwa. *Phys. Rev. Lett.*, 75:1268, 1995.

[12] Z. Cao and R. Hwa. *Phys. Rev.*, D54:6674, 1996.

[13] Z. Cao and R. Hwa. *Phys. Rev.*, E56:326, 1997.

[14] Z. Cao and R.C. Hwa. *Phys. Rev.*, D59:114023, 1999.

[15] Plastic Ball Collaboration. *Phys. Rev.*, C42:640, 1990.

[16] L.P. Csernai. *Introduction to Relativistic Heavy Ion Collisions.* JOHN WILEY & SONS, 1994.

[17] Manuel Calderon de la Barca Sanchez. *Charged Hadron Spectra in Au+Au Collisions at 130GeV.* PhD thesis, Yale University, 2001.

[18] S. Bernard D.H. Rischke and J.A. Maruhn. *Nucl. Phys.*, A595:346, 1995.

[19] V.V. Dixit. *Mod. Phys. Lett.*, A5:227, 1990.

[20] I.M. Dremin E.A. De Wolf and W. Kittel. *Phys. Rep.*, 270:1, 1996.

[21] K.H. Ackermann er al. The star time projection chamber. *Nucl. Phys.*, A661:681c–685c, 1999.

[22] H. Wieman et al. *IEEE Trans. Nuc. Sci.*, 44:671, 1997.

[23] K.H. Ackermann et al. *Phys. Rev. Lett.*, 86:402, 2001.

[24] M.Aguilar-Benitez et al. *em Nucl. Instrum. Methods*, 205:79, 1983.

[25] Particle Data Group (D.E. Groom et al.). *Eur. Phys. J.*, C45:1, 2000.

[26] T.H. Burnett et al. *Phys. Rev. Lett.*, 50:2062, 1983.

[27] V.K. Magas et al. *Heavy Ion Phys.*, 9:193, 1999.

[28] J. Barrette et al. (E877 Collaboration). *Phys. Rev. Lett.*, 73:2532, 1994.

[29] J. Barrette et al. (E877 Collaboration). *Phys. Rev.*, C63:014902, 2001.

[30] P. Chung et al. (E895 Collaboration). *Phys. Rev. Lett.*, 85:940, 2000.

[31] M. Justice et al. (EOS Collaboration). *Phys. Lett.*, B440:12, 1998.

[32] S. Wang et al. (EOS Collaboration). *Phys. Rev. Lett.*, 76:3911, 1996.

[33] P. Crochet et al. (FOPI Collaboration). *Phys. Lett.*, B486:6, 2000.

[34] Y. Shin et al. (KaoS Collaboration). *Phys. Rev. Lett.*, 81:1576, 1998.

[35] N.M. Agababyan et al. (NA22). *Phys. Lett.*, B382:305, 1996.

[36] N.M. Agababyan et al. (NA22). *Phys. Lett.*, B431:451, 1998.

[37] N.M.Agababyan et al. (NA22). *Phys. Lett.*, B382:305, 1996.

[38] N.M.Agababyan et al. (NA22). *Phys. Lett.*, B431:451, 1998.

[39] H. Appelsh*ä*user et al. (NA49 Collaboration). *Phys. Rev. Lett.*, 80:4136, 1998.

[40] H. Appelsh*ä*user et al (NA49 Collaboration). *Phys. Rev. Lett.*, 80:4136, 1998.

[41] C. Adler et al. [STAR Collaboration]. *Phys. Rev. Lett.*, 87:182301, 2001.

[42] M.M. Aggarwal et al. (WA98 Collaboration). *Phys. Lett.*, B469, 1999.

[43] I.V.Ajineko et al.(NA22). *Phys. Lett.*, B222:306, 1989.

[44] I.V.Ajineko et al.(NA22). *Phys. Lett.*, B235:373, 1990.

[45] F.Cooper and G.Frye. *Phys. Rev.*, D10:186, 1974.

[46] F.P.M.Botterweck. PhD thesis, University of Nijmegen, 1992.

[47] Wu Yuanfang Fu Jinghua and Liu Lianshou. *High energy physics and nuclear physics*, 2000. hep-ph/9901408.

[48] T.K. Gaisser and F. Halzen. *Phys. Rev. Lett.*, 54:1754, 1985.

[49] M. Gell-Mann. *Phys. Lett.*, 8:214, 1964.

[50] M. Gyulassy and M. Pl*ü*mer. *Phys. Lett.*, B243:432, 1990.

[51] M. Gyulassy and X.N. Wang. *Nucl. Phys.*, B420:583, 1994.

[52] A. Levy H. Heiselberg. *Phys. Rev.*, C59:2716, 1999.

[53] H. St*ö*cker H. Sorge, M. Berenguer and W. Greiner. *Phys. Lett.*, B289:6, 1992.

[54] H. Sorge H. van Hecke and N. Xu. *Phys. Rev. Lett.*, 81:5764, 1998.

[55] R. Hagedorn. *Riv. Nuovo Cimento*, 6:1, 1983.

[56] P.F. Kolb P. Huovinen U. Heinz H. Heiselberg. *Phys. Lett.*, B500:232, 2001.

[57] T. Hirano. *Phys. Rev.*, C65:011901, 2002. nucl-th/0108004.

[58] H.Stocker and W.Greiner. *Phys. Rept.*, 137:277, 1986.

[59] R. C. Hwa. *Acta Physica Polonico*, B27:1789, 1996.

[60] F.Retiere J.H. Thomas. *The STAR Time Projection Chamber: A Unique Tool for Studing High Multiplicity Events at RHIC*, 2002. http://www.star.bnl.gov/ jhthomas/NimWeb.

[61] Yuanfang Wu Jinghua Fu and Lianshou Liu. *Phys. Rev.*, C60:067603, 1999.

[62] Yuanfang Wu Jinghua Fu and Lianshou Liu. *Phys. Lett.*, B472:161–167, 2000.

[63] S. S. Rasanen K. J. Eskola, P. V. Ruuskanen and K. Tuominen. *Nucl. Phys.*, A696:715, 2001. hep-ph/0104010.

[64] F. Karsch. *Nucl. Phys. Proc. Suppl.*, 83:14–23, 2000.

[65] G.I. Kopylov. *Phys. Lett.*, B50:472, 1974.

[66] M. Lamont. *in Proceedings of Strange Quarks in Matter*, 2001.

[67] L.D. Landau. *Izv. Akad. Nauk SSSR*, 17:51, 1953.

[68] P.T. Landsberg. *Thermodynamics and Statistical Mechanics.* Oxford Univ. Press, Oxford, UK, 1978.

[69] Jinghua Fu Lianshou Liu and Yuanfang Wu. *Phys. Lett.*, B444:563–568, 1998.

[70] G.L.Gogiberidze L.K.Gelovani and E.K.Sarkisyan. hep-ph/9809502, 1998.

[71] Hui Long. *Mid-rapidity Λ and $\bar{\Lambda}$ Production in Au+Au Collisions at the Relativistic Heavy Ion Collider.* PhD thesis, University of California, Los Angeles, 2002.

[72] NA22 Coll. M.Adamus et al. *Z. Phys.*, C32:475, 1986.

[73] L. McLerran and R. Venugopalan. *Phys. Rev.*, D49:2233, 1994.

[74] M.Gyulassy and L.McLerran. *Phys. Rev.*, C56:2219, 1997.

[75] D. Molnar and M. Gyulassy. *Phys. Rev.*, C62:054907, 2000.

[76] N.F. Mott. *Proc. Phys. Soc. (London)*, A42:416, 1949.

[77] P.M. Dinh N. Borghini and J.Y. Ollitrault. *Phys. Lett.*, B477:51, 2000.

[78] P.M. Dinh N. Borghini and J.Y. Ollitrault. *Phys. Rev.*, C62:34902, 2000.

[79] P.M. Dinh N. Borghini and J.Y. Ollitrault. *Phys. Rev.*, C63:054906, 2001.

[80] Johannes P. Wessels Norbert Herrmann and Thomas Wienold. *Annu. Rev. Nucl. Part. Sci.*, 49:581–632, 1999.

[81] J.-Y. Ollitrault. *Phys. Rev.*, D46:229, 1992.

[82] J.-Y. Ollitrault. *Nucl. Phys.*, A638:195c, 1998.

[83] J.Sollfrank P.F. Kolb and U. Heinz. *Phys. Rev.*, C62:054909, 2000.

[84] K. Adcox et al. PHENIX Collaboration. *Phys. Rev. Lett.*, 88:022301, 2002.

[85] J. Podolanski and R. Armenteros. *Phil. Mag.*, 45:13, 1954.

[86] A.M. Poskanzer and S.A. Voloshin. *Phys. Rev.*, C58:1671, 1998.

[87] J. Rafelski. *Phys. Rep.*, 88:331, 1982.

[88] W. Reisdorf and H.G.Ritter. *Annu. Rev. Nucl. Part. Sci.*, 47:663–709, 1997.

[89] W. Reisdorf and H.G. Ritter. *Annu. Rev. Nucl. Part. Sci.*, 47:663, 1997.

[90] Z. Wang S. Wang and C. Wu. *Phys. Lett.*, B410:323, 1997.

[91] H. Satz. *Nucl. Phys.*, A418:447c, 1984.

[92] H. Satz. *Rep. Prog. Phys.*, 63:1511, 2000.

[93] B.R. Schlei and D. Strottman. *Phys. Rev.*, C59:9, 1999. nucl-th/9806034.

[94] Wang Shaushun and Wang Zhaomin. *Phys. Rev. D*, 57:3036, 1998.

[95] S.Margetis. *Kaons and Lambdas in the STAR TPC*, 1998. STAR-Note No.367.

[96] H. Sorge. *Phys. Rev. Lett.*, 78:2309, 1997.

[97] H. Sorge. *Phys. Rev. Lett.*, 82:2048, 1999.

[98] C. Adler et al. STAR Collaboration. 2002. nucl-ex/0206001, submitted to Phys. Rev. C.

[99] J. Dunlop et al. STAR Collaboration. *Nucl. Phys.*, A698:515c, 2002.

[100] P. Houvinen P.F. Kolb U. Heinz P.V. Ruuskanen S.A. Voloshin. *Phys. Lett.*, B503:58, 2001.

[101] S. Voloshin and Y. Zhang. *Z. Phys.*, C70:665, 1996.

[102] X. Wang and M. Gyulassy. *Phys. Rev.*, D44:3501, 1991.

[103] X. Wang and M. Gyulassy. *Phys. Rev. Lett.*, 86:3496, 2001.

[104] X.N. Wang. *Phys. Rev.*, C63:054902, 2001.

[105] Zhang Kunshi Wu Yuanfang and Liu Lianshou. *Chinese Science Bulletin*, 36:1077, 1991.

[106] Wu Yuanfang and Liu Lianshou. *Phys. Lett.*, B269:28, 1991.

[107] Wu Yuanfang and Liu Lianshou. *Phys. Rev. Lett.*, 70:3197, 1993.

Publications and Presentations

1. C. Adler et al. (STAR Collaboration)
   Azimuthal Anisotropy of K^0_S and $\Lambda + \bar{\Lambda}$ Production at Midrapidity from Au+Au Collisions at $\sqrt{s_{NN}} = 130$ GeV
   Submitted to Phys. Rev. Lett.
   main author: Jinghua Fu, Paul Sorensen

2. Jinghua Fu, Yuanfang Wu and Lianshou Liu
   The Influence of Statistical Fluctuations on Erraticity Behavior of Multiparticle System
   Phys. Lett. **B472**:161-167, 2000

3. Jinghua Fu, Tachung Meng, R. Rittel and K. Tabelow
   Criticality in Quark Gluon Systems Far Beyond Thermal and Chemical Equilibrium
   Phys. Rev. Lett. **86**:1961-1964, 2001

4. Jinghua Fu, Yuanfang Wu and Lianshou Liu
   Order Parameter of a Single Event
   Phys. Rev. **C60**:067603, 1999

5. Jinghua Fu, Lianshou Liu
   Identification of Color Reconnection Using Factorial Correlator
   Chin. Phys. Lett. **17**:338-339, 2000

6. Lianshou Liu, Jinghua Fu and Yuanfang Wu
   On the Dominance of Statistical Fluctuation in the Factorial Moment Study of Chaos in Low Multiplicity Events of High-Energy Collisions
   Sci. China **43**:1215-1223, 2000

7. Lianshou Liu, Jinghua Fu and Yuanfang Wu
   Scaling Exponent and Fluctuation Strength in High-Energy Collisions
   Phys. Lett. **B444**:563-568, 1998

8. Yuting Bai, Jinghua Fu and Yuanfang Wu
Event by Event Fluctuations of Transverse Momentum in Elementary Collisions at 250 GeV/c
Talk given at 31st International Symposium on Multiparticle Dynamics (ISMD 2001), Datong, China, Sep.1-7, 2001

9. Lianshou Liu, Gang Chen and Jinghua Fu
A Monte Carlo Study of the Dynamical Fluctuation Property of the Hadronic System Inside Jets
Phys. Rev. **D63**:054002, 2001

10. Jinghua Fu (main author), NA22 Collab.
Erraticity Analysis of Multiparticle Production in π^+p and K^+p Collisions at 250GeV/c
to be published

Acknowledgements

The two parts of this thesis, elliptic flow and fluctuation analysis, marks the two very important stages of my Ph.D studying. I would like to thank my supervisor Wu Yuanfang and Liu Lianshou at Institute of Particle Physics (IOPP) for introducing me into high energy physics in 1997 and constant supporting me over the following five years. That's really a unforgettable time for me. Without their encouragement and help I couldn't have made this step. I would like to thank Liu Feng, Wang Enke and everyone at IOPP for helping me go through the very hard time when I start.

The main part of this thesis, K^0_S and $\Lambda + \bar{\Lambda}$ elliptic flow analysis, is made at Lawrence Berkeley National Laboratory (LBNL). I would like to thank H.G. Ritter for offering me this great opportunity to work with the Relativistic Nuclear Collision (RNC) group and support me over the past two years. I want to thank Nu Xu for picking up this nice topic and being so kind and patient in guiding me going through it. I would like to thank A.M. Poskanzer, R. Snellings and S.A. Voloshin for valuable assistance in flow analysis. I want to thank everyone of the RNC group for the help and happiness they bring me!

I started my STAR data analysis at UCLA. I would like to thank H. Huang, H. Long and E. Yamamoto for helping me understand STAR software and strangeness reconstruction. The whole K^0_S and Λ elliptic flow analysis is done together with P. Sorensen. It is really nice time of corporation. I thank everyone of the UCLA Heavy Ion and Intermediate Energy Group, especially my best friend J. Kiryluk.

I had very nice time in High Energy Experiment group at Nijmegen University. I would like to thank W. Kittle for supporting me while I am there and guiding me with NA22 and L3 data analysis. I thank W. Metzger for introducing and guiding me with color reconnection analysis at LEPII.

I will never forget my two weeks in Berlin Freie University working with T.C Meng and students there on Self-Organize Criticality (SOC).

I would like to thank the STAR Collaboration for everything I got here!